POLITECNICO DI TORINO

CORSO DI LAUREA MAGISTRALE IN INGEGNERIA CIVILE

SCALE EFFECTS ON FRC COMPOSITES:

BRITTLE, PERFECTLY-PLASTIC, SOFTENING POST-PEAK REGIMES

Tesi di Laurea Magistrale

Relatore

Chiar.mo Prof. Ing. Alberto Carpinteri

Correlatori

Ill.mo Dr. Ing. Federico Accornero   **Candidata**

Ill.mo Ing. Alessio Rubino   Angela Muscolino

23 Luglio 2020

Ai miei genitori, fonti delle mie essenziali conoscenze

Acknowledgments

I would like to thank my supervisor, Chiar.mo Prof. Ing. Alberto Carpinteri. First of all he made me fall in love with Fracture Mechanics, then he guided me in this fascinating research on FRC.

My sincere gratitude also to my co-supervisors, Dr. Ing. Federico Accornero and Ing. Alessio Rubino. They gave me invaluable suggestions, taking care of my every question.

Ringraziamenti personali

"La cosa più difficile è la decisione iniziale di agire, il resto è solo tenacia.
Le paure sono tigri di carta" (Amelia Earhart)

Quello al Politecnico di Torino è stato senza alcun dubbio il più ambizioso percorso che io abbia mai intrapreso, sia dal punto di vista accademico che personale. Ho affrontato molte "tigri di carta" nel corso di questi anni, mai mi sono sentita sola.

Voglio ringraziare i miei genitori, per tutto, ma soprattutto grazie per l'esempio di tenacia, per i vostri sacrifici e per ogni parola di incoraggiamento.

Grazie ai miei fratelli, Rossella e Filippo, insieme ai miei cognati, Concetto e Loredana, per l' aiuto concreto e sempre confortante. Grazie anche per essere stati vicini a mamma e papà tutte le volte in cui io non ho potuto.

Un ringraziamento del tutto speciale alla piccola Arianna, perché inconsapevolmente è stata il mio punto forte, il mio pensiero positivo. Nei suoi abbracci ho sempre ritrovato la mia forza.

Grazie ai miei zii Maria e Nino, con Giò e Salvo, per l'aiuto, l'affetto e l'incoraggiamento mai mancati.

Grazie agli amici di tutta la vita, Emanuela, Enzo, Filippo, Rosario e Stefania. Il vostro affetto e il tempo trascorso insieme sono per me sempre più preziosi.

Grazie a chi ha reso un appartamento la mia casa, riempiendolo di affetto e serenità: Alessia, Maria e Paola. Considero la vostra amicizia un dono di questo percorso.

Grazie ad Alessio e a Renato, per la pazienza avuta con me durante questi mesi, per il vostro aiuto concreto e per un'amicizia che è stata una bella scoperta.

Grazie, infine, alle tante persone che hanno fatto parte di questo percorso e che hanno condiviso un po' del loro tempo con me.

ABSTRACT

In the framework of Fracture Mechanics, the present work aims to analyse the mechanical behaviour of Fiber-Reinforced Concrete (FRC) structural elements subjected to monotonically increasing flexural loading.

Following this purpose, the Bridged Crack Model is proposed as a Fracture Mechanics based approach able to describe the crack propagation process occurring in the cross-section of FRC structural elements. After a brief introduction, the basic features of this model are extensively described in Chapter 2: the concrete matrix is assumed as elastic-perfectly brittle, whereas the bridging mechanism of the secondary phase is modelled with suitable constitutive laws, describing the pull-out mechanisms of the reinforcing fibers. These mechanisms are experimentally determined on the basis of pull-out tests results, reported in the scientific literature, depending on the geometry of the reinforcing steel fibers, as discussed in Chapter 3. On the basis of equilibrium and compatibility conditions, the response of the cracked cross-section is described in terms of applied moment vs localized rotation diagrams.

Extensive experimental studies reported in the scientific literature suggest to describe the flexural response of FRC beams, by subdividing it into three different stages. Considering a notched FRC specimen subjected to bending, the related applied load vs deflection diagram starts with a linear elastic ascending branch (stage I), up to the initiation of the fracturing process. From this point forward, the post-cracking phase (stage II) of the element takes place, during which the main crack gradually propagates while the reinforcing fibers exert their bridging action. Depending on several conditions, including the fiber volume content, different post-cracking behaviour of the composite can be obtained, such as the perfectly-plastic one. The flexural response is finally described by a descending softening branch (stage III) of the load vs deflection curve, where the fiber pull-out from the brittle matrix (fiber slippage) is the dominant phenomenon.

By applying the Buckingham's π theorem, the dimensional analysis reveals two dimensionless parameters, N_{P} and N_{W}, as crucial in the identification of the mechanical response of the composite in the post-cracking regimes. The first one, $N_{\mathrm{P}} = V_{\mathrm{f}} \dfrac{\tau_u (2\lambda)}{K_{\mathrm{IC}}} \sqrt{h}$, depends on the fiber volume fraction, V_{f}, the matrix fracture toughness, K_{IC}, the mechanical and geometrical properties of the fiber, τ_{u} and λ, and the beam characteristic

I

size, h. The second one, $N_W = \dfrac{E w_C}{K_{IC}\sqrt{h}}$, depends on the matrix fracture toughness, K_{IC}, the matrix Young's modulus, E, the beam characteristic size, h, and the average embedded length of the fiber into the matrix, w_C. Numerical simulations conducted on the basis of the numerical algorithm reported in Chapter 4, point out the effect of the two dimensionless parameters on the global response of the composite. It is found that the reinforcing brittleness number, N_P, governs the stage II of the response, whereas a fixed value of N_W provides the collapse of the curves onto a unique final branch, related to the stage III of the structural behaviour. In conclusion, by varying N_P and N_W, brittle, perfectly-plastic, and softening regimes can be identified.

In the second part of this work, the model is validated on the basis of experimental campaigns, carried out by other Authors on prismatic specimens of FRC subjected to flexural loading. A comparison between numerical results and experimental data proves the effectiveness of the Bridged Crack Model also in the identification of the constitutive law of the composite. More precisely, the experimental curves can be easily reproduced by varying four parameters. The matrix Young's modulus, E, and the matrix fracture toughness, K_{IC}, are required to identify the elastic stage. On the other hand, the maximum bridging force, related to N_P, and the critical embedded length, related to N_W, are essential to fully describe the post-cracking regime of the response. For each experimental campaign, the identifying parameters can be determined, which makes the model able to evaluate the minimum reinforcement condition, required to achieve a stable post-cracking response.

Finally, the last Chapter of this work is devoted to the simulation of experimental campaigns which involve FRC specimens of different sizes. Three experimental studies are analysed and reproduced, confirming the model's capability to understand in a comprehensive manner the size effects occurring in the structural behaviour of FRC.

Contents

Chapter 1
INTRODUCTION

Recent developments in concrete technology, revealed the advantages in the structural performance of the material, when fibers were included in the concrete mixture. In this perspective, the Fiber Reinforced Concrete (FRC) was developed in the second half of the twentieth century.

This material is generally defined as cementitious composite made of two main components: the cementitious matrix and the reinforcing fibers. The cementitious matrix may itself be considered a composite with several components (aggregate, additive, water), but it will be assumed to represent, in this context, the first main component of the FRC composite. The fiber is the secondary phase of the composite, and it is assumed discontinuous and randomly oriented and distributed within the volume of the composite. Both the fiber and the matrix work together, providing the synergism required to make an effective composite (Naaman, 2008). The constituents are characterized by enormous variability. High Strength Concrete, High Performance Concrete and many others special concretes are indeed available with modern technologies. Fiber also can be really different, both for material and geometry. They can be made of steel, polymeric materials as well as inorganic materials such as carbon, glass and natural materials (CNR, 2006). Moreover, the fiber shape can be undeformed (straight), with a round or flat section; there are also fibers with deformed profile, such as cramped along the length or with hooked end. This work is focused on composites with steel fiber (SFRC), but the concepts relating to mechanical and geometric parameters could also be extended to other materials.

The experimental research on the flexural behaviour of the FRC specimens pointed out three different stages into a typical load-deflection curve. The diagram starts with a linear ascending branch (stage I), up to the initiation of the fracturing process. From this point forward, the post-cracking phase (stage II) of the element takes place, during which the main crack gradually propagates while the reinforcing fibers exert their bridging action. Depending on several conditions, including the fiber volume content, different behaviour of the composite can be exhibited by the composite in the second stage, such as brittle, perfectly plastic, or hardening. The flexural response finally experiences a descending branch (stage III), in this phase the fiber pull-out is the dominant mechanism.

The fundamental role of the secondary phase is that of providing crack control and improving the fracture toughness of the composite, by means of a bridging action affecting the matrix macro- and microcracks. However, in order to guarantee the required mechanical properties with minimum fiber employment, it have to be take into account several parameters in the design of the so called *minimum reinforcement*: Fiber geometric an mechanical characteristics, concrete mechanical properties, fiber volume fraction, and geometrical characteristic of the structural element. Experimental tests are thus necessaries, both on the two individual main components and on the composite mixture.

The purpose of this work is to give a contribute in understanding the aforementioned stages, in the framework of Fracture Mechanics. Following this purpose, the Bridged Crack Model is proposed to reproduce analytically the flexural response, providing the identification of the constituent materials. The application of Buckingham's π Theorem revealed two dimensionless parameters, which synthetically describe the post-cracking response of the composite.

Moreover, the flexural behaviour of different specimens made of the same materials vary according to specimen size. This phenomenon, known as *size effect*, was already studied in ordinary reinforced concrete by Bosco, Carpinteri and Debernardi (1990). In this work these analyses are extended to the SFRC response.

In conclusion, it will be clear how, by means of Bridged Crack model and Dimensional Analysis, it is possible to interpret the tests and predict the mechanical behaviour of the structural element, by varying the design parameters, taking into account also the effects of the size variation.

Chapter 2

THE BRIDGED CRACK MODEL

2. 1   Introduction

The fibrous composites show a common feature: the bridging action exerted by the fibers. This behaviour is the focus of the mechanical models, proposed in the literature, for the analysis of these materials.

In the framework of Fracture Mechanics, two peculiar models can be used to analyse the composite failure process: the *Bridged Crack model* and the *Cohesive Crack model*. They have been represented in a dimensionless formulation by Carpinteri et al. (1996), and an experimental campaign demonstrated that, with a correct definition of the parameters characterizing the two options, both lead to the same structural behaviour (Carpinteri et al., 1996). The key-differences among these two models lies in the material basic assumptions, regarding the crack-tip stress field and the crack propagation condition.

The *Cohesive Crack model*, in accordance with the model proposed by Barenblatt (1962) for the analysis of brittle *heterogeneous* materials and then by Dugdale (1962) for the analysis of ductile materials, has been proposed by Hillerborg et al. (1976) with the name of Fictitious Crack model. The basic hypothesis of the Cohesive model is to replace the fracture process zone (FPZ) with a fictitious crack in which a distribution of reclosing tractions stresses applies. The cohesive tractions have a maximum value where the crack opening displacement is zero, and vanish when the crack opening displacement reaches its critical value. The stress field at the fictitious crack tip is hypothesized finite, and the crack propagation condition is assumed when the maximum stress reaches the composite tensile strength.

On the other hand, the *Bridged Crack model* is a fracture mechanic model which assumes the composite material as a *biphasic* material, where the matrix and the reinforcing fibres constitute the first and the secondary phase, respectively. Under this assumption, the bridging mechanisms of the reinforcing fibers are modelled with a continuous (in continuous models) or discontinuous (in discontinuous model) distribution of reclosing forces, applied onto the crack faces. The model assumes a singular stress field

7

in the crack-tip vicinity, and the crack propagates when the crack tip stress intensity factor, K_I, reaches its critic value, i.e., the matrix fracture toughness, K_{IC}.

Different versions of continuous model have been formulated for the analysis of uniformly distributed reinforcements (Marshall et al., 1985; Jenq and Shah, 1985; Foote et al., 1986; Cox and Marshall, 1994; Carpinteri et al., 1997).

The discontinuous model was originally proposed by Carpinteri (1984) to investigate the fracturing process in reinforced concrete beams under monotonic bending, and it was subsequently extended also to the case of cyclic loading (A. Carpinteri and An. Carpinteri, 1984). This discontinuous model was able to describe the behaviour of element with localized reinforcement, such as bars, wires, and riveted or bonded stiffeners. However, when the number of localized reinforcement becomes sufficiently high, the global results of discontinuous and continuous models are convergent (A. Carpinteri et al., 1997), providing a useful tool for the analysis of fibrous materials. More recently, significant advances have been made in the implementation of the discontinuous numerical model, both for motonically increasing and cyclical loading (Carpinteri et al., 2019; Accornero et al., 2020).

In this Chapter, the discontinuous model for FRC beams under monotonic bending is presented, which is the base of the numerical algorithm described in fourth Chapter.

2. 2   Theoretical model

2. 2. 1   Basic assumptions

The discontinuous model refers to Figure 2.1, where a scheme of the cracked cross section of a FRC beam in bending is represented. The geometry of the beam cross section is rectangular, characterized by the thickness, b, the depth, h, and the initial edge crack, a_0. The number of fibers for each section is n, uniformly distributed in the ligament, with generic position c_i. The $m < n$ fibers crossing the crack are considered as active, which bridging action is represented by the m reclosing forces, F_i. The total number of fibers crossing the mid-span cross section is assumed as a deterministic quantity, calculated as:

$$n = V_f \frac{bh}{A_f},$$

(2.1)

where A_f is the cross-sectional area of the single fiber, and V_f is the fiber volume ratio.
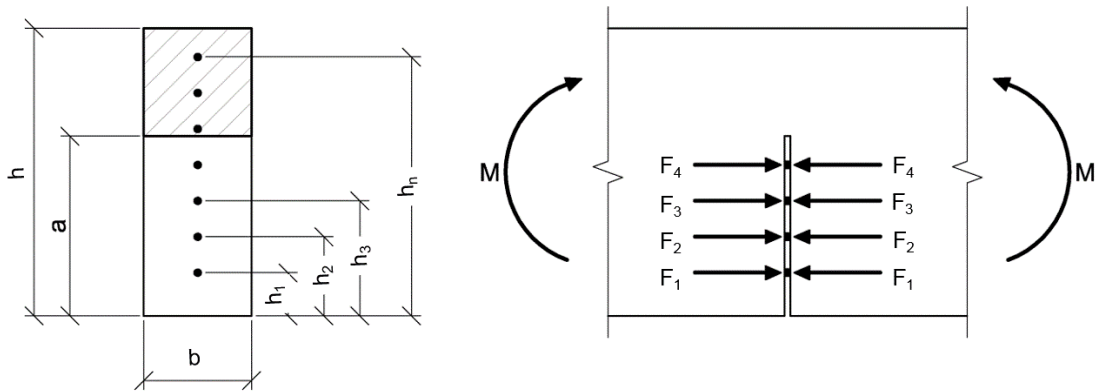

Figure 2.1 Theoretical scheme of the discontinuous model.

The depth of the initial crack and the generic position of the fiber can be normalized with respect to the beam crack depth, h, as provided in Eq. (2.2) and in Eq. (2.3), respectively. The bottom of the beam is assumed as the origin of the reference system.

$$\xi = \frac{a_0}{h}$$

(2.2)

$$\zeta_i = \frac{c_i}{h}$$

(2.3)

9

The material behaviour in theoretical model is defined through some following assumptions. The concrete matrix is assumed linear elastic-perfectly brittle, both in traction and in compression, characterized by the Young's modulus, E, and its fracture toughness, K_{IC}. The fibers are considered as uniformly distributed in the matrix, their orientation is assumed horizontal, and the embedded length is considered the same for all the fibers. In Figure 2.2 it is showed the difference between the fiber distribution assumed in the model, and the actual one. Further developments of the model could randomize the position and orientation of the fiber, considering these quantities as stochastic variables.
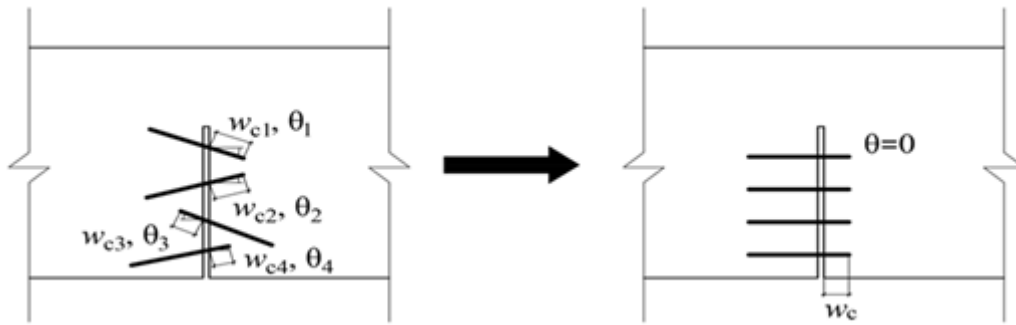
Figure 2.2 From real to model fiber distribution.

By the position and orientation of the fibers depends their bridging action. Considering the model distribution, instead, the bridging action is related only to the crack opening displacement along the crack faces at the fiber level, w_i; there is no more reclosing force when the crack opening displacement is equal to the embedded length. The relationship among the reclosing force and w_i, namely *slippage constitutive law* or *bridging law*, can be obtained from experimental tests or micromechanical models, which are illustrated in third Chapter.

2. 2. 2   Stress-intensity factor

The model assumes the crack propagation condition in according to LEFM, Eq. (2.4), considering only the Mode I opening:

$$K_I = K_{IC}. \tag{2.4}$$

The value of stress intensity factor at the crack tip is obtained, by means of the superposition principle, taking into account the two opposite contributes, due to bending moment and reclosing forces:

$$K_{\mathrm{I}} = K_{\mathrm{IM}} - \sum_{i=1}^{m} K_{\mathrm{Ii}}. \tag{2.5}$$

As regard the first contribute, considering a simply cracked bended strip, represented in Figure 2.3, Tada et al. (1985) found the following expression:

$$K_{\mathrm{IM}} = \frac{M}{h^{1.5}b} Y_{\mathrm{M}}(\xi). \tag{2.6}$$

Figure 2.3. Simply cracked bended strip.

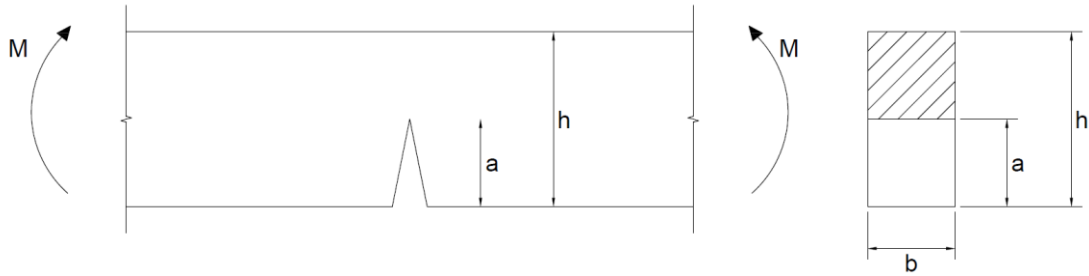Considering the same geometry, the stress intensity factor due to a concentrated force, applied on the crack face (Figure 2.4), is given by:
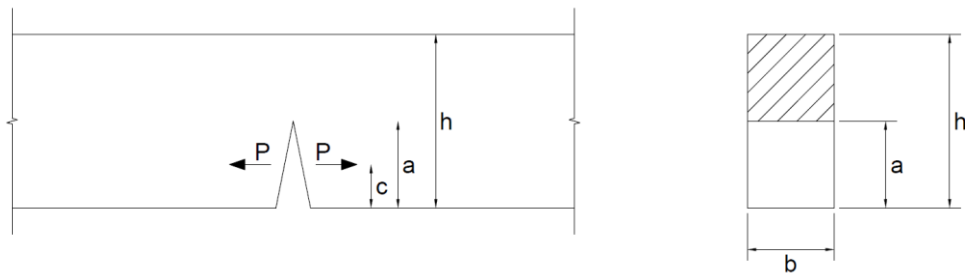
$$K_{\mathrm{IF}} = \frac{F}{h^{0.5}b} Y_{\mathrm{F}}(\xi,\zeta) \tag{2.7}$$

Figure 2.4. Simply cracked strip with concentrated forces.

In Eq. (2.6) and Eq. (2.7), two shape functions, Y_{M} and Y_{F}:

$$Y_{\mathrm{M}}(\xi) = \begin{cases} 6\left(1.99\xi^{0.5} - 2.47\xi^{1.5} + 12.97\xi^{2.5} - 23.17\xi^{3.5} + 24.8\xi^{4.5}\right) & \xi \le 0.6 \\ 3.99(1-\xi)^{-1.5} & \xi > 0.6 \end{cases}, \quad (2.8)$$

$$Y_{\mathrm{F}}(\xi,\zeta_{\mathrm{i}}) = \frac{2}{\sqrt{\pi\xi}} \frac{1}{(1-\xi)^{1.5}\sqrt{1-\left(\dfrac{\zeta_{\mathrm{i}}}{\xi}\right)^2}} G(\xi,\zeta_{\mathrm{i}}) \qquad \xi > \zeta_{\mathrm{i}}, \qquad (2.9)$$

$$G(\xi,\zeta_{\mathrm{i}}) = g_1(\xi) + g_2(\xi)\frac{\zeta_{\mathrm{i}}}{\xi} + g_3(\xi)\left(\frac{\zeta_{\mathrm{i}}}{\xi}\right)^2 + g_4(\xi)\left(\frac{\zeta_{\mathrm{i}}}{\xi}\right)^3, \qquad (2.10)$$

$$g_1(\xi) = 0.46 + 3.06\xi + 0.84(1-\xi)^5 + 0.66\xi^2(1-\xi)^2, \qquad (2.11)$$

$$g_2(\xi) = -3.52\xi^2, \qquad (2.12)$$

$$g_3(\xi) = 6.17 - 28.22\xi + 34.54\xi^2 - 14.39\xi^3 - (1-\xi)^{1.5} - 5.88(1-\xi)^5 - 2.64\xi^2(1-\xi)^2, \quad (2.13)$$

$$g_4(\xi) = -6.63 + 25.16\xi - 31.04\xi^2 + 14.41\xi^3 + 2(1-\xi)^{1.5} + 5.04(1-\xi)^5 + 1.98\xi^2(1-\xi)^2 t. \quad (2.14)$$

It is worth noting that the shape function related to the bending moment, Eq. (2.8), is a function of the normalized crack depth. On the other hand, the shape function introduced for the concentrated force, Eq. (2.9), depends also on the normalized fiber position, and it provides a singularity for $\xi = \zeta_{\mathrm{i}}$.

2. 2. 3   Compliances of a cracked beam element

The bridging forces transmitted by the active fibers are statically undetermined. Until the beginning of the fiber pull-out, they are founded by imposing compatibility conditions. Following this purpose, the compliances of a cracked beam are introduced.

The compliance matrix, in the simplest case of $m=1$, is a matrix that connect rotation, φ, and crack opening, w, to the applied bending moment M and the reinforcement reaction F:

$$\begin{Bmatrix} \varphi \\ w \end{Bmatrix} = \begin{Bmatrix} \lambda_{MM} & \lambda_{MF} \\ \lambda_{FM} & \lambda_{FF} \end{Bmatrix} \begin{Bmatrix} M \\ F \end{Bmatrix} . \tag{2.15}$$

The matrix in Eq. (2.15) is symmetric, i.e., $\lambda_{MF} = \lambda_{FM}$, for Betty's theorem. In order to obtain the value of the compliances an energetic approach, based on the Clapeyron's theorem, is applied. The energy variation of the cracked beam element can be written as:

$$-\Delta W = \frac{1}{2} M \varphi + \frac{1}{2} F w , \tag{2.16}$$

$$-\Delta W = \frac{1}{2} \lambda_{MM} M^2 + \frac{1}{2} \lambda_{FF} F^2 + \lambda_{MF} MF . \tag{2.17}$$

Then, the strain energy release rate, G_I, and the relation between G_I and K_I are introduced:

$$G_I = -\frac{dW}{dA} , \tag{2.18}$$

$$G_I = \frac{K_I^2}{E} . \tag{2.19}$$

Thus, the energy variation can be expressed by:

$$-\Delta W = \int_0^a G_I b \ dh = \int_0^a \frac{K_I^2}{E} b \ dh = \int_0^a \frac{\left(K_{IM} + K_{IF}\right)^2}{E} b \ dh = \int_0^a \frac{K_{IF}^2}{E} b \ dh + \int_0^a \frac{K_{IF}^2}{E} b \ dh + 2\int_0^a \frac{K_{IM}K_{IF}}{E} b \ dh. \tag{2.20}$$

By substituting Eq. (2.5) and Eq. (2.6), in Eq. (2.19):

$$-\Delta W = \frac{M^2}{b^2 hE} \int_0^{\xi} Y_M^2 \left(\xi\right) d\xi + \frac{F^2}{hE} \int_0^{\xi} Y_F^2 \left(\xi\right) d\xi + \frac{2MF}{bhE} \int_0^{\xi} Y_M \left(\xi\right) Y_F \left(\xi\right) d\xi . \tag{2.21}$$

By comparing Eq. (2.17) and Eq. (2.20), the compliances are obtained as follows:

$$\lambda_{MM} = \frac{2}{Eh^2 b} \int_0^{\xi} Y_M^2 \left(\xi\right) d\xi , \tag{2.22}$$

$$\lambda_{MF} = \frac{2}{Ehb} \int_0^{\xi} Y_M \left(\xi\right) Y_F \left(\xi\right) d\xi , \tag{2.23}$$

$$\lambda_{\mathrm{FF}} = \frac{2}{Eb} \int_0^{\xi} Y_{\mathrm{F}}^2(\xi)\, \mathrm{d}\xi \,. \tag{2.24}$$

For cracked element with m active fibers, the expressions of the crack openings at each fiber level and the localized rotation are defined by applying the superposition principle on the two acting contributes. The minus sign in the following equations is related to the reclosing effect of the bridging forces:

$$w_{\mathrm{i}} = w_{\mathrm{iM}} + \sum_{\mathrm{j}=1}^{m} w_{\mathrm{ij}} = \lambda_{\mathrm{iM}} M - \sum_{\mathrm{j}=1}^{m} \lambda_{\mathrm{ij}} F_{\mathrm{j}} \,, \tag{2.25}$$

$$\varphi = \varphi_{\mathrm{M}} + \sum_{\mathrm{j}=1}^{m} \varphi_{\mathrm{j}} = \lambda_{\mathrm{MM}} M - \sum_{\mathrm{j}=1}^{m} \lambda_{\mathrm{Mj}} F_{\mathrm{j}} \tag{2.26}$$

where w_{iM} and w_{ij} are the crack opening at the level of the i-th fiber due to bending moment and j-th reclosing force respectively; φ_{M} and φ_{j} are the localized rotations due to bending moment M and to concentrated forces F_{j} respectively; λ_{MM}, λ_{iM} and λ_{ij} are the local compliances, which are obtained by Carpinteri et al. (1997):

$$\lambda_{\mathrm{MM}} = \frac{2}{Eh^2 b} \int_0^{\xi} Y_{\mathrm{M}}^2(\xi)\, \mathrm{d}\xi \,, \tag{2.27}$$

$$\lambda_{\mathrm{iM}} = \frac{2}{Ehb} \int_0^{\xi} Y_{\mathrm{M}}(\xi) Y_{\mathrm{F}}(\xi, \zeta_{\mathrm{i}})\, \mathrm{d}\xi \,, \tag{2.28}$$

$$\lambda_{\mathrm{ij}} = \lambda_{\mathrm{ji}} = \frac{2}{Eb} \int_{\max(\zeta_{\mathrm{i}}, \zeta_{\mathrm{j}})}^{\xi} Y_{\mathrm{M}}(\xi) Y_{\mathrm{F}}(\xi, \zeta_{\mathrm{i}})\, \mathrm{d}\xi \,. \tag{2.29}$$

As seen, the Eqs. (2.27), (2.28), and (2.29) are analogous to Eqs. (2.22), (2.23) and (2.24). Particularly, λ_{MM} is unchanged increasing the number of fibers; λ_{iM} and λ_{ij} involve also the dimensionless position of i-th fiber. The integrals of Eq. (2.28) and Eq. (2.29) are improper because the integrand has a singularity in the interval of integration. The singularity of the first integrand is removable, while the second, for $i = j$, is not removable and the integral diverges. The problem can be overcome, as suggested by Carpinteri et al. (1997), by introducing a normalized cut-off distance, $t/h = 10^{-5}$, at the first extreme integration:

$$\lambda_{\text{ii}} = \frac{2}{Eb} \int_{\zeta_{\text{i}}+\frac{t}{h}}^{\xi} t \, Y_{\text{F}}\left(\xi,\zeta_{\text{i}}\right)^2 \mathrm{d}\xi \ . \tag{2.30}$$

Now, for each fiber level, it can possible to evaluate λ_{iM}, i.e., the crack opening displacement due to a unit bending moment, and the compliance λ_{ij}, i.e., the crack opening displacement due to a unit opening force acting at ζ_{j}.

2. 2. 4   Compatibility equation

The compatibility conditions are applied to solve the statically indeterminate problem, i. e., to evaluate the bridging forces, for a given crack depth, depending on the applied bending moment. The crack opening displacements vector is defined as:

$$\{w\} = \{w_1, ..., w_{\text{m}}\}^{\text{T}} \ , \tag{2.31}$$

where w_{i} is the crack opening displacement at the level of the *i*-th fiber, obtained by applying the superposition principle on the two opposite contributes, as seen in Eq. (2.25). The vector of the reactions of the m active fibers is defined as:

$$\{F\} = \{F_1, ..., F_{\text{m}}\}^{\text{T}} \ . \tag{2.32}$$

The vector of the local compliance due to the bending moment is defined as:

$$\{\lambda_{\text{M}}\} = \{\lambda_{1\text{M}}, ..., \lambda_{\text{mM}}\}^{\text{T}} \ . \tag{2.33}$$

By Eq. (2.25), the vector of the crack opening displacements can be written:

$$\{w\} = \{\lambda_{\text{M}}\} M - [\lambda]\{F\} \ , \tag{2.34}$$

where $[\lambda]$ is the $m \times m$ matrix of the local compliances (Eq. (2.30)) due to the bridging action, and it is symmetric for Betti's theorem.

Eq. (2.34) describe a linear system of m equations, and $2m$ unknowns, i.e., the bridging forces F_i, and the corresponding crack opening displacements, w_i. The solution of the system requires other m conditions.

In a first stage, the reinforcement shows an elastic behaviour, and it keeps the crack locally closed. Thus, in this phase, the compatibility condition is expressed by the following expression:

$$\{w\} = 0. \tag{2.35}$$

The reactions in the reinforcements can be thus calculated by substituting Eq. (2.35) in Eq. (2.34):

$$\{F\} = \left[\lambda\right]^{-1}\{\lambda_M\}M. \tag{2.36}$$

When the i-th fiber reaches a particular value of reaction, the maximum one, called pull-out load, $F_{P,i}$, it starts to slip. This value is known and depends on the bridging law adopted, i.e., as will be clarified later, on the fiber type:

$$F_{P,i} = \tau_u \pi d_{f,i} w_C, \tag{2.37}$$

where τ_u is the bond shear strength of the fiber, $d_{f,i}$ is the fiber's diameter, w_C is the critical crack opening displacement. When the pull-out load is reached, the fiber progressively slips from the matrix. The crack opening is thus greater than zero, and the bridging force decreases, as predict by the most realistic bridging law adopted (Chapter 3). In this second phase, the reaction depends on the crack opening displacement, according to the slippage constitutive law of the fiber.

Considering the m active fibers, the problem can be partitioned into two parts. By naming f (free displacements) the slipping fibers, and c (constrained displacements) the elastic ones, one can write:

$$\begin{Bmatrix} w_f \\ w_c \end{Bmatrix} = \begin{Bmatrix} \lambda_{Mf} \\ \lambda_{Mc} \end{Bmatrix} M - \begin{bmatrix} \lambda_{ff} & \lambda_{fc} \\ \lambda_{cf} & \lambda_{cc} \end{bmatrix} \begin{Bmatrix} F_f \\ F_c \end{Bmatrix} \tag{2.38}$$

Differently of the elastic phase, characterized solely by static unknowns, in this case there are both kinematic and static unknowns. Indeed, the crack opening displacements, w_i, and the bridging forces, F_i, must be determined. The problem again requires $m = c + f$ additional conditions, that in this stage for c fibers are:

$$w_i = 0. \tag{2.39}$$

In the case of the f fibers, the bridging force is in turn a function of the crack opening displacements:

$$F_i = F(w_i), \tag{2.40}$$

where $F(w_i)$ is the force of the i-th fiber, evaluated by the slippage constitutive law adopted for the reinforcing phase. From the upper part of Eq. (2.38), and considering the conditions given by Eqs. (2.39) and (2.40), the m_c bridging elastic forces can be found:

$$\{F_c\} = \left[\lambda_{cc}\right]^{-1} \left\{ \{\lambda_{M,c}\} M - \left[\lambda_{cf}\right] \{F(w_f)\} \right\}. \tag{2.41}$$

Then, by introducing Eq. (2.41) into the lower part of Eq. (2.38), it is obtained:

$$\{w_f\} = \left\{ \{\lambda_{M,f}\} - \left[\lambda_{fc}\right]\left[\lambda_{cc}\right]^{-1}\{\lambda_{M,c}\} \right\} M + \left\{ \left[\lambda_{fc}\right]\left[\lambda_{cc}\right]^{-1}\left[\lambda_{cf}\right] - \left[\lambda_{ff}\right] \right\} \{F(w_f)\}, \tag{2.42}$$

where the f unknowns, the crack opening displacement $\{w_f\}$, are determined as a function of the applied bending moment, M.

Slippage constitutive law, based on experimental researches, are numerically implemented in the algorithm for steel fibers, straight or hooked hand. They are piecewise defined functions, as it will explained in next Chapter. For this reason, the determination of the crack opening displacements $\{w_f\}$, and the corresponding bridging forces $F_f = F(w_f)$, requires an iterative procedure.

2. 2. 5   Moment-rotation response

It is possible to find the crack propagation bending moment, by means of the Eq. (2.4), substituting the expressions of the stress intensity factor reported in Eq. (2.6) and Eq. (2.7). The scalar product of vectors is used for the summation, so the crack propagation condition becomes:

$$K_I = \frac{M}{h^{3/2}b} Y_M - \frac{\{Y_F\}^T \{F\}}{h^{1/2}b} = K_{IC} \tag{2.43}$$

The value of the fracture moment is:

$$M_{\mathrm{F}} = \frac{h^{3/2}b}{Y_{\mathrm{M}}}\left(K_{\mathrm{IC}} + \frac{\{Y_{\mathrm{F}}\}^{\mathrm{T}}\{F\}}{h^{1/2}b}\right) = \frac{h^{3/2}b}{Y_{\mathrm{M}}}K_{\mathrm{IC}} + \frac{h}{Y_{\mathrm{M}}}\{Y_{\mathrm{F}}\}^{\mathrm{T}}\{F\} = R_1 + R_2\{Y_{\mathrm{F}}\}^{\mathrm{T}}\{F\}, \quad (2.44)$$

where R_1 and R_2 are used to reduce the expression of the fracture moment.

For a given crack depth, a, and a given applied bending moment, M, the related bridging forces have been evaluated. Also the localized rotation of the cracked cross-section can be calculated by Eq (2.26). In matrix form:

$$\varphi = \lambda_{\mathrm{MM}}M - \{\lambda_{\mathrm{M}}\}^{\mathrm{T}}\{F\} \qquad (2.45)$$

When the fracture moment is achieved the crack depth increases, and the same calculations, regarding fracture moment and localized rotation are required for each crack advancement.

By this way, finally, the Bridged Crack model allows to describe the sectional response in terms of moment vs rotation. From these results, it is also possible to evaluate the load vs deflection response of the beam, taking into account also the elastic displacement of the beam midspan. This conversion, implemented in the numerical algorithm, will be discussed in detail in fourth Chapter.

Chapter 3

FIBER PULL-OUT BEHAVIOUR

3. 1   Introduction

Fibers represent the secondary phase of the FRC composite material. The mechanical and geometrical properties of the reinforcing fibers are fundamental to provide the synergism with the concrete matrix, which make the material an effective composite. The fibers are variable, both for material and geometry. They can be made of steel, polymeric materials as well as inorganic materials such as carbon, glass and natural materials (CNR, 2006). Moreover, the shape of the fiber can be undeformed (straight), with a round or flat section; there are also fibers with deformed profile, such as twisted or with hooked end. In Figure 3.1 different types of fibres are showed.

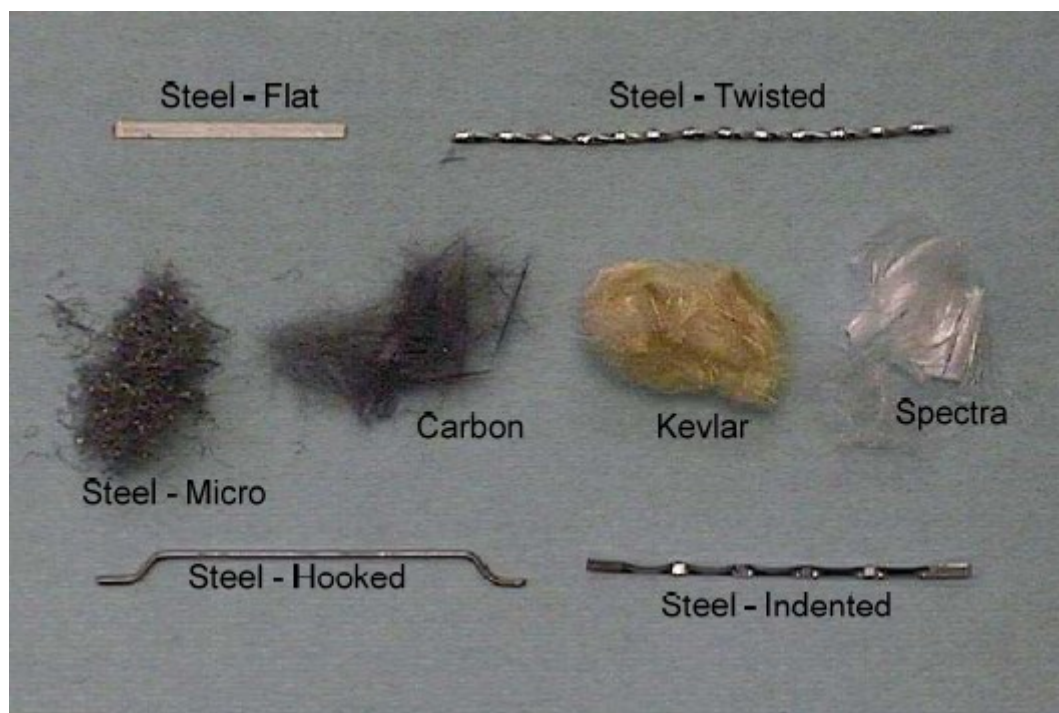**Figure 3.1 Different type of fibers (Figure from Naaman, 2008).**

Recent experimental works investigated the effects of the fiber addition in the concrete matrix, providing enhanced mechanical properties. The main reason behind the use of fiber reinforced composites is to contain cracking process. The fibers bridge the cracked parts of the matrix, thus delaying the sudden brittle failure of the structural

element. So, after the onset of the cracking process, the mechanical behaviour of FRC element is primarily governed by the interfacial bond stress response of the fibers, which is fundamental in this phase.

The bridging mechanism allows to increase the energy absorption during the fracture process. Moreover, the use of fibers significantly increases the tensile and flexural strength of the concrete material (ACI, 1988). Further experimental researches have also found an increase in the shear strength of the composite (Lim et al., 1999). On the other hand, the addition of fibers does not significantly affect the compressive strength and the Young's Modulus of the composite (ACI, 1993).

Considering the structural design of FRC members, the addition of fibers in concrete elements provides advantages both in Serviceability Limit States (SLS) and Ultimate Limit States (ULS): the FRC has the capability to contain the cracking process and enhance, thus, the durability of the structural elements (SLS); moreover, the increase of concrete bearing capacity improve the performance in ULS.

3. 2   Bridging mechanisms of the reinforcing fibers

Fiber pull-out tests measure the force required to pull out a fiber, embedded in a matrix, when it is subjected to uniaxial tension. These tests can be carried out applying the tensile force in one side or in double side; they can be also performed on a single fiber or in a multiple configuration. One-sided pull-out test has been performed mostly on single fiber, to investigate the properties of the matrix-fiber interface.

This work is focused on steel fibers, particularly on the straight and the hooked-end ones (Figure 3.2). Regarding the bridging mechanism of the straight steel fibers, a theoretical formulation was proposed by Naaman et al. (1991a), then validated with experimental pull-out tests (Naaman et al., 1991b). It will be shortly presented in this section.
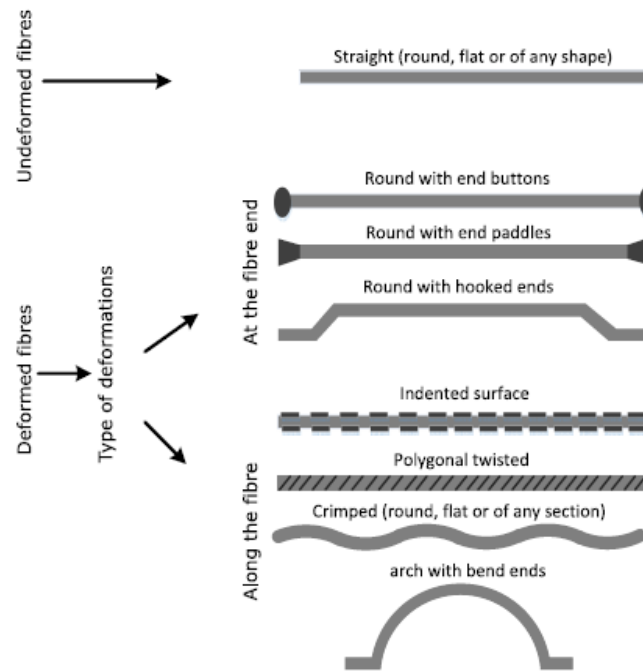
Figure 3.2 Different geometric shape of steel fibers (Figure from Abdallah, 2018).

A scheme of the slippage phenomenon, occurring during a typical pull-out test, is represented in Figure 3.3, where a fiber, embedded for a length l in a cementitious matrix, is subjected to a tensile force P. The latter monotonically increases during the test, providing a progressive debonding along the fiber-matrix interface. Once debonding occurs along the entire embedded length of the fiber, a progressive slippage of the fiber into the matrix occurred, with the consequent distribution of tangential stresses, mobilized at the fiber-matrix interface.

Figure 3.3 Free-body diagram of an element of fiber (data from Naaman et al., 1991b).

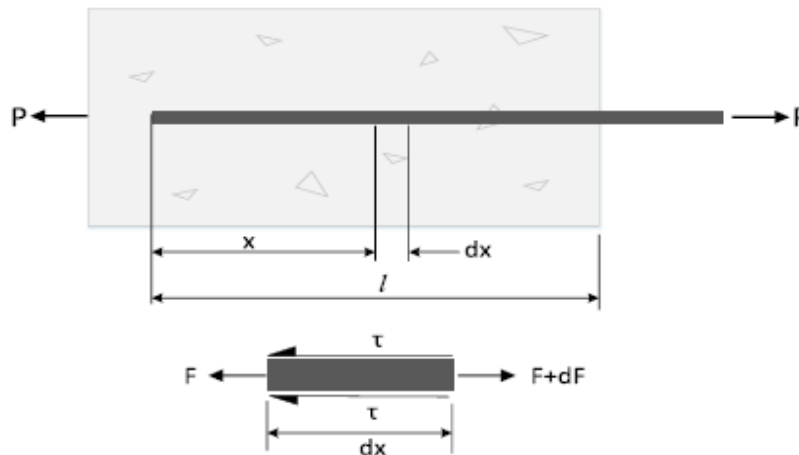An idealized stress-slip relationship in a straight fiber pull-out test was proposed by Naaman et al. (1991b), and it is showed in Figure 3.4.
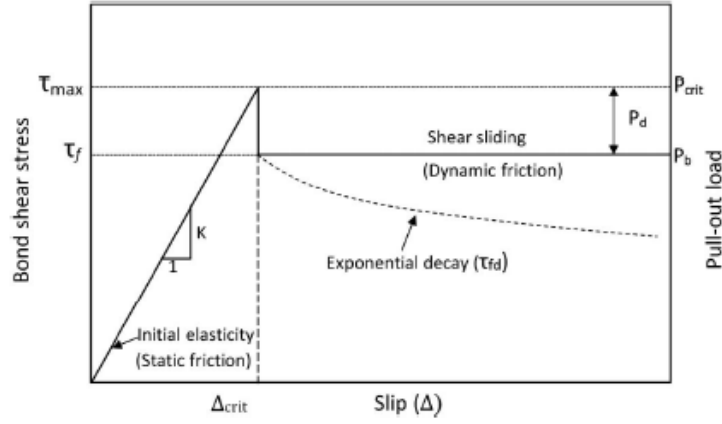

Figure 3.4 Assumed straight fiber bond shear stress versus slip relationship.
(Figure from Abdallah, 2018. Data from Naaman et al., 1991b).

The diagrams stars with a linear elastic range, until the maximum bond shear strength, $\tau_{\max}$, is reached. The corresponding pull-out force can be found as follow.

Considering the equilibrium of fiber element with a diameter of d_f (Figure 3.3), one can write:

$$\left(F + dF\right) - F = \tau \times 2\pi r \times dx \, , \tag{3.1}$$

$$\therefore \frac{dF}{dx} = \tau \cdot \psi \, , \tag{3.2}$$

$$\psi = \pi d_f \, . \tag{3.3}$$

The constitutive law, related to the Linear elastic branch, is defined as follows:

$$\tau = k\Delta \, , \tag{3.4}$$

where the slip, Δ, can be written as:

$$\Delta = \delta_f - \delta_m = \int_0^x \left[\varepsilon_f\left(x\right) - \varepsilon_m\left(x\right) \right] dx \, , \tag{3.5}$$

where δ_f and δ_m are the displacements in the fiber and the matrix respectively; ε_f and ε_m are the corresponding axial strains. By solving the Eq. (3.2) and substituting the previous expressions of τ and Δ, it is obtained:

$$\tau\left(x\right) = \frac{dF}{dx}\frac{1}{\psi} = \frac{P\lambda}{\psi}\left(Ae^{\lambda x} + Be^{-\lambda x}\right), \tag{3.6}$$

22

where $\lambda = \sqrt{KQ}$; with $K = (\psi k)/(A_m E_m)$ and $Q = 1 + A_m E_m / A_f E_f$, in which A_m and A_f are the section areas of the matrix and the fiber, E_m and E_f are their corresponding Young's moduli. The values of A and B can be found using the two boundary conditions, $F(l) = P$ and $F(0) = 0$.

The critical force is the load at $x = l$, corresponding to maximum value of interfacial shear stress:

$$P_{crit} = \frac{\psi \tau_{max}}{\lambda} \left[\frac{1 - e^{-2\lambda l}}{\left(1 - \frac{1}{Q}\right)\left(1 + e^{-2\lambda l}\right) + \left(\frac{1}{Q}\right) 2e^{-\lambda l}} \right]. \tag{3.7}$$

It is thus possible to individuate three stage of pull-out mechanism, for straight fibers (Figure 3.5):

1) *Elastic range*: when $P < P_{crit}$ fiber is completely bonded in the matrix. By solving the Eq. (3.5), it can found the slip displacement, and consequentially the expression of the gradient k :

$$\frac{P}{\Delta} = \left(\frac{\lambda A_m E_m}{Q - 2} \right)\left(\frac{1 + e^{-\lambda l}}{1 - e^{-\lambda l}} \right). \tag{3.8}$$

2) *Partial debonding stage*: when critical value of the pull-out load is reached, only a part of fiber is still bonded, and the force experiences a sudden decrease. The fiber bonded region allows to have a remaining pull-out force, namely P_b.

3) *Fully debonded and frictional pull-out stage*: fibre is totally debonded and its relative elastic elongation is neglected. The relation between the force and the slip becomes:

$$P = \psi \tau_{fd}(\Delta) \times (l - \Delta), \tag{3.9}$$

where $(l - \Delta)$ is the embedded length of the remaining fiber, τ_{fd} is the dynamic frictional shear stress. Pull-out tests conducted by Naaman et al. (1991b) led to a descending branch that is not linear, suggesting a decay in the frictional bond. So, the assumption that the bond shear stress remains steady after the bond strength

τ_{max} is not representative for large slips. Naaman et al. (1991b) found the expression of τ_{fd} with increasing slip:

$$\tau_{fd}\left(\Delta\right)=\tau_{fi}\frac{e^{-(\Delta-\Delta_0)^\eta-\xi e^{-(l)^\eta}}}{1-\xi e^{-(l-\Delta+\Delta_0)^\eta}}\times\frac{1-\exp\left[\dfrac{-2\upsilon_f\mu\left(l-\Delta+\Delta_0\right)}{E_f r_f\left(\dfrac{1+\upsilon_m}{E_m}\right)+\left(\dfrac{1-\upsilon_f}{E_f}\right)}\right]}{1-\exp\left[\dfrac{-2\upsilon_f\mu l}{E_f r_f\left(\dfrac{1+\upsilon_m}{E_m}\right)+\left(\dfrac{1-\upsilon_f}{E_f}\right)}\right]},\qquad(3.10)$$

where Δ_0 is the slip of the fiber at the end of stage 1, μ is the dynamic friction coefficient of the interface fiber-matrix, r_f is the fiber's radius, υ is the Poisson's coefficient, with subscript f and m for fiber and matrix, respectively. The damage coefficient ξ describes decay observed in the curve, and the the exponent $\eta=0.2$, for straight steel fiber.
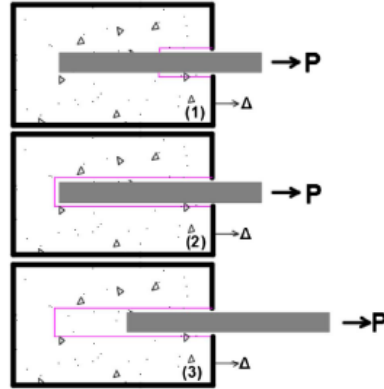
Figure 3.5 Pull-out behaviour of straight fiber (Stages 1-3).
(Figure from Abdallah, 2018).

More complex mechanisms are exhibit in pull-out tests by deformed shape of fiber (Figure 3.2). The hooked-end type is the most commonly employed, because these fibers are able to further enhance the energy absorption during the pull-out process. For this type of geometry, indeed, the pull-out mechanism provides other two additional stages, due to the development of two plastic hinges (PH1 and PH2) correspondingly to the end deformed region (Figure 3.6).
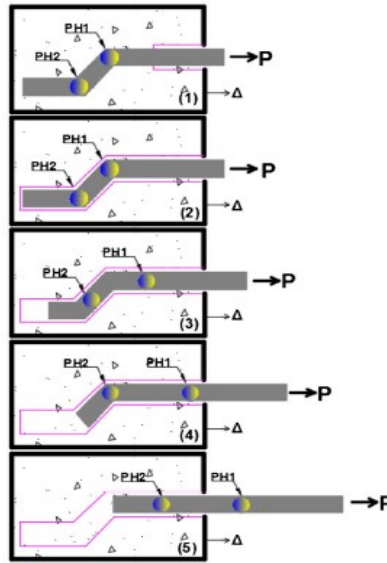
Figure 3.6 Pull-out behaviour of hooked-end fiber (Stages 1-5).
(Figure from Abdallah, 2018).

The difference between the two typical pull-out responses can be evaluated in Figure 3.7. The curves show the same elastic range, after which the straight fiber experiences the exponential decay, as previously described. On the contrary, the hooked-end fiber reaches a higher value of the pull-out force, due to the mechanical anchorage of the fiber end. After this maximum, the pull-out load starts to decrease due to the progressive mobilization of the PH1. When the first plastic hinge has straightened the fiber, it is placed in the straight part of the channel. Further straightening under PH2 is recognize in the slight increase in pull-out load at Stage 4 (Abdallah, 2018). Finally, when both the hooked-end are straightened, the fiber has reached the straight configuration, and the same exponential decay is found.

Figure 3.7 Pull-out response of straight fiber (Stages 1-3) and hooked-end fiber (Stages 1-5).
(Figure from Abdallah, 2018).

Moreover, the influence of fiber orientation and matrix strength, for hooked-end type, is extensively investigated by Robins e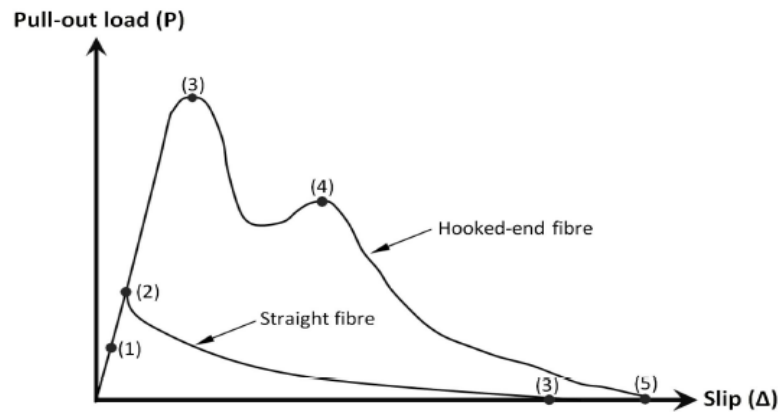t al. (2002) and Cunha et al. (2010). The results of the experimental researches suggest that: (i) increasing the matrix strength, and the embedded length, the critical value of the pull-out force increases; (ii) the embedded length must be greater than the hooked length to guarantee the employment of the mechanical anchorage; (iii) an inclination of 10-20 degrees provides the maximum value of energy absorption.

3. 3   Slippage constitutive laws

In order to define an analytical bridging-law, both for straight and hooked-end steel fibers, the experimental results obtained by Abdallah et al. (2019) are analysed.

The pull-out tests on single steel fiber were carried out using the cube of 100×100×100 mm (Figure 3.8). In each specimen, one steel fibre, characterized by a length of 60 mm, was placed carefully in a hole made through the bottom of moulds. The embedded length (L_E) was one half of the fibre length, i.e., equal to 30 mm.
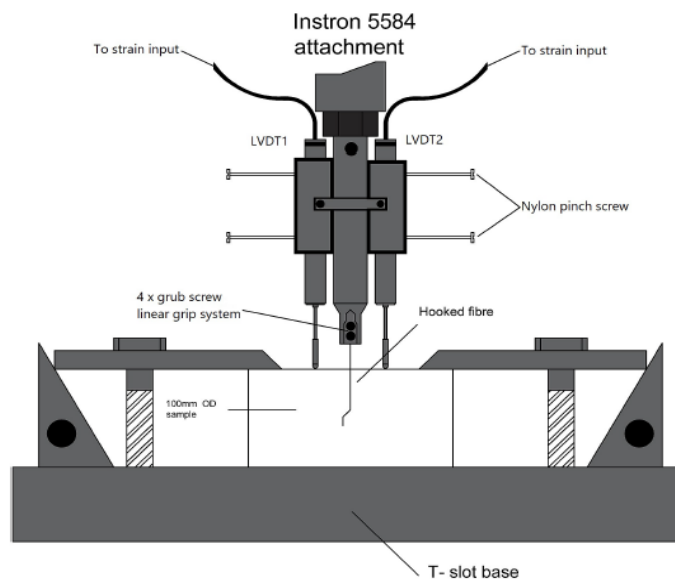
Figure 3.8 Pull-out test setup (Abdallah et al, 2019).

The pull-out tests were performed using a specially designed grip system, as showed in Figure 3.8, which was attached to an Instron 5584 universal testing machine. The grips were designed such that the forces applied to the fibre provided a true reflection of the real situation experienced by fibers bridging a crack. Two linear variable differential transformer (LVDT) transducers were used to measure the distance travelled by the steel

fiber relative to the concrete face during testing. A displacement rate of 10 mm/s was adopted for all the tests.

In the case of straight fibers the experimental results are reported in Figure 3.9.
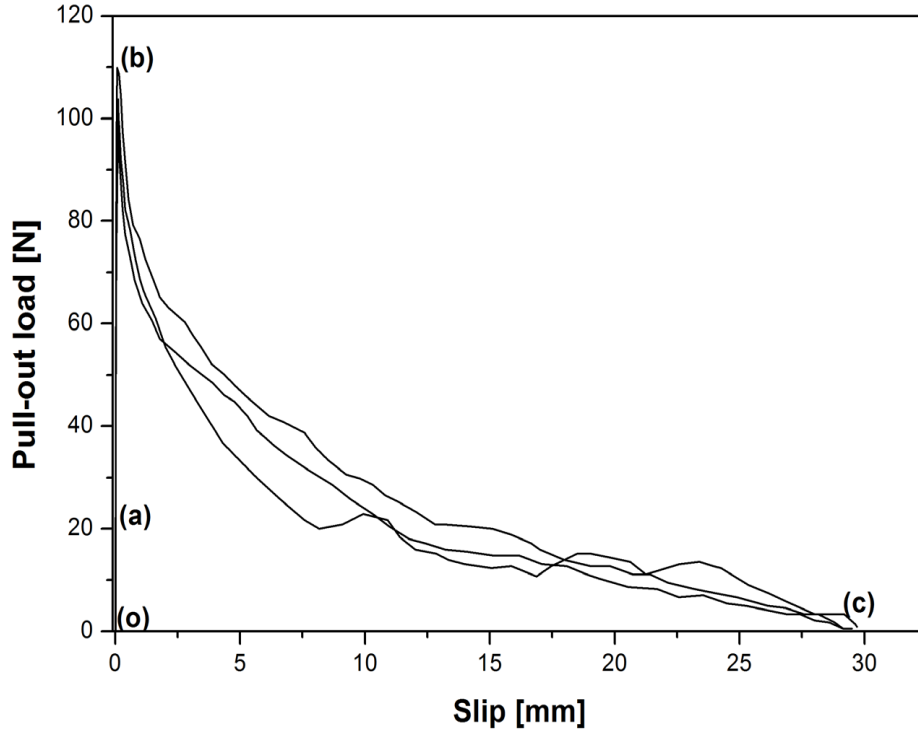
Figure 3.9 Pull-out tests on straight steel fiber results.
(Abdallah, 2019).

In all the tests, the three stages discussed in the previous section can be recognized. The average of the results are normalized: the load respect to the maximum pull-out force, $F_P = 110N$, the slip respect to the fiber embedded length, $w_C = 30mm$. This normalization provides the so-called slippage law per "unit embedded length" of the fiber. By the graphical analysis of the normalized experimental data, the function in Figure 3.10 is thus obtained. The corresponding analytical formulation is defined as follow:

1. For $0 < \dfrac{w_i}{w_C} \leq 4.174 \times 10^{-3}$

$$\frac{F_i}{F_P} = 1, \tag{3.11}$$

2. For $4.174 \times 10^{-3} < \dfrac{w_i}{w_C} < 1$

$$\frac{F_i}{F_P} = e^{-5.204\left(\frac{w_i}{w_C}\right)}, \qquad (3.12)$$

3. For $\dfrac{w_i}{w_C} \geq 1$

$$\frac{F_i}{F_P} = 0. \qquad (3.13)$$
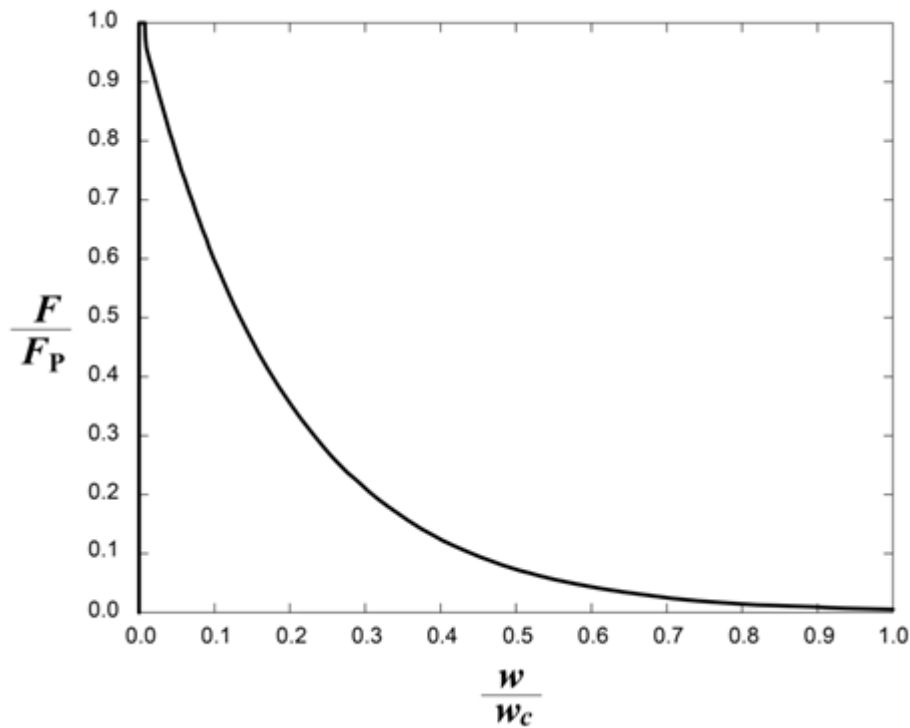
Figure 3.10 Normalized pull-out curve of straight steel fiber adopted in the Bridged Crack model.

The pull-out of straight fiber is reproduced using an exponential decay law after the peak load. It is worth noting that the actual fiber pull-out behaviour starts with a linear-elastic branch, but it is analytically reproduced through the vertical line before the peak load. Indeed, even if it is not exactly corresponding to the experimental results, it is coherent with the compatibility condition of the Bridged Crack model ($w_i = 0$ for $F_i < F_P$), and the comparisons with experimental data (Chapters 6 and 7) confirm the effectiveness of this assumption.

The same procedure is conducted for the hooked-end steel fibers; experimental pull-out tests results (Abdallah, 2019) are represented in Figure 3.11.
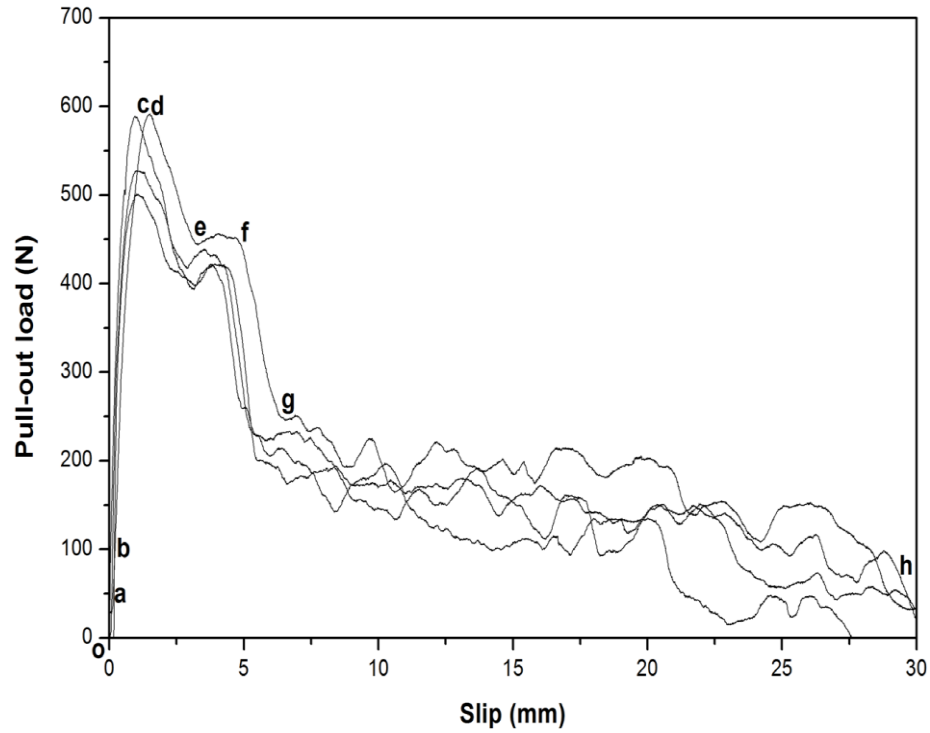
Figure 3.11 Pull-out tests on hooked-end steel fiber results.
(Abdallah, 2019).

Also in this case, the experimental curves show the typical phases connected to the hooked-end fiber geometry. Particularly, it is remarkable the effect of the two plastic hinges correspondently to the c-d, and e-f curve's range. In order to generalize the pull-out response, the average of the results are again normalized: the load respect to the maximum pull-out load, $F_{\mathrm{p}} = 590N$, the slip respect to the embedded length, $w_{\mathrm{C}} = 30mm$. By the graphical analysis of the normalized experimental data, the function in Figure 3.12 is thus obtained. The corresponding analytical formulation is defined as follow:

1. For $0 < \dfrac{w_{\mathrm{i}}}{w_{\mathrm{C}}} \leq 0.05$

$$\frac{F_{\mathrm{i}}}{F_{\mathrm{P}}} = 1, \qquad\qquad (3.14)$$

2. For $0.05 < \dfrac{w_{\mathrm{i}}}{w_{\mathrm{C}}} < 0.1$

29

$$\frac{F_\mathrm{i}}{F_\mathrm{P}} = 1 - 4\left(\frac{w_\mathrm{i}}{w_\mathrm{C}} - 0.05\right),$$ (3.15)

3. For $0.1 \le \dfrac{w_\mathrm{i}}{w_\mathrm{C}} \le 0.15$

$$\frac{F_\mathrm{i}}{F_\mathrm{P}} = 1,$$ (3.16)

4. For $0.15 < \dfrac{w_\mathrm{i}}{w_\mathrm{C}} \le 0.18$

$$\frac{F_\mathrm{i}}{F_\mathrm{P}} = 1 - 13.33\left(\frac{w_\mathrm{i}}{w_\mathrm{C}} - 0.15\right)$$ (3.17)

5. For $0.18 < \dfrac{w_\mathrm{i}}{w_\mathrm{C}} < 1$

$$\frac{F_\mathrm{i}}{F_\mathrm{P}} = 0.4 \cdot e^{-5.204\left(\frac{w_\mathrm{i}}{w_\mathrm{C}} - 0.18\right)}$$ (3.18)

6. For $\dfrac{w_\mathrm{i}}{w_\mathrm{C}} \ge 1$

$$F_\mathrm{i} = 0$$ (3.19)
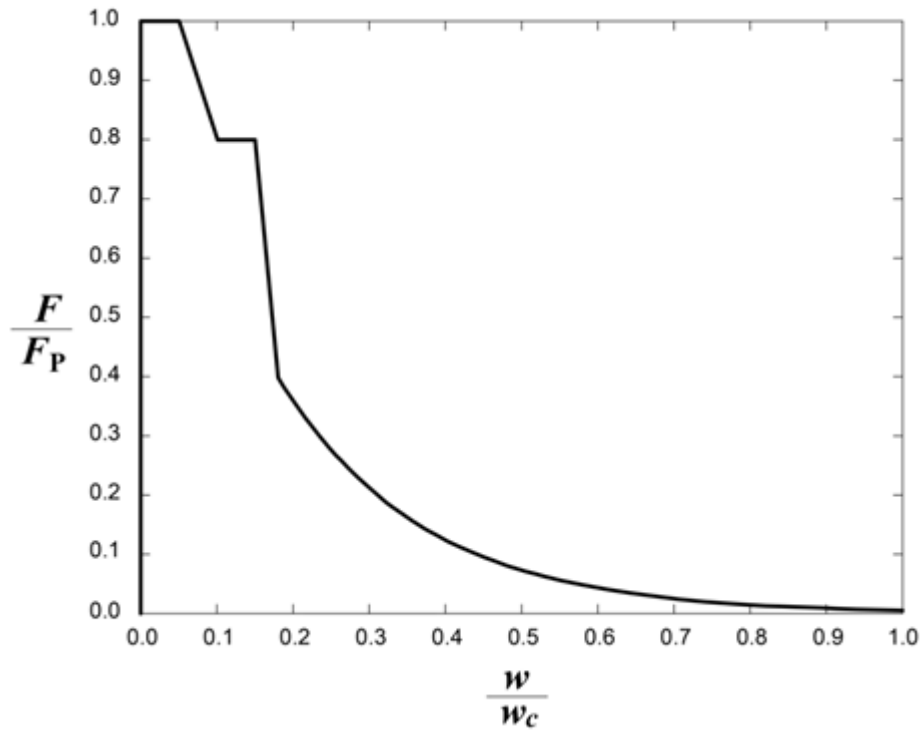
Figure 3.12 Normalized pull-out curve of hooked-end steel fiber adopted in the Bridged Crack model.

The pull-out response of the hooked-end is analytically reproduced taking into account the experimental peculiarity: the effect of the plastic hinges is considered through the insertion of the two plateaus. As for the straight fibers, the elastic range of the behaviour is approximated.

These two constitutive slippage laws are currently implemented in the algorithm of the Bridged Crack model, since steel straight and hooked-end steel fibers are the most commonly employed in practical applications. Further pull-out tests on other fiber's types could be considered, to identify the different bridging laws, and enlarge the applicability of the model.

Chapter 4

NUMERICAL ALGORITHM

4.1   Crack Length Control Scheme (CLCS)

The algorithm of the Bridged Crack model is implemented in MATLAB language.
The initialization requires input parameters, which are divided into the following groups:

- Beam geometry
  - b → section thickness
  - h → section depth
  - a_0 → initial crack depth (or ξ_0 → normalized initial crack depth)
  - L → beam length
  - S → beam span

- Fiber geometry
  - d_f → fiber diameter
  - l_f → fiber length
  - V_f → fiber volume fraction
  - n → number of fibers modelling
  - ρ → fiber specific weight
  - c_1 → position of the first fiber (or ζ_{min} → normalized position)
  - c_n → position of the last fiber (or ζ_{max} → normalized position)
  - w_c → average embedded length of the fiber

- Matrix material
  - E → matrix Young's modulus
  - K_{IC} → matrix fracture toughness
  - f_{ck} → matrix characteristic cylindrical compression strength

32

- Fiber material

  ➢ f_u → fiber ultimate tensile strength

  ➢ τ_u → fiber bond shear strength

- Process control

  ➢ a_{max} → final crack depth (or ξ_{max} → normalized final crack depth)

  ➢ $\Delta\xi$ → normalized crack depth increment at each calculation step

The actual number of fibers is evaluated through the Eq. (2.1). However, it can be really high, affecting the computation time. To avoid this problem, the input data include the fibers number; the numerical code is able to define an equivalent bridging force, in order to ensure the equivalence between the two distributions. The effect of different numbers of fibers modelling regards the local phenomenon, whereas the global response remains unchanged, as discussed in section 5.3.

As seen in Chapter 2, the fibers are considered evenly spaced in the entire ligament, between c_1 and c_n (Figure 2.1). The constitutive law is defined, on the basis of the type of reinforcement. For straight and hooked-end steel fibers the bridging laws implemented are illustrated in section 3.2.

After the input data initialization, at each *k-th* step the crack depth is increased as follow:

$$\xi^{(k+1)} = \xi^{(k)} + \Delta\xi, \tag{4.1}$$

where the apex (k) indicates the generic calculation step.

The fiber is defined active if:

$$\zeta_i < \xi^{(k)}. \tag{4.2}$$

The algorithm is based on the following steps:

1. Data initialization ;

2. Actual crack depth. At the first step it is assumed equal to a_0 ;

3. Compute the *m* active fibers;

4. Compute compliances;

5. Initialize n_c and n_f. At the first step, it is assumed $n_c = m$, $n_f = 0$;

6. Computed the m bridging actions $\{F\}$, through Eq. (2.36) if $n_c = m$, or Eq. (2.41).

    6a. loop entering conditions:

$$\text{If } F_i > F_\text{P} \text{ or } F_i < -F_\text{P}, \rightarrow F_i = F_\text{P};$$

    Update n_c and n_f, and return to step 6.

7. Compute the m crack opening displacements $\{w\}$, with Eq. (2.42).

    7a. loop entering condition:

$$\text{If } F_i > F(w_i), \rightarrow F_i = F(w_i);$$

    Update n_c, n_f, F_i, and return to step 3.

10. Compute localized rotation of the cracked cross-section, φ, with Eq. (2.43);

11. Compute crack propagation moment, M_F, with Eq. (2.45);

11. Save results: $M_\text{F}, \{w\}, \{F\}, \varphi$;

12. Update crack depth, $\xi^{(k+1)} = \xi^{(k)} + \Delta\xi$ and return to step 2 if $\xi^{(k+1)} < \xi_\text{stop}$.

12. Computation of TPBT or FPBT force and the corresponding deflection;

13. Plot $M - \varphi$ and $P_\text{TPBT} - \delta_\text{TPBT}$ values or $P_\text{FPBT} - \delta_\text{FPBT}$.

The process is thus controlled by increasing the crack length (Crack Length Control Scheme). Using this technique, the discontinuous phenomena characterizing the post-cracking response, i.e., snap-back and snap-through instabilities, are described by the model, as extensively described by Carpinteri and Accornero (2019).

4.2 Load-deflection curves

The conversion from $M - \varphi$ to $P - \delta$ response, for three-point bending test (TPBT) and four-point bending test (FPBT), is developed starting from the simple schemes of Figures 4.1 and 4.2. The superposition principle is applied, because the displacement

measured at the beam midspan is the result of two contributes: the beam elastic deflection, δ_{el}, and the rigid localized one, δ_ϕ, due to the localized rotation of the cracked section.
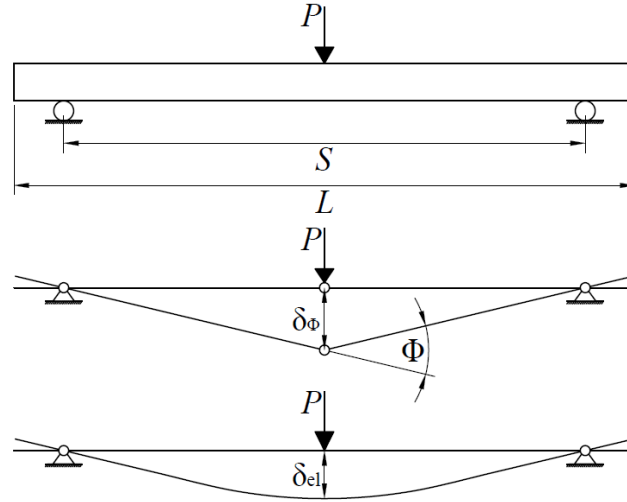
Figure 4.1 Evaluation of the beam displacement in case of three-point bending test.
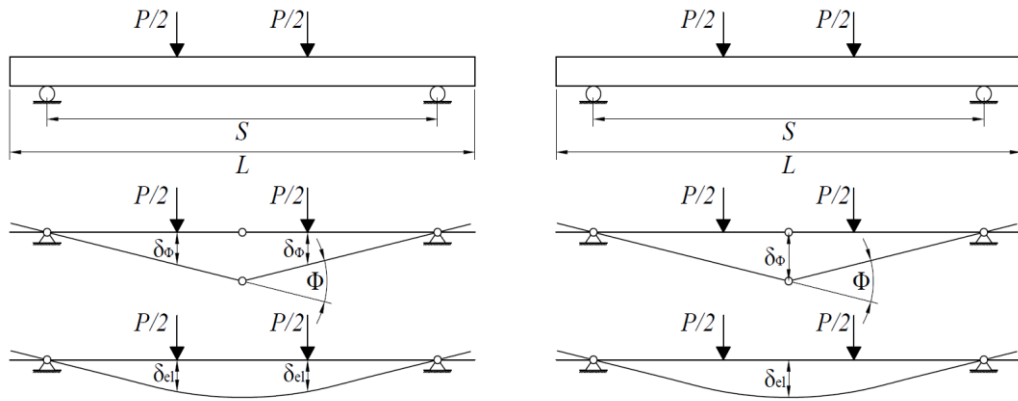
(a) Test with loaded point deflection control   **(b) Test with midspan deflection control**

Figure 4.2 Determination of the beam displacement in case of four-point bending test.

Regarding the three point bending test (Figure 4.1), the values of midspan load and deflection are calculated as follow:

$$P = \frac{4M}{L} \ ,$$
(4.3)

$$\delta = \delta_{el} + \delta_{\phi} = \frac{PS^3}{48EI} + \frac{\phi S}{4} \; , \tag{4.4}$$

where S is the beam span, I the inertia of the cross section, and E the Young's Modulus.

Similar considerations can be drawn for the four-point bending test controlled by the loaded point deflection, Figure 4.2 scheme (a). The application points of the forces divides the beam span into three equal parts; with this supposition, the value of the load and the corresponding deflection is computed.

$$P = \frac{6M}{L} \; , \tag{4.5}$$

$$\delta = \delta_{el} + \delta_{\phi} = \frac{5PS^3}{108EI} + \frac{\phi S}{6} \; . \tag{4.6}$$

If the test is controlled by the midspan deflection, the above expressions can be rewritten:

$$P = \frac{6M}{L} \; , \tag{4.7}$$

$$\delta = \delta_{el} + \delta_{\phi} = \frac{23PS^3}{1296EI} + \frac{\phi S}{4} \; . \tag{4.8}$$

4.3   Mechanical parameter

As seen in section 4.1, the input parameters of the model are the starting point of the analysis.

The fracture toughness of the matrix, its Young's Modulus, and the fiber's bond shear can be evaluated by empirical expressions, as functions of the average cylindrical compression strength of the matrix. The first one gives the fracture toughness; it was proposed by John R. and Shah S. P. (1989):

$$K_{IC} = 0.06 \left(f_{ck} \right)^{0.75} \; , \tag{4.9}$$

where the physical dimensions of f_{ck} are $\left[\text{MPa} \right]$ and of K_{IC} are $\left[\text{MPa}\sqrt{\text{m}} \right]$.

The second one provides the value of the Young's Modulus, still as a function of the average cylindrical compression strength of the concrete, as suggested by EUROCODE 2 (UNI EN 1992-1-1), Table 3.1.

$$E_{cm} = 22000 \left(\frac{f_{cm}}{10} \right)^{0.3} , \qquad (4.10)$$

where the physical dimensions of E_{cm} are $\left[MPa \right]$ and of f_{cm} are $\left[MPa \right]$.

The last one allows to evaluate the bond shear stress (*Fib* Model Code 2010):

$$\tau_u = 0.1 \sqrt{f_{cm}} \qquad (4.11)$$

where the physical dimensions of τ_u are $\left[MPa \right]$ and of f_{cm} are $\left[MPa \right]$.

4.4   Numerical errors

The predicted response is strongly affected by the increment $\Delta \xi$ and by the distance between the crack tip and the closest active fiber. This issue is due to the shape function $Y_P \left(\xi, \zeta_i \right)$, that provides a singularity for $\xi = \zeta_i$. In order to avoid this problem, the following conditions are imposed in the numerical code:

$$\Delta \xi = 0.005 , \qquad (4.12)$$

$$\xi - \zeta_i > 0.05 \Delta \xi . \qquad (4.13)$$

Typical examples of numerical problems related to the crack depth increment, $\Delta \xi$, are shown in Figure 4.3 and Figure 4.4. The curves are obtained imposing the same mechanical and geometrical parameters, but different values of $\Delta \xi$. Particularly, in the first case (Figure 4.3), the excessive peak is the consequence of a too low $\Delta \xi$ (0.0005). On the other hand, the second picture is found using a too high $\Delta \xi$ value (0.05), so the peak is too low that cannot be recognizable. A more realistic solution is obtained when the value of Eq. (4.15) is adopted, and the corresponding result is shown in Figure 4.5.
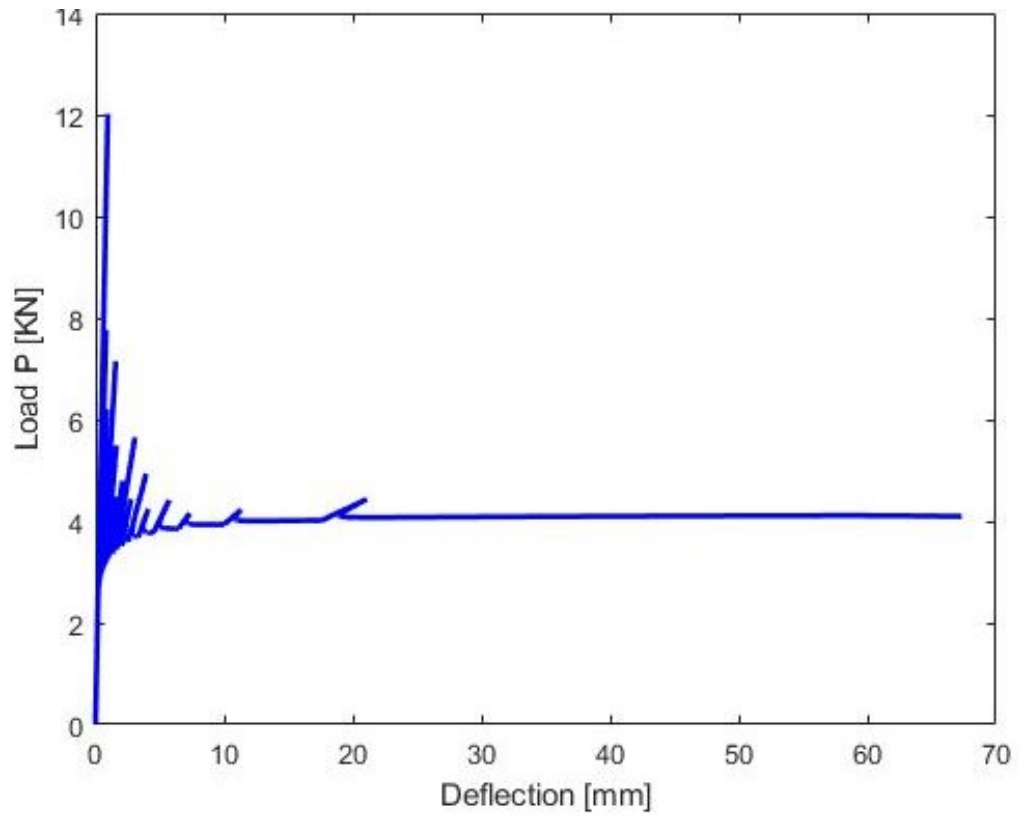
Figure 4.3 Load deflection curve obtained with a value of $\Delta\xi$ =0.0005.
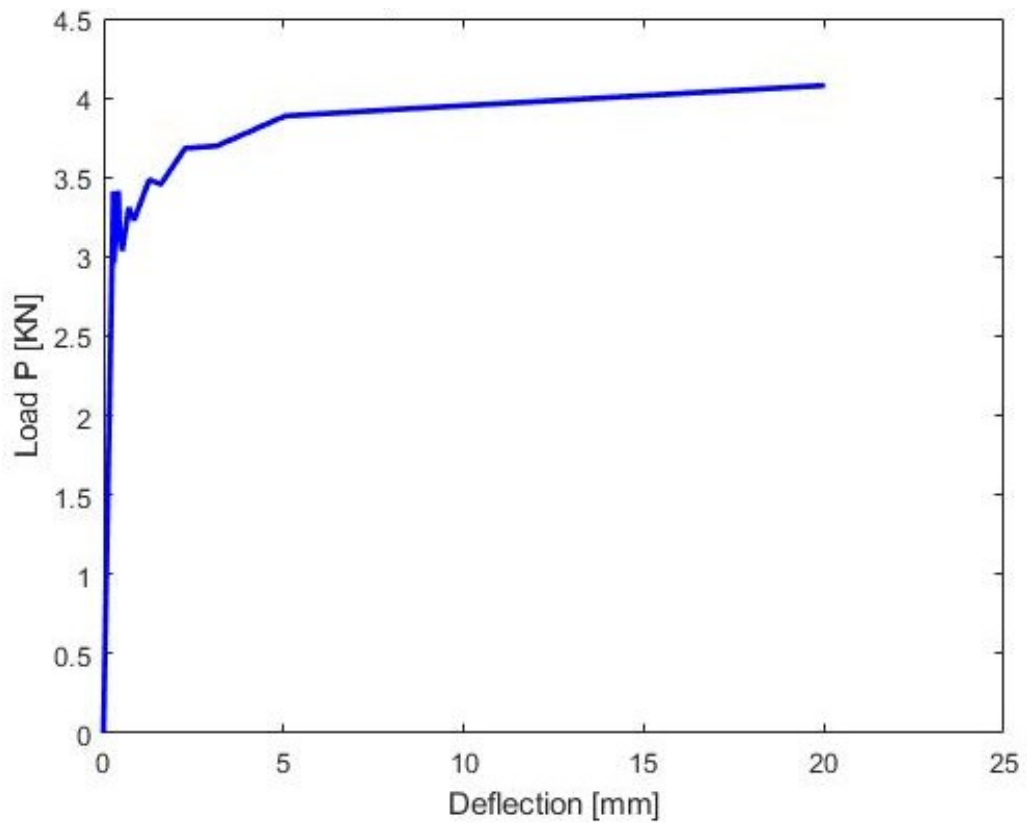
Figure 4.4 Load deflection curve using the value of $\Delta\xi$ =0.05.
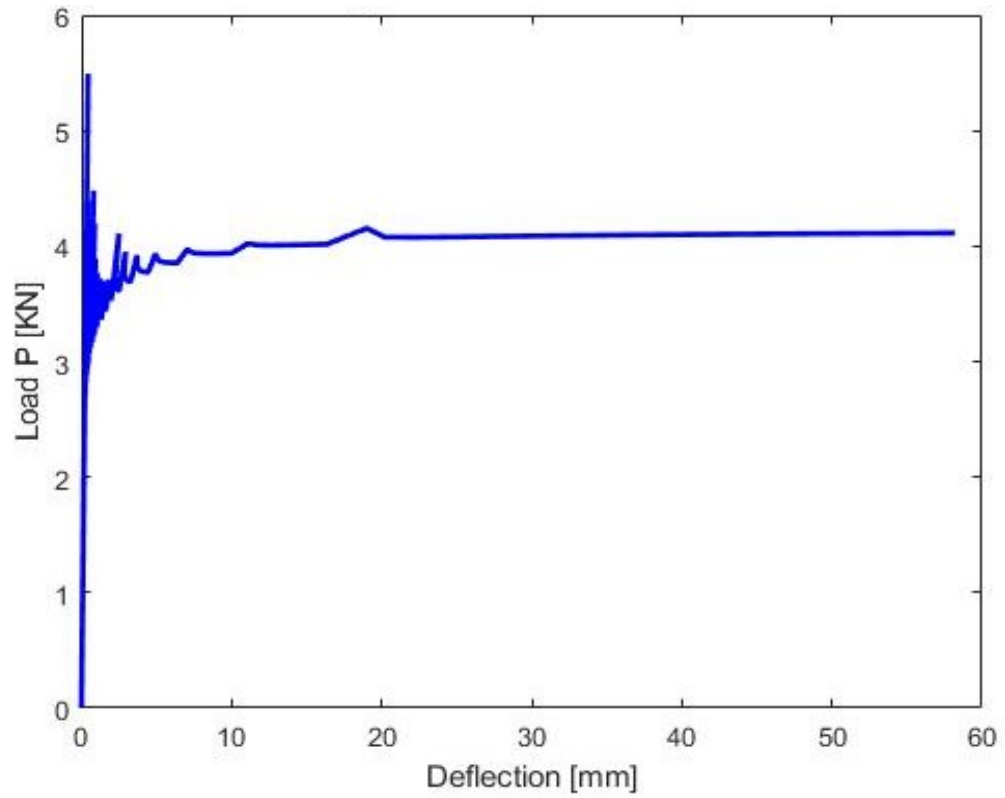
Figure 4.5 Load deflection curve using the value of $\Delta\xi$ =0.005.

Chapter 5

DIMENSIONAL ANALYSIS

5.1   Buckingham's π Theorem

Dimensional analysis is a method to define the functional dependence between physical quantities that are relevant for a certain phenomenon under investigation. The Buckingham's π theorem (Buckingham, 1915) states that the functional dependence between a certain number of variables can be reduced to obtain a set of dimensionless groups (*Pi* groups), which describe synthetically the physical phenomenon. The form of the functional dependence is still unknown, and it has to be defined by means of experimental tests.

The application of the π Theorem requires the definition of all the variables involved in the phenomenon. Among these, the output parameter, q_0, is a function of a number of variables:

$$q_0 = f(q_1, q_2, \ldots q_n; s_1, s_2, \ldots s_m; r_1, r_2, \ldots r_k),\tag{5.1}$$

where q_i are quantities with independent physical dimension; the dimensions of parameters s_i can be, instead, expressed as products of powers of the dimensions of the parameters q_i. The r_i quantities are dimensionless.

The product of *n* dimensionally independent are considered:

$$q_1^{\alpha_{10}} q_2^{\alpha_{20}} \ldots q_n^{\alpha_{n0}} = \prod_{i=1}^{n} q_i^{\alpha_{i0}},\tag{5.2}$$

to make dimensionless the output parameter, with a suitable choice of α_{i0}. By this way, all the s_i quantities can be transformed in dimensionless variables, as follow:

$$\frac{q_0}{q_1^{\alpha_{10}} q_2^{\alpha_{20}} \ldots q_n^{\alpha_{n0}}} = \tilde{f}\left(\frac{s_1}{q_1^{\alpha_{11}} q_2^{\alpha_{21}} \ldots q_n^{\alpha_{n1}}}, \frac{s_2}{q_1^{\alpha_{12}} q_2^{\alpha_{22}} \ldots q_n^{\alpha_{n2}}}, \ldots, \frac{s_m}{q_1^{\alpha_{1n}} q_2^{\alpha_{2n}} \ldots q_n^{\alpha_{nm}}}; r_1, r_2, \ldots r_k \right)\tag{5.3}$$

These dimensionless groups are called Π_1, Π_2, $\Pi_3,...,\Pi_m$; the functional relationship can thus be reduced to the much more compact form:

$$\Pi_0 = \tilde{i} \qquad \Pi_3,...,\Pi_m ; r_1 , r_2 , ... r_k) = 0 \qquad (5.4)$$

5.2 Dimensional analysis of FRC beam flexural response

In this section, the Buckingham's π theorem is applied to describe the flexural behaviour of a FRC beam, in the framework of the continuous Bridged Crack model.

Considering the local behaviour of the mid-span cross section, it is assumed to be governed by the following physical variables, listed along with their physical dimensions:

- M_F $[F][L]$, crack propagation moment;

- φ $[-]$, localized rotation;

- K_{IC} $[F][L]^{-1.5}$, matrix fracture toughness;

- σ_P $[F][L]^{-2}$, fictitious axial stress of the fiber;

- V_f $[-]$, fiber volume ratio

- E $[F][L]^{-2}$, matrix Young's modulus;

- w_C $[L]$, average embedded length of the fibers;

- n $[-]$, the exponent of bridging law decay;

- h $[L]$, beam depth;

- b $[L]$, beam thickness;

- a_0 $[L]$, initial crack depth.

The functional dependence between these parameters can be put into the following general form:

$$f\left(M_F, \varphi, K_{IC}, \sigma_P, V_F, E, w_C, n, h, b, a_0\right) = 0 \qquad (5.5)$$

Among all the parameters, crack propagation moment, M_F, and localized rotation, φ, can be considered as the output parameters of the phenomenon, while the other ones as input data. The ultimate stress of the fiber, σ_P, and the average embedded length of the fiber, w_C, are assumed as independent quantities, for sake of simplicity, in this work.

41

Actually, experimental pull-out tests point out an increase in the maximum pull-out force, with an increase in the embedded length of the fiber into the matrix (Robins, 2002).

The fundamental physical dimensions considered are force $[F]$ and length $[L]$, since the flexural response is assumed independent by time $[t]$ and temperature $[T]$. The matrix toughness K_{IC} and the beam depth h are assumed as the fundamental set of dimensionally independent variables.

By applying the Theorem, the relationship between the cross sectional bending moment and the localized rotation can be thus described by the following equation in dimensionless form:

$$f\left(\frac{M_F}{K_{IC}h^{1.5}b}, \varphi, \frac{\sigma_P\sqrt{h}}{K_{IC}}, V_F, \frac{E\sqrt{h}}{K_{IC}}, \frac{w_C}{h}, n, \frac{b}{h}, \frac{a_0}{h}\right) = 0 \qquad (5.6)$$

Replacing some quantities, with the corresponding product, one can obtain (Carpinteri et al.,1996):

$$f\left(\frac{M_F}{K_{IC}h^{1.5}b}, \varphi, \frac{V_f\sigma_P\sqrt{h}}{K_{IC}}, \frac{Ew_C}{K_{IC}\sqrt{h}}, n, \frac{b}{h}, \frac{a_0}{h}\right) = 0. \qquad (5.7)$$

The bridging law is defined, on the basis of fiber type, as seen in Chapter 3. Also the geometrical properties of the beam are fixed. Under these assumptions, the functional relationship can be written as follows:

$$f\left(\frac{M_F}{K_{IC}h^{1.5}b}, \varphi, \frac{V_f\sigma_P\sqrt{h}}{K_{IC}}, \frac{Ew_C}{K_{IC}\sqrt{h}}\right) = 0. \qquad (5.8)$$

The $M-\varphi$ response, in conclusion, can be defined by means of two dimensionless parameters, named N_P and N_W.

The first one, i.e. N_P, shows this general expression:

$$N_P = \frac{V_f\sigma_P\sqrt{h}}{K_{IC}}. \qquad (5.9)$$

In the FRC composites, the ultimate strength is the pull-out tension. If it is expressed as a function of the pull-out force, i.e., the maximum bridging action exhibit by the fiber, the previous equation can be written:

$$N_{\mathrm{P}} = \frac{\sum_{i=1}^{n} P_{\mathrm{P,i}}}{K_{\mathrm{IC}} b \sqrt{h}}. \tag{5.10}$$

Moreover, if it assumes that the maximum reclosing force is that in Eq. (5.11), the N_{P} expression can be rewritten.

$$P_{\mathrm{P,i}} = \tau_{\mathrm{u}} \pi d_{\mathrm{f}} \frac{l_{\mathrm{f}}}{2}, \tag{5.11}$$

$$\sigma_{\mathrm{P}} = \frac{P_{\mathrm{P}}}{A_{\mathrm{i}}} = \tau_u 2 \left(\frac{l_{\mathrm{f}}}{d_{\mathrm{f}}} \right), \tag{5.12}$$

$$N_{\mathrm{p}} = 2V_{\mathrm{f}} \frac{\tau_{\mathrm{max}}}{K_{\mathrm{IC}}} \sqrt{h} \left(\frac{l_{\mathrm{f}}}{d_{\mathrm{f}}} \right) = V_{\mathrm{f}} \frac{\tau_{\mathrm{u}} \sqrt{h}}{K_{\mathrm{IC}}} \left(2\lambda_{\mathrm{f}} \right), \tag{5.13}$$

where l_{f} is the fiber length, d_{f} is the fiber diameter, and λ_{f} is the fiber *aspect ratio*. Thus, since the dominant role of the slippage phenomenon respect to the yielding in FRC composites, the ultimate force is expressed as a function of the shear pull-out stress. Consequentially, in the brittleness number related to the FRC also a geometrical characteristic of the fiber is involved.

The second dimensionless parameter has the following expression:

$$N_{\mathrm{W}} = \frac{E w_{\mathrm{C}}}{K_{\mathrm{IC}} \sqrt{h}}, \tag{5.14}$$

which depends on the equivalent embedded length of the fiber. Comparing Eqs. (5.9) and (5.14) an opposite dependence of the two parameters on the specimen size is found.

Both the parameters affect the post-cracking behaviour of the composite. More precisely, N_{P} mainly affects the so called stage II of the post-cracking phase, which can range from catastrophic to strain hardening. By increasing N_{P}, called also *reinforcement brittleness number*, it is possible to individuate the transition N_{P} value, N_{PC}, the critical

one. It is fundamental to define the minimum reinforcement volume ratio, taking into account the dependence of the specimen size.

The second dimensionless parameter becomes relevant in case of $N_\text{P} \geq N_\text{PC}$. Under this hypothesis, indeed, the FRC flexural behaviour shows a post-cracking strain-hardening regime, and only a sufficiently high value of N_W guarantees the stability of the ductile behaviour. On the other hand, a low N_W value conducts to a globally brittle response: the stage II undergoes a dramatic contraction, anticipating the softening branch. This problem in FRC structural elements is often related to a low fiber embedded length.

The crucial role of these dimensionless parameters to define the $M - \phi$ response curve will be clarified in next section, with parametrical analysis conducted.

5.3 Parametrical analysis

The influence of key-parameters on the mechanical response of the FRC beams in bending is investigated through numerical simulations of Three Point Bending Test (TPBT). They are conducted by means of the Bridged Crack model Algorithm, implemented in MATLAB language. The analyses are divided into five groups, depending on the parameter investigated. The first three groups are related to the dimensionless parameters, N_P and N_W. The other two are focused on the minimum reinforcing condition.

- **INFLUENCE OF N_W ON SOFTENING BRANCH**

To understand the role of the dimensionless parameter related to the fiber embedded length, three TPBT numerical simulations are conducted. Particularly, three different values of N_P are chosen (1.3, 1, and 0.7), for each of these the effect of N_W changing is evaluated (ranging from 2032 to 203).

Geometrical and mechanical properties assumed for the prismatic specimen are summarized in Table 5.1. The slippage constitutive law of hooked-end fiber is considered.

Beam thickness	b	[cm]	15
Beam depth	h	[cm]	15
Notch depth	a_0	[cm]	1.5
Dimensionless notch depth	a_0/h	[/]	0.1
Beam span	S	[cm]	45
Beam length	L	[cm]	50
Young's modulus	E	[MPa]	31500
Fracture toughness	K_{IC}	[kg/cm$^{1.5}$]	70
Concrete compressive strength	f_{cm}	[MPa]	33
Fiber diameter	d_f	[cm]	0.075
Fiber length	l_f	[cm]	3.5
Fiber tensile strength	f_u	[MPa]	1100
Number of fibers modelling	n	[/]	100

Table 5.1 Geometrical and mechanical properties of the FRC specimen.
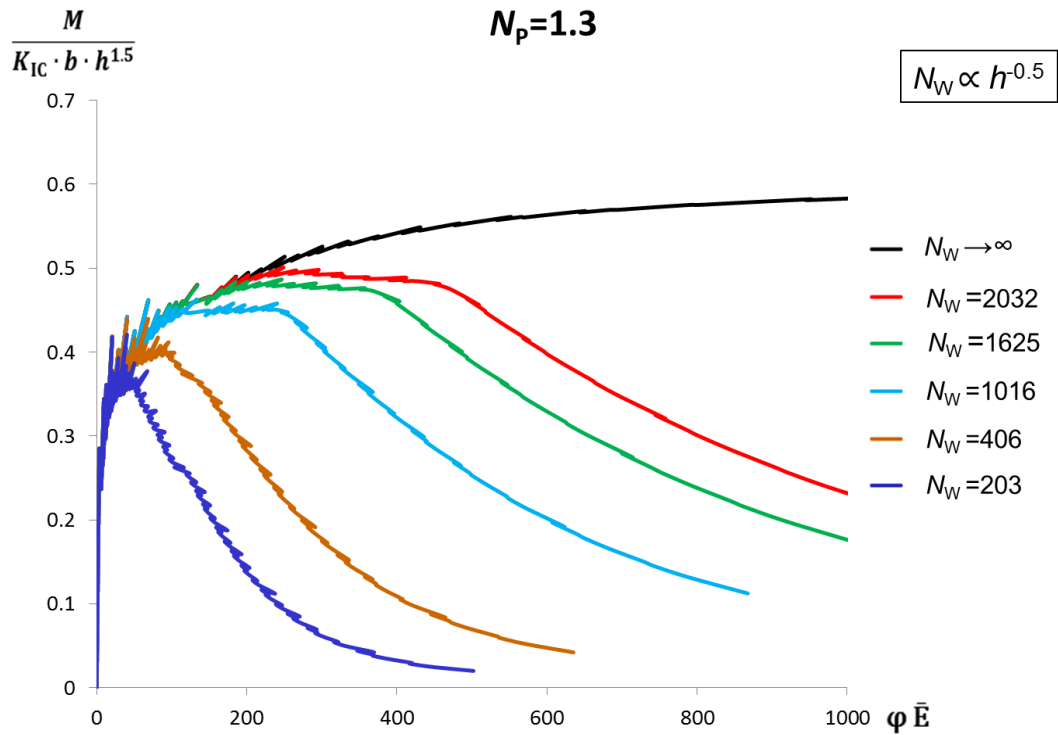
Figure 5.1 Influence of N_W on softening branch .

Figure 5.2 Influence of N_W on softening branch .

Figure 5.3 Influence of N_W on softening branch .
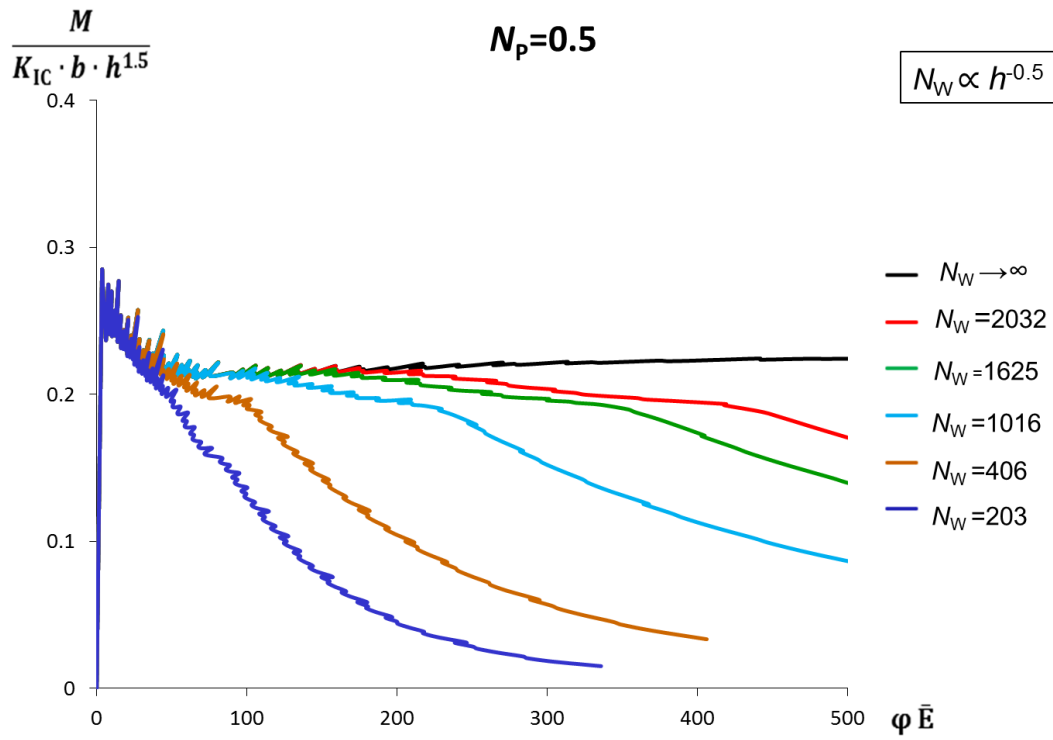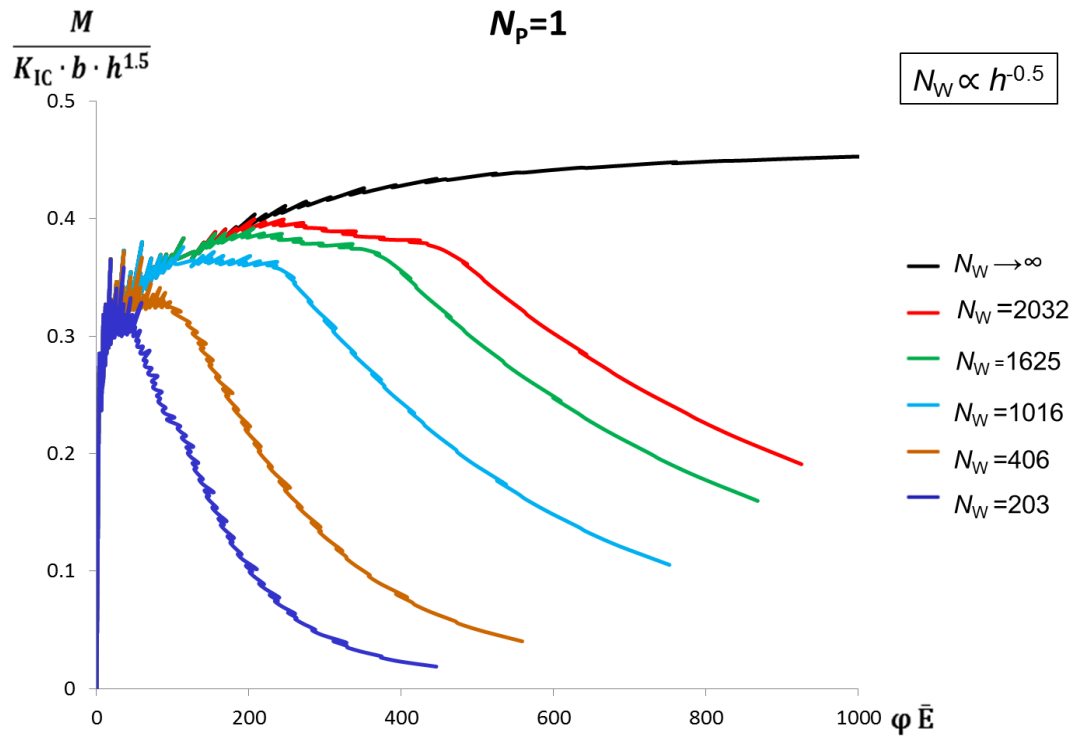
As seen in this first group of numerical simulation, the three stages of the flexural response are clearly recognizable. The black curves, which do not show softening branch, are referred to an idealized continuous reinforcement, with rigid perfectly-plastic constitutive bridging law ($w_\mathrm{c} \to \infty$). In each diagram, the linear-elastic (stage I) is not affected by the parameter N_W; the second and third stages, characterizing the post-cracking phase of the composite are, instead, really different from red curves to the blue ones. In second stage, indeed, bridging phenomenon starts and it is affected by the embedded length of the fiber (described by N_W); in third stage, finally, slippage mechanism prevails with respect to the bridging one, so the softening branch occurs. It is surprising to see the influence of N_W looking at the global response, when the brittleness number provides a ductile behaviour (Figures 5.1 and 5.2). By decreasing N_W, indeed, the so called stage II results evidently reduced and the softening branch prematurely appeared; also the bearing capacity of the element is reduced. The post-peak response, until the softening branch, thus, change from perfectly-plastic, stable (red curves) to brittle, unstable (blue curves).

On the other hand, if N_P is not enough to provide a ductile behaviour, the post-cracking response is brittle, since the cracking bending moment is not exceeded, regardless of N_W (Figure 5.3).

- **INFLUENCE OF N_P ON POST-PEAK RESPONSE**

The reinforcement brittleness number is extremely relevant in the design process, to guarantee a ductile post-cracking flexural response of the structural element; as seen in previous analysis looking at the black curves, it is the unique dimensionless parameter in case of continuous reinforcement, such as ordinary steel rebars (Carpinteri, 1984; Bosco and Carpinteri, 1990). His role is preeminent also in discontinuous reinforcement, even if not enough alone to provide a stable post-peak response. In the following numerical TPBT simulation, four different N_W values are considered: 203, 406, 1016, 2032; for each of these the effect of N_P changing is evaluated. The four N_W values are obtained assuming the embedded length equal to: 0.1 l_f, 0.25 l_f, 0.4 l_f, and 0.5 l_f. Geometrical and mechanical properties assumed for the prismatic specimen are reported in Table 5.2. The slippage constitutive law of hooked-end fiber is considered.

Beam thickness	b	[cm]	15
Beam depth	h	[cm]	15
Notch depth	a_0	[cm]	1.5
Dimensionless notch depth	a_0/h	[/]	0.1
Beam span	S	[cm]	45
Beam length	L	[cm]	50
Young's modulus	E	[MPa]	31500
Fracture toughness	K_{IC}	[kg/cm$^{1.5}$]	70
Concrete compressive strength	f_{cm}	[MPa]	33
Fiber diameter	d_f	[cm]	0.075
Fiber length	l_f	[cm]	3.5
Fiber tensile strength	f_u	[MPa]	1100
Number of fibers modelling	n	[/]	100

Table 5.2 Geometrical and mechanical properties of the FRC specimen.
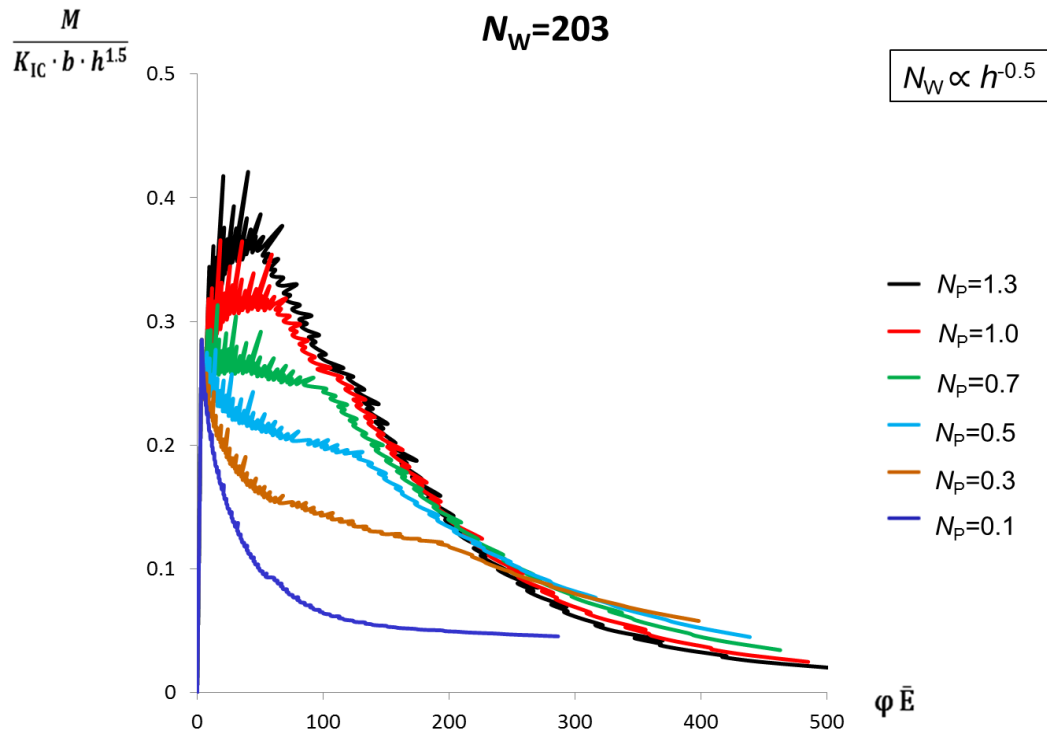
Figure 5.4 Influence of N_P on post-cracking stage.
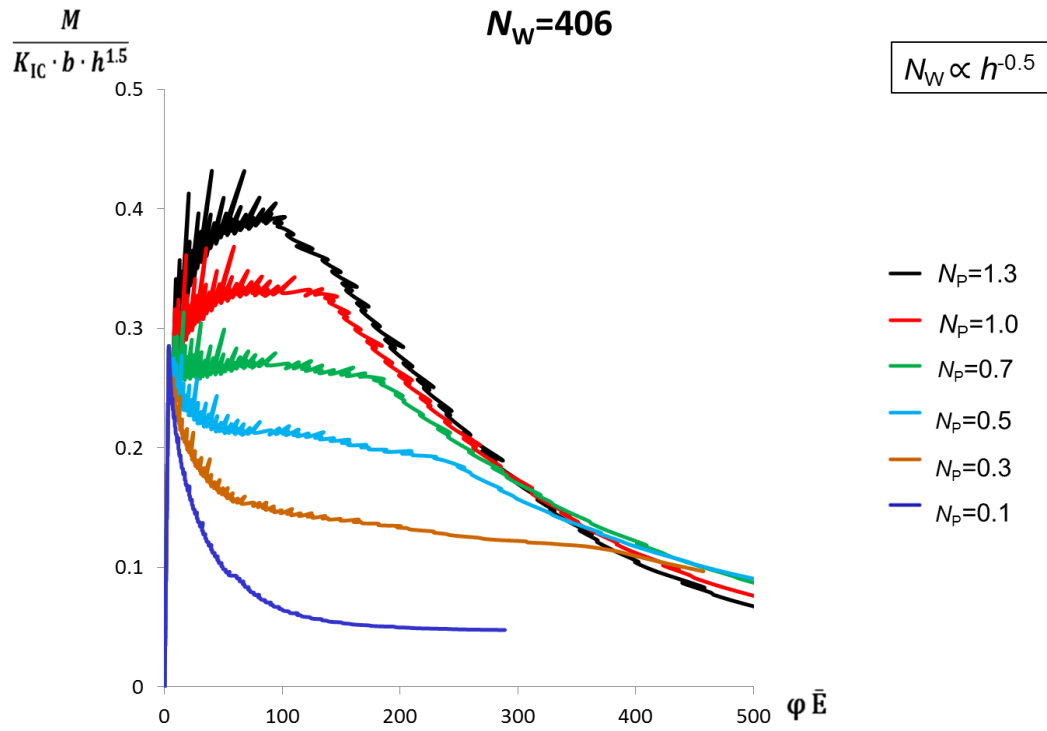
Figure 5.5 Influence of N_{P} **on post-cracking stage.**
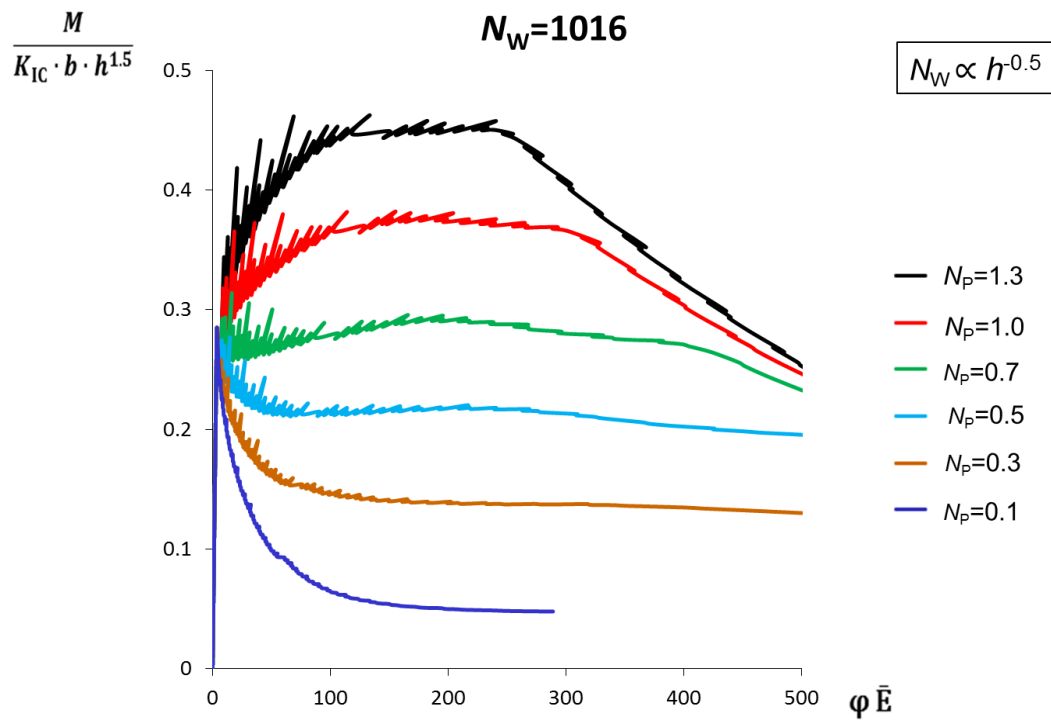
Figure 5.6 Influence of N_{P} **on post-cracking stage.**
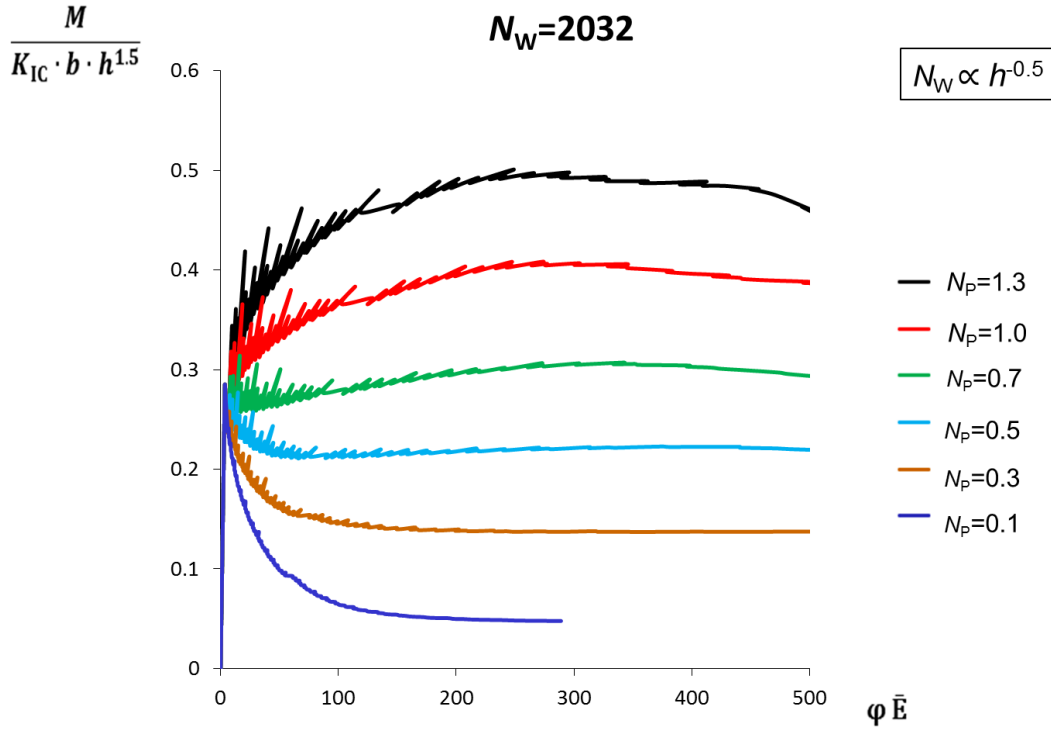
Figure 5.7 Influence of N_P on post-cracking stage.

For each value of N_W, the curves collapse in an unique final softening branch. It is evident especially for lowest value of N_W, in Figure 5.4. For the highest value of N_W, instead, N_P is fundamental to define a brittle (blue curve) or a ductile (above green curve) global response: the high plastic deformability of the specimen, provides by the N_W value, removes almost at all the softening branch.

- **SCALE EFFECT**

The two dimensionless parameters show an opposite dependence on the specimen size, as it can be evaluated in Eq. (5.9) and Eq. (5.14). It means that an increase of the specimen characteristic dimension provides a positive effect in the immediately post-peak stage (governs by N_P), whereas the consequentially decrease of N_W value provides a premature appearance of the softening branch. The following numerical simulations of TPBT are able to clarify these considerations.

Five different values of beam depth are considered (ranging from 2.5 cm to 30 cm), for each of these the effect of N_P and N_W changing on the global response is evaluated. However, it is worth notice that their product is not affected by the specimen size. Geometrical and mechanical properties assumed for the prismatic specimen are reported in Table 5.3. The slippage constitutive law of hooked-end fiber is implemented.

Beam thickness	b	[cm]	15
Dimensionless notch depth	a/h	[/]	0.1
Beam span	S	[cm]	45
Beam length	L	[cm]	50
Young's modulus	E	[MPa]	31500
Fracture toughness	K_{IC}	[kg/cm$^{1.5}$]	70
Concrete compressive strength	f_{cm}	[MPa]	33
Fiber diameter	d_f	[cm]	0.075
Fiber length	l_f	[cm]	3.5
Fiber tensile strength	f_u	[MPa]	1100
Number of fibers modelling	n	[/]	100

Table 5.3 Geometrical and mechanical properties of the FRC specimen.
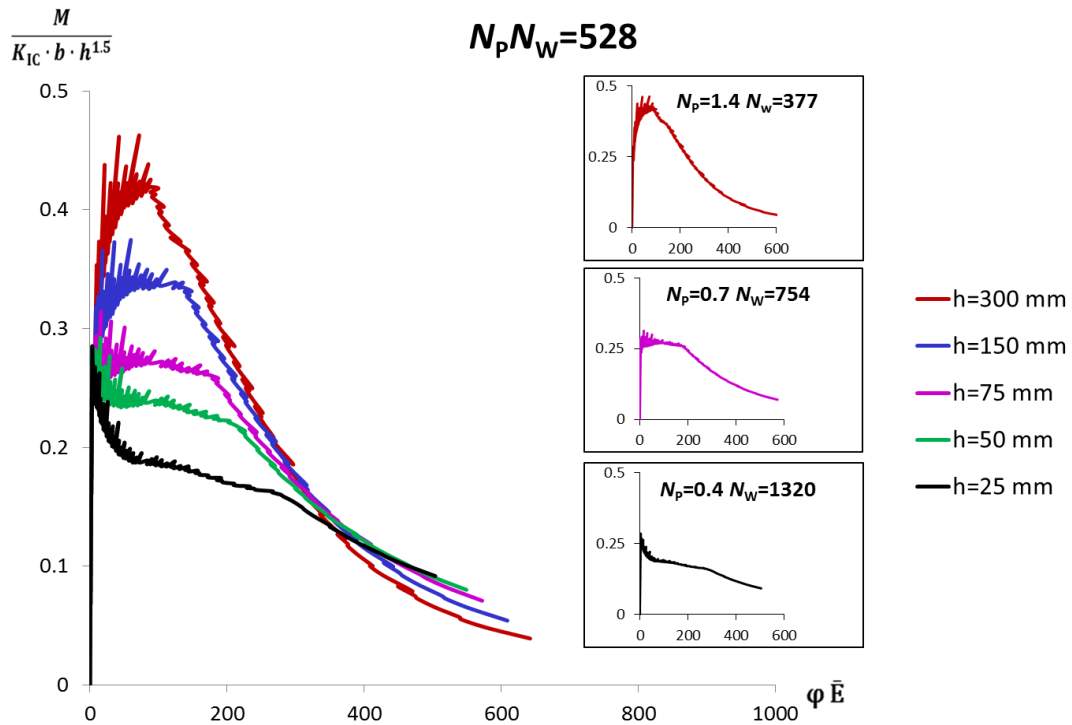
Figure 5.8 Influence of specimen size on post-cracking stage.

51

In the Figure above, from the black curve to the fuchsia one it is observable a first brittle-to-ductile transition. It is due to the increase of N_P with the beam depth. His further increase conducted to a strain hardening range, immediately after the crack onset. On the contrary, lower N_W values, consequent to an increase in the specimen size, make the global response increasingly unstable. Thus, a ductile-to-brittle transition occurs from the fuchsia curve to the red one.

- **INFLUENCE OF N_W ON THE DUCTILE-TO-BRITTLE TRANSITION AND NOTCH-SENSITIVITY OF N_{PC}**

In the section 5.2 the N_{PC} is introduced, as the brittleness number corresponding to the minimum reinforcement condition. Since the parametrical analysis just seen, it can guess that the critical value of N_P depends also on N_W. In this group of numerical simulations this dependence is discussed. Three different values of N_W are chosen: 610, 1016, 2033; for each of these the ductile-to-brittle transition is provided. Moreover, the analysis are carried out for three different notch depths ($0.1h$, $0.05h$, and $0.03h$) to investigate also the so called *notch-sensitivity* of N_{PC}. Geometrical and mechanical properties assumed for the prismatic specimen are reported in Table 5.4. The slippage constitutive law of hooked-end fiber is implemented.

Beam thickness	b	[cm]	15
Beam depth	h	[cm]	15
Beam span	S	[cm]	45
Beam length	L	[cm]	50
Young's modulus	E	[MPa]	31500
Fracture toughness	K_{IC}	[kg/cm$^{1.5}$]	70
Concrete compressive strength	f_{cm}	[MPa]	33
Fiber diameter	d_f	[cm]	0.075
Fiber length	l_f	[cm]	3.5
Fiber tensile strength	f_u	[MPa]	1100
Number of fibers modelling	n	[/]	100

Table 5.4 Geometrical and mechanical properties of the FRC specimen.
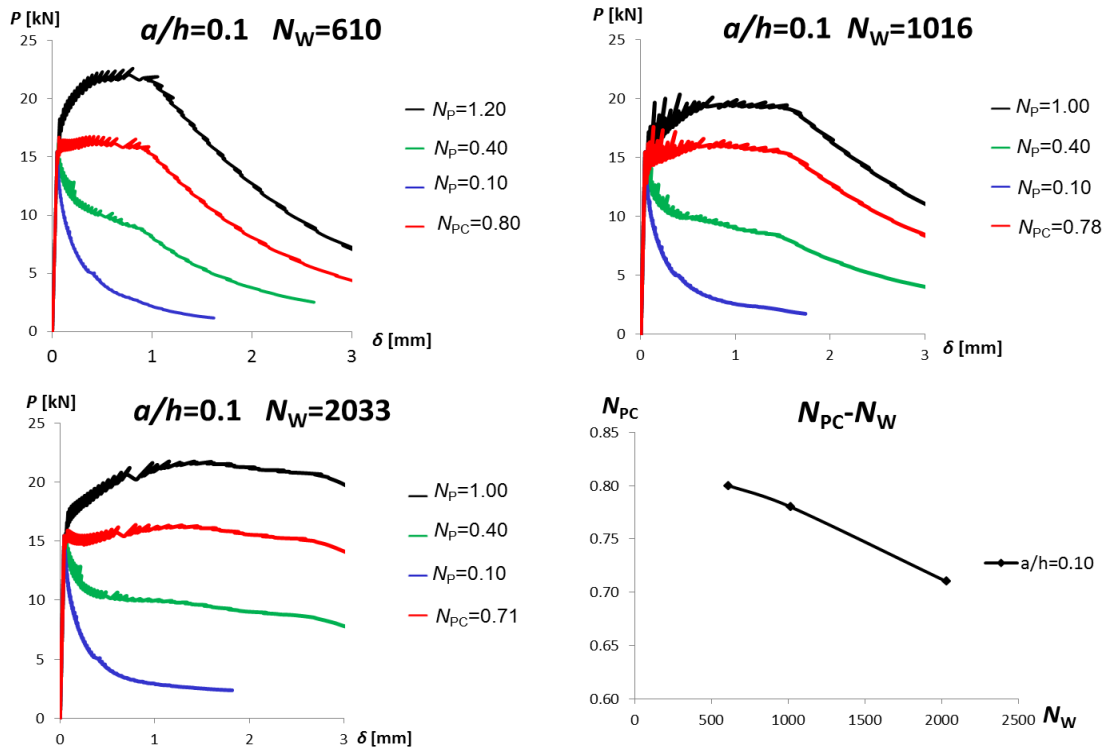
Figure 5.9 Influence of N_{W} on the Ductile-to-Brittle transition (N_{PC}).
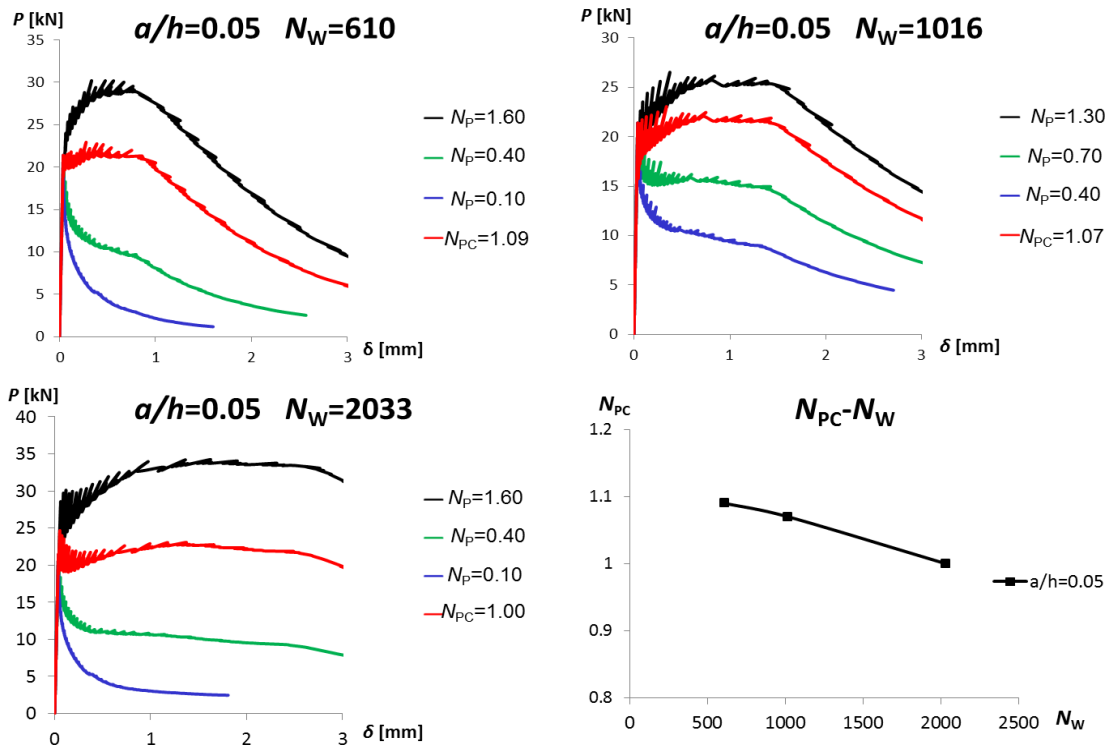
Figure 5.10 Influence of N_{W} on the Ductile-to-Brittle transition (N_{PC}).

53
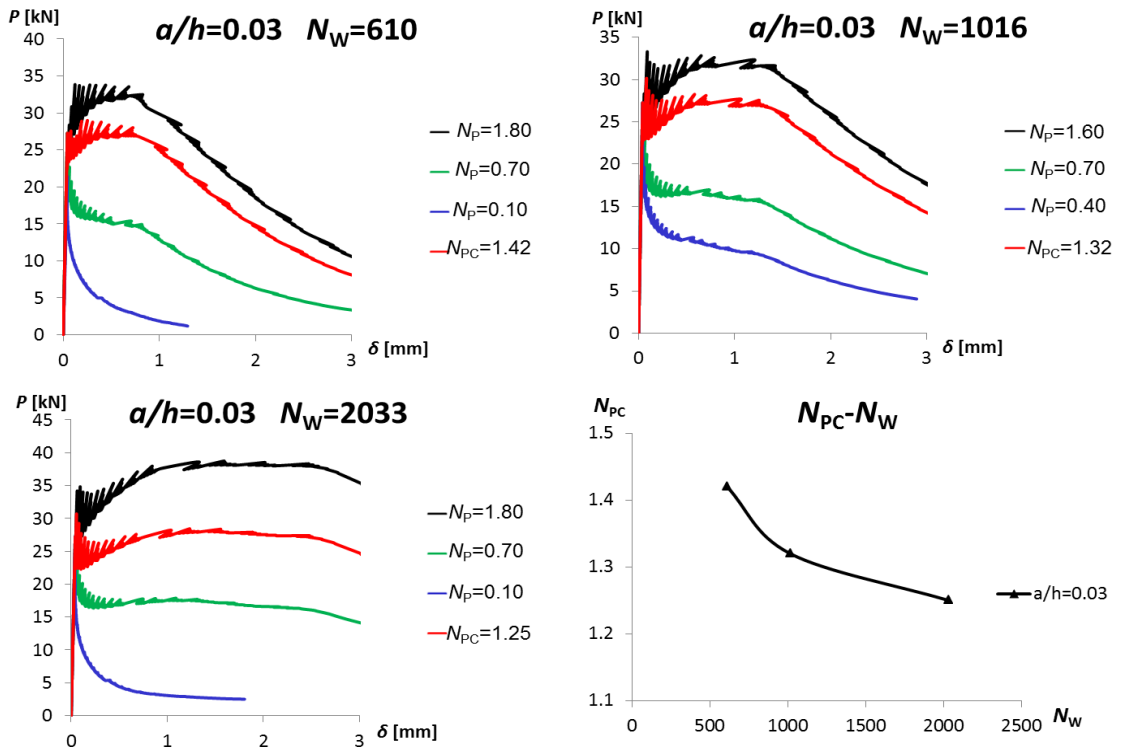
Figure 5.11 Influence of N_{W} on the Ductile-to-Brittle transition (N_{PC}).

In the Figures 5.9, 5.10 and 5.11, red curves show the $P-\delta$ response corresponding to the minimum reinforcement condition (characterised by N_{PC}). Each Figure contains also the graph of the relation N_{W} - N_{PC}, for the specific notch depth. It is worth noting that, in this circumstance, only the immediately post-cracking behaviour (governs by N_{P}) is considered to define the minimum reinforcement. Actually, in the design process, also the plateau's extension must be taken into account to choose the minimum required reinforcement. By this way, also the length of the fibers (related to N_{W}) could be a design parameter.
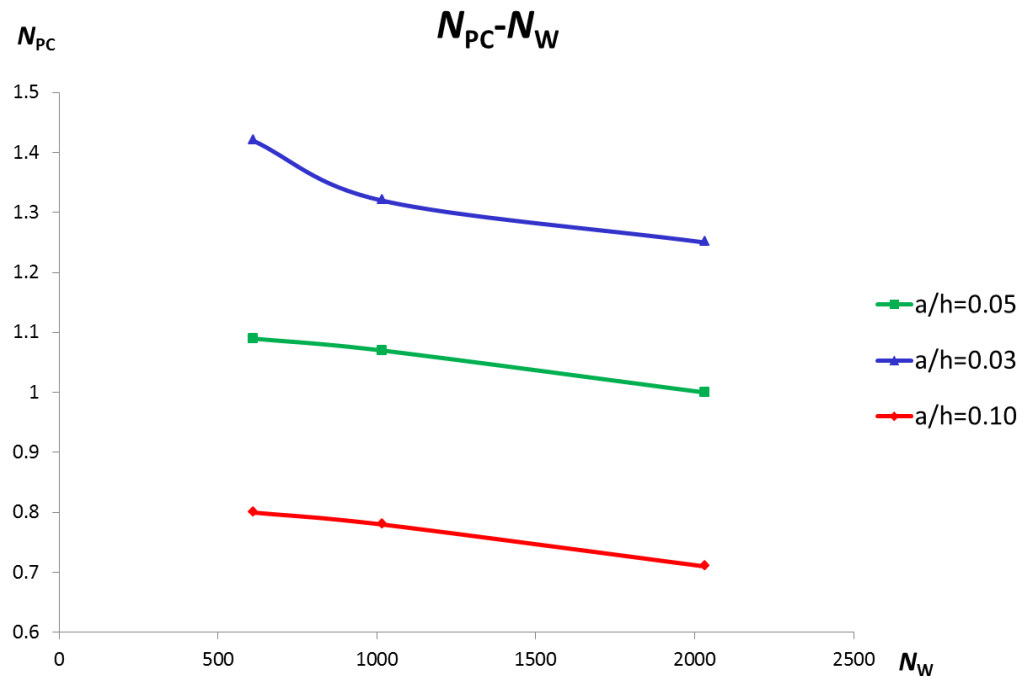
Figure 5.12 Influence of N_{W} **on the Ductile-to-Brittle transition (** N_{PC} **).**
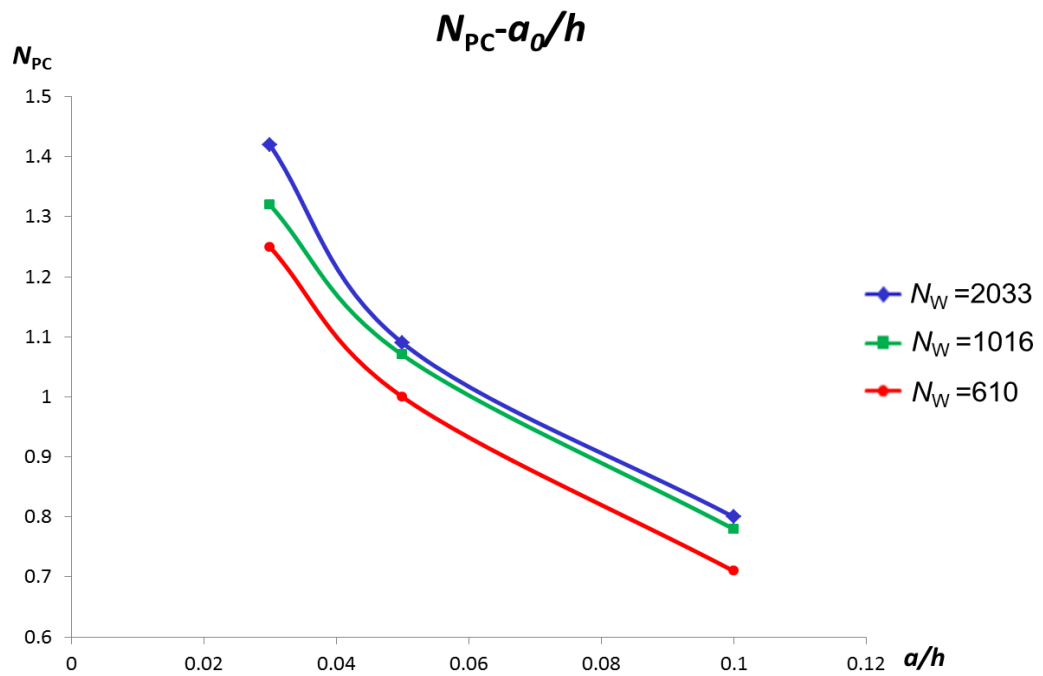
Figure 5.13 Notch-sensitivity of N_{PC} **.**

55

The Figures 5.12 and 5.13 summarize the results: by increasing the N_W value, the fiber volume ratio required to define the minimum reinforcement condition decreases, since the higher bridging action; moreover, these results show the notch-sensitivity. If the initial crack depth of the specimen increase, indeed, the minimum reinforcement required for the un-cracked structural element is underestimated.

- **FIBER DISTRIBUTION**

As discussed in Chapter 4, the number of fibers modelling, corresponding to a given fiber volume fraction is an input data of the MATLAB code. By the fiber amount depends the computation time, so it is relevant to understand how this parameter influenced the evaluation of the minimum reinforcement, to simplify the application of the model. Moreover, it is possible to choose the first dimensionless fiber position (ξ_{min}) and the last one (ξ_{max}). The fiber distribution has a fundamental role in the bridging action of the reinforcing phase, as seen in Chapter 3. An uniform distribution into the specimen section depends on casting technique. In the following numerical simulation of TPBT the effect of different fiber modelling on N_{PC} is evaluated, both in terms of number and positioning. Particularly, fixed an intermedium N_W value (1016), still for three different initial crack depth, the ductile to brittle transition is reproduced by varying the number of fiber (20 and 100) and the value of ξ_{max} (0.50 and 0.95). Geometrical and mechanical properties assumed for the prismatic specimen are reported in Table 5.5. The slippage constitutive law of hooked-end fiber is implemented.

Beam thickness	b	[cm]	15
Beam depth	h	[cm]	15
Beam span	S	[cm]	45
Beam length	L	[cm]	50
Young's modulus	E	[MPa]	31500
Fracture toughness	K_{IC}	[kg/cm$^{1.5}$]	70
Concrete compressive strength	f_{cm}	[MPa]	33
Fiber diameter	d_f	[cm]	0.075
Fiber length	l_f	[cm]	3.5
Fiber tensile strength	f_u	[MPa]	1100

Table 5.5 Geometrical and mechanical properties of the FRC specimen.
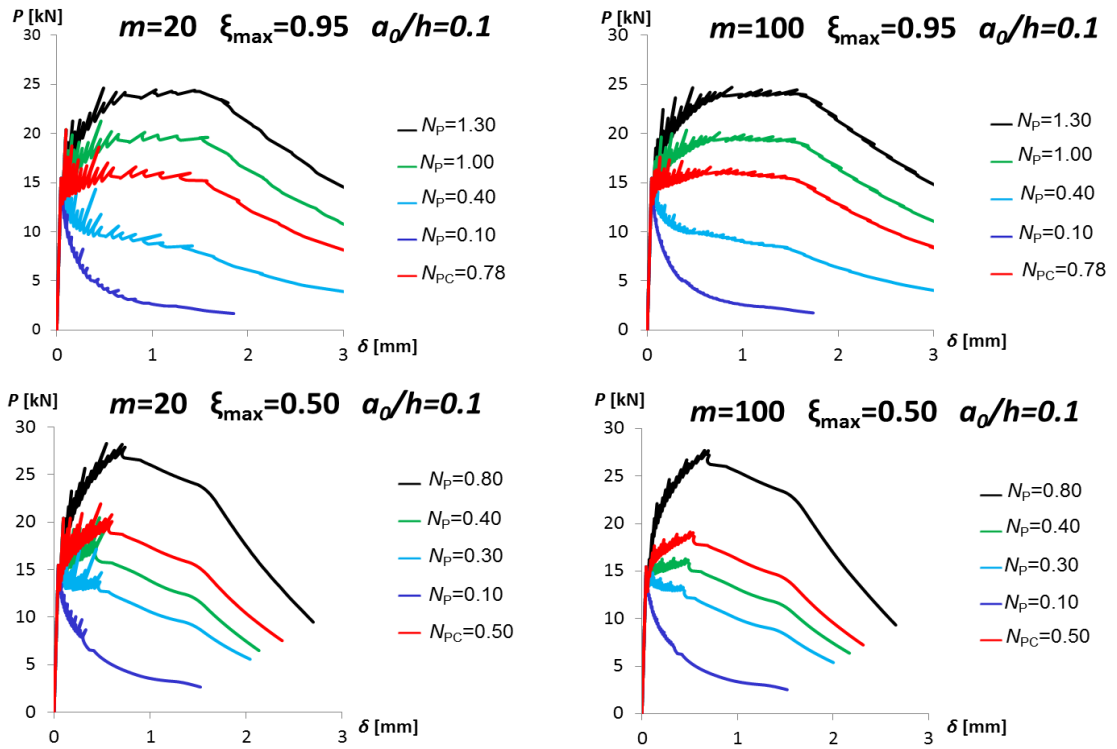
Figure 5.14 Influence of fiber modelling on N_{PC} .
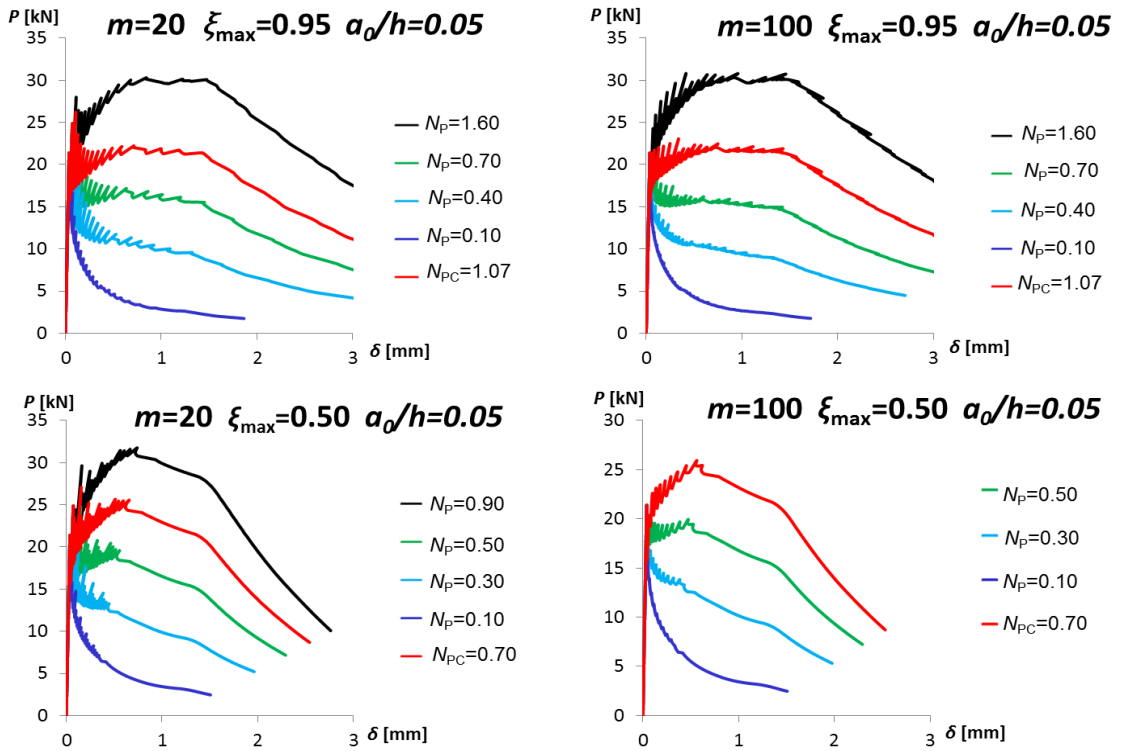
Figure 5.15 Influence of fiber modelling on N_{PC} .
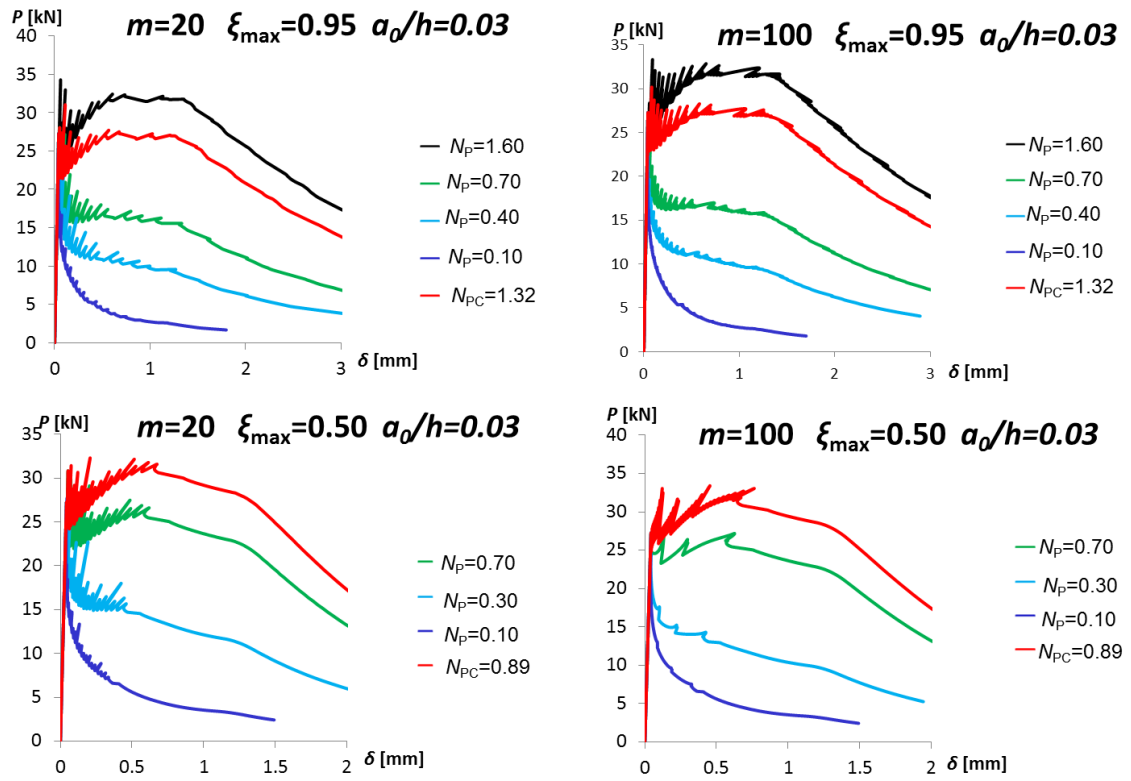
Figure 5.16 Influence of fiber modelling on N_{PC}.
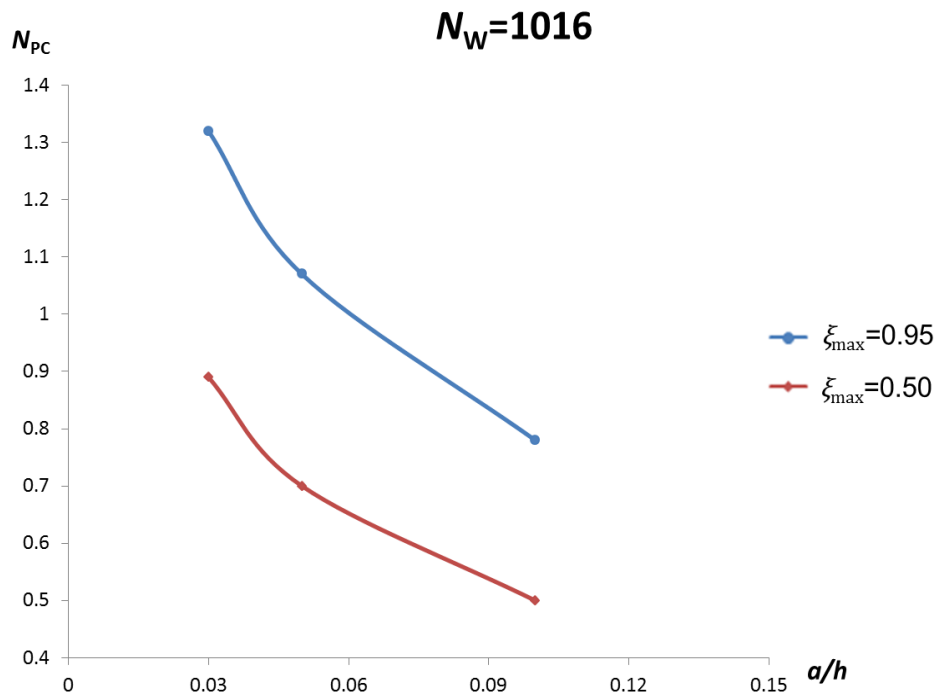
Figure 5.17 Influence of fiber modelling on N_{PC}.

For each initial crack depth, it can possible to evaluate how the number of fibers modelling leave unchanged the critical value of N_{p}. The N_{PC}, indeed, is related to the global response, and the numerical code is able to define an equivalent bridging force for the less number of fibers, in order to ensure the equivalence between the two distributions. The effect regards, instead, the local phenomenon: less fibers are more distant, so the instabilities related to the brittle crack propagation are more evident. In Figure 5.17 the notch sensitivity is confirmed, as in the previous analysis.

The effect of an extremely bad distribution of the fiber into the specimen section can be evaluated. Indeed, it is supposed that only an half of the section contains the fibers, even if uniformly distributed ($\xi_{\mathrm{max}} = 0.50$). By comparing the results with that of the correct distribution ($\xi_{\mathrm{max}} = 0.95$), it is clear that if the fibers are not correctly distributed in the specimens realizations, the amount of the minimum reinforcing results underestimated.

Chapter 6

MINIMUM REINFORCEMENT IN FRC BEAMS

6.1   Introduction

The design of FRC members requires wide experimental campaigns, both on the two individual main components and on the composite mixture. These tests are fundamental to define the mechanical properties of the constituent materials, and to provide the so-called mix design of the composite. In this context, the definition of the minimum amount of reinforcement, required to ensure a ductile post-cracking response, is an attractive parameter for the structural design of FRC members.

This argument has been extensively discussed in the past, in the case of ordinary reinforced concrete beams. In the framework of Fracture Mechanics, the Bridged Crack model is able to evaluate the minimum reinforcement condition, synthetically described by the reinforcement brittleness number, N_P (Bosco and Carpinteri, 1990). The latter, in case of yielding bridging mechanism of the steel rebars, is a function of steel yielding stress, concrete fracture toughness, steel area percentage, and beam depth, making possible the evaluation of the size effects on the phenomenon.

In this work, the discussion about the minimum reinforcement condition is extended to FRC structural elements. As discussed in the previous section, another geometrical property has to be considered in the dimensional analysis: the embedded length of the fiber, w_c. Thus, there are finally two dimensionless parameters to describe completely the flexural response: N_W and N_P. Reinforcement geometry, its resistance and finally its volume ratio can be thus defined on the basis of these dimensionless parameters, keeping also the effect of the size variation among test specimen and structural element.

In this Chapter nine experimental campaigns, conducted by other Authors, are analysed. The main features characterizing each work are the matrix concrete composition, the fiber type and the range of fiber amount considered, the presence or absence of the initial notch, and finally the test setup. For each work, these main features are described. Then, the results of recognizing of material properties are summarized. By applying the best fitting procedure on the elastic range of the experimental $P-\delta$ curve,

the actual matrix properties (Young's Modulus and fracture toughness) are recognized. The Young's Modulus, E, is related to the slope of this first stage; the fracture toughness, K_{IC}, instead, affects the cracking bending moment. By the analysis of the post-cracking stages, the maximum pull-out fiber force, P_P, and its embedded length, w_C, are estimated. Particularly, the embedded length governs mainly the softening branch, in which the slippage phenomenon is prevalent. The pull-out fiber force, instead, is estimated through the best fitting of the stage II, between the crack onset and softening range. However, also the pull-out force exhibited by the fiber is affects by its embedded length, thus the procedure of best fitting of the whole post-cracking phase allows to define correctly the two quantities. It is worth notice that the matrix properties are uniquely defined, whereas the bridging force and the embedded length are variable with the distribution; they can be actually different for each specimen. Thus, on the bases of these four estimated parameter, the dimensionless quantities N_P and N_W are computed. The same procedure is repeated for each experimental curve. Then, the experimental $P - \delta$ curves are compared with the numerical ones. In case of experimental test on un-notched specimen, it is modelled with a small initial crack. The bridged crack, indeed, requires an initiation to reproduce the crack propagation process. Finally, considering the average of the four estimated parameter, the minimum fiber volume ratio required to provide a ductile post-cracking response of the specimen is estimated. The minimum reinforcement condition is is characterized by N_{PC}. The corresponding N_W value gives information about the stability of the behaviour.

6.2 Comparison with experimental data

6.2.1 Almusallam et al. experimental work

In the experimental campaign conducted by Almusallam et al. (2016), the post-cracking behaviour and the fracture properties of Hybrid FRC (HFRC) composites were investigated. For this purpose, a total of 27 beams with different HFRC mixes were cast. The HFRC composites were produced using different volume fractions of steel, Kevlar and polypropylene fibers. To determine the fracture parameters of the HFRC composite, notched beams were tested under three point loading as recommended by RILEM TC 162-TDF. The main variables were the fiber volume content for each type of fibre.

The results of TPBT on FRC specimens with only hooked-end steel fiber are the object of the comparison with analytical response. In the following, the main variables of the experimental campaign, including the results, are summarized.

- **MATERIALS**

  ➢ **Matrix**

  The matrix mixture, including the mechanical properties, is reported in Table 6.1.

Portland cement-ASTM type I (c)	[kg/m³]	520.0
Water (w)	[l/m³]	145.0
w/c	[-]	0.28
Superplasticizer GLI 110	[l/m³]	3
Fine sand	[kg/m³]	586
Coarse aggregate (0-5 mm)	[kg/m³]	850
Coarse aggregate (6-10 mm)	[kg/m³]	315
Concrete compressive strength (f_{cm})	[MPa]	64.5

Table 6.1 Concrete composition and mechanical properties.

  ➢ **Fiber**

  Steel hooked-end Fibers (SF) were used. Their mechanical and geometrical properties, and their volume ratio for each mixture (M1 and M3), are reported in Tables 6.2 and 6.3 respectively.

			SF
Fiber diameter	d_f	[cm]	0.075
Fiber length	l_f	[cm]	6
Fiber aspect ratio	λ	[-]	80
Fiber tensile strength	f_u	[MPa]	1225

Table 6.2 Fiber mechanical and geometrical properties.

			M1	M3
Fiber volume ratio	V_f	[%]	1.2	1.4

Table 6.3 Fiber volume ratio for each mixture.

- **TEST SETUP**

The TPBT were performed after 28 days from the cast, according to RILEM TC 162-TDF, using prismatic specimens of 15X15X60 cm, with an initial notch of 2.5 cm (Figure 6.1a). The specimens were tested for Mode-I fracture under servo-controlled electrohydraulic Zwick compression testing machine. The three point bending test was conducted so that the high stress fracture process zone was confined at the notched section. The rate of increase of mid-span deflection of the specimen was kept constant at 0.25 mm/min. The mid-span vertical deflection was recorded by the vertical LVDT attached to the mid-span of beams as shown in Figure 6.1b.
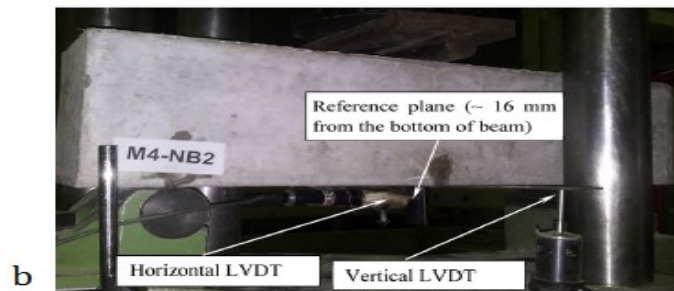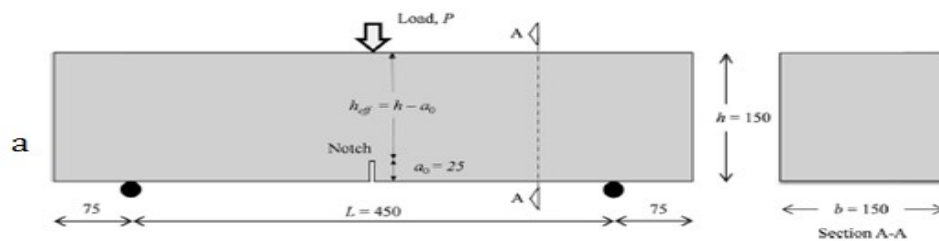
Figure 6.1 Bending Test setup on FRC specimen.

- **RESULTS AND DISCUSSION**

For each specimen, identified by beam ID, the experimental data (black curves) with the related numerical simulations (blue curves) are represented in Figure. 6.2. The best fit is obtained by varying the four parameters (K_{IC} , E , P_P , and w_C), which are summarized in Table 6.4 along with the dimensionless quantities, N_P and N_W .

It can be appreciate that in this case the matrix Young's modulus obtained is the same for the two specimen, whereas the matrix fracture toughness is different, causing doubt on the estimate of cracking bending moment. Both fiber pull-out force and its embedded length are very similar, suggesting a uniform fiber distribution among the specimen.

ID	K_{IC}	E	P_P	w_C/l_f	N_P	N_W
	[kg/cm$^{1.5}$]	[MPa]	[kN]	[-]	[-]	[-]
M1	150	38400	0.153	0.34	1.08	1348
M3	213	38400	0.159	0.36	0.91	1005

Table 6.4 Parameters obtained with best fitting procedure.
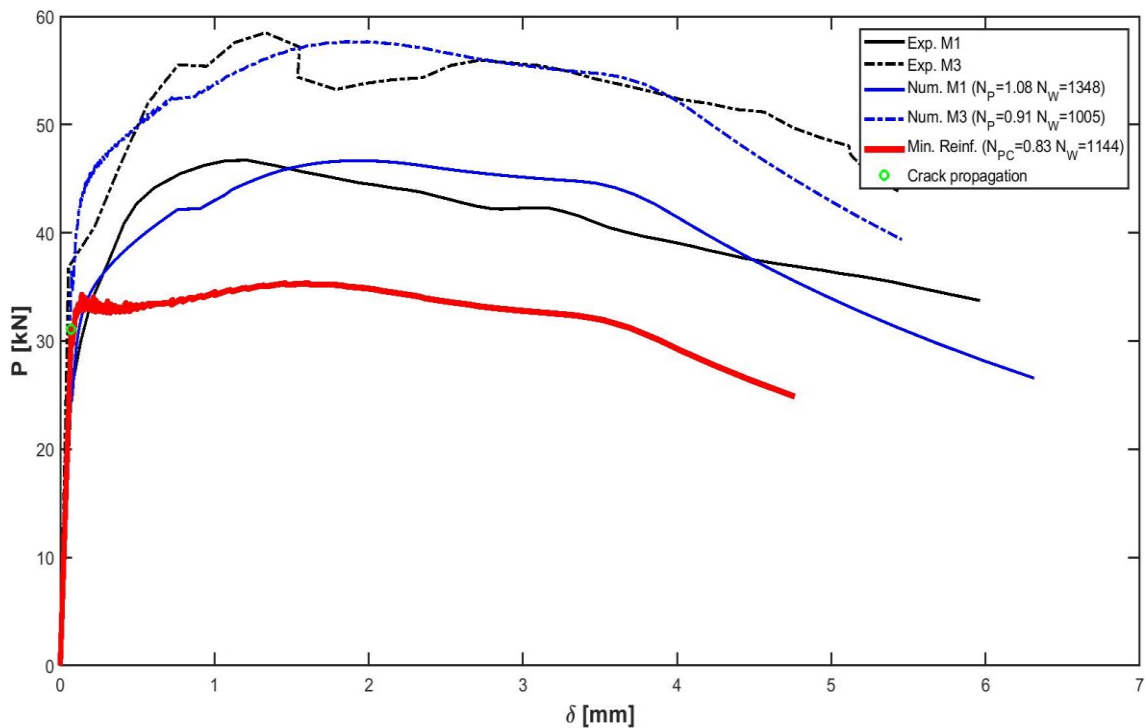
Figure 6.2 Experimental and numerical $P - \delta$ **response.**

As seen in the Figure 6.2, the model is able to reproduce the three stages of the flexural response. Particularly, blue numerical curves follow the black numerical ones in elastic phase. The two curve appear slightly different in post-cracking regimes: the analytical are more regular than the experimental ones. It is expected, regarding mainly the fiber distribution, that is actually random, as widely discussed, different from the modelled uniform one.

In Figure 6.2 is also represented, in red, the analytical curve of estimated minimum reinforcement condition. To obtain it, K_{IC}, E, P_p, and w_C are assumed as the average of the parameters in Table 6.4, the slippage constitutive law for hooked-end fibers (section 3.3) is adopted, the number of fibers modelling is the deterministic one (Eq. 2.1), fibers are uniformly distributed into the whole ligament, the other input data are defined as in following table.

Beam thickness	b	[cm]	15
Beam depth	h	[cm]	15
Notch depth	a_0	[cm]	2.5
Dimensionless notch depth	a_0/h	[-]	0.17
Beam span	S	[cm]	45
Beam length	L	[cm]	60
Young's modulus	E	[MPa]	38400
Fracture toughness	K_{IC}	[kg/cm$^{1.5}$]	182
Concrete compressive strength	f_{cm}	[MPa]	64.5
Fiber diameter	d_f	[cm]	0.075
Fiber length	l_f	[cm]	6
Fiber tensile strength	f_u	[MPa]	1225
Fiber pull-out strength	τ_u	[MPa]	2.21
Dimensionless fiber average embedded length	w_C/l_f	[-]	0.35
Fiber volume ratio	V_f	[-]	0.83

Table 6.5 Input data for minimum reinforcement condition.

6.2.2 Mobasher et al. experimental work

The experimental research program conducted by Mobasher et al. (2014) provided a variety of tests conducted on notched and un-notched FRC beams, with different fiber types (polymeric, glass and steel fiber) and dosage rate (13 kg/m^3, 26 kg/m^3, and 39 kg/m^3).

The results of FPBT on un-notched FRC specimen with hooked-end steel fiber are the object of the comparison with analytical response. In the following, the main variables of the experimental campaign, including the results, are summarized.

- **MATERIALS**
  - ➢ **Matrix**

    The matrix mixture, including the mechanical properties, is reported in Table 6.6.

Portland cement (c)	[kg/m³]	380.0
Water (w)	[kg/m³]	242.0
w/c	[-]	0.48
Fly ash	[kg/m³]	125.0
Fine aggregate	[kg/m³]	1343
Coarse aggregate	[kg/m³]	1816
Concrete compressive strength (f_{cm})	[MPa]	36

Table 6.6 Concrete composition and mechanical properties.

  - ➢ **Fiber**

    Steel Hooked-end Long fibers were used as reinforcing phase (S-HL). Their mechanical and geometrical properties, and their volume ratio for each mixture, are reported in Tables 6.7 and 6.8 respectively.

			S-HL
Fiber diameter	d_f	[cm]	0.03
Fiber length	l_f	[cm]	5
Fiber aspect ratio	λ	[-]	167
Fiber tensile strength	f_u	[MPa]	2300

Table 6.7 Fiber mechanical and geometrical properties.

			S-13-HL-28d	S-26-HL-28d	S-39-HL-28d
Fiber volume ratio	V_f	[%]	0.17	0.33	0.50

Table 6.8 Fiber volume ratio for each mixture.

- **TEST SETUP**

Un-notched SFRC prismatic specimen were tested under four-point bending loading configuration (Figure 6.3). The specimen dimensions were 15X15X51 cm, the span was equal to 45 cm. The tests were carried out after 28 days of curing. Casting of the specimens, their curing and the experimental setup were chosen in accordance with ASTM C1018-97/1997. The beams were loaded orthogonal to the casting direction. Tests were performed under closed loop control with the load point deflection as the controlled variable. The midspan deflection was measured using a Linear Variable Differential Transformer (LVDT) with a working range of 2.5 mm.
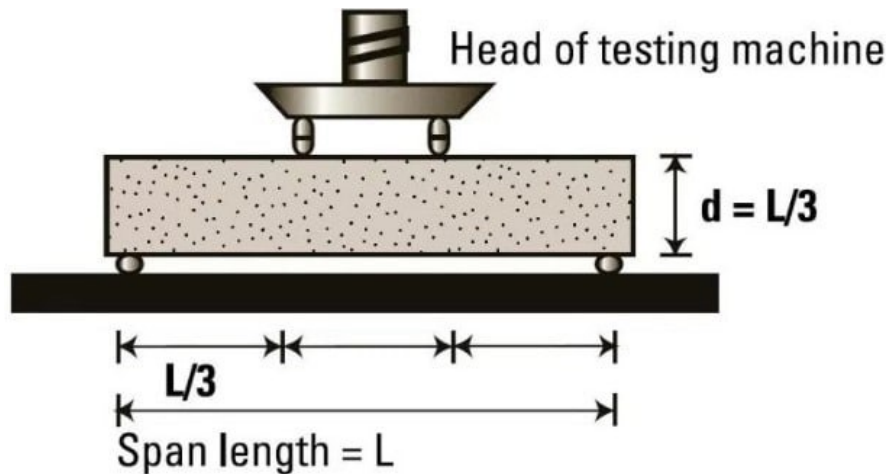
Figure 6.3 Bending Test setup on FRC specimen.

- **RESULTS AND DISCUSSION**

For each specimen, identified by beam ID, the experimental data (black curves) with the related numerical simulations (blue curves) are represented in Figure. 6.4. The best fit is obtained by varying the four parameters (K_{IC}, E, P_P, and w_c), which are summarized in Table 6.9 along with the dimensionless quantities, N_P and N_W.

The matrix toughness recognized is almost the same for two of the three specimens, but their Young's modulus shows relevant differences. As expected, also in fiber properties there are some differences.

ID	K_{IC}	E	P_P	w_C/l_f	N_P	N_W
	[kg/cm$^{1.5}$]	[MPa]	[kN]	[-]	[-]	[-]
S-13-HL-28d	45	22000	0.010	0.50	0.20	3156
S-26-HL-28d	55	25000	0.015	0.38	0.49	2230
S-39-HL-28d	56	15000	0.017	0.35	0.83	1210

Table 6.9 Parameters obtained with best fitting procedure.
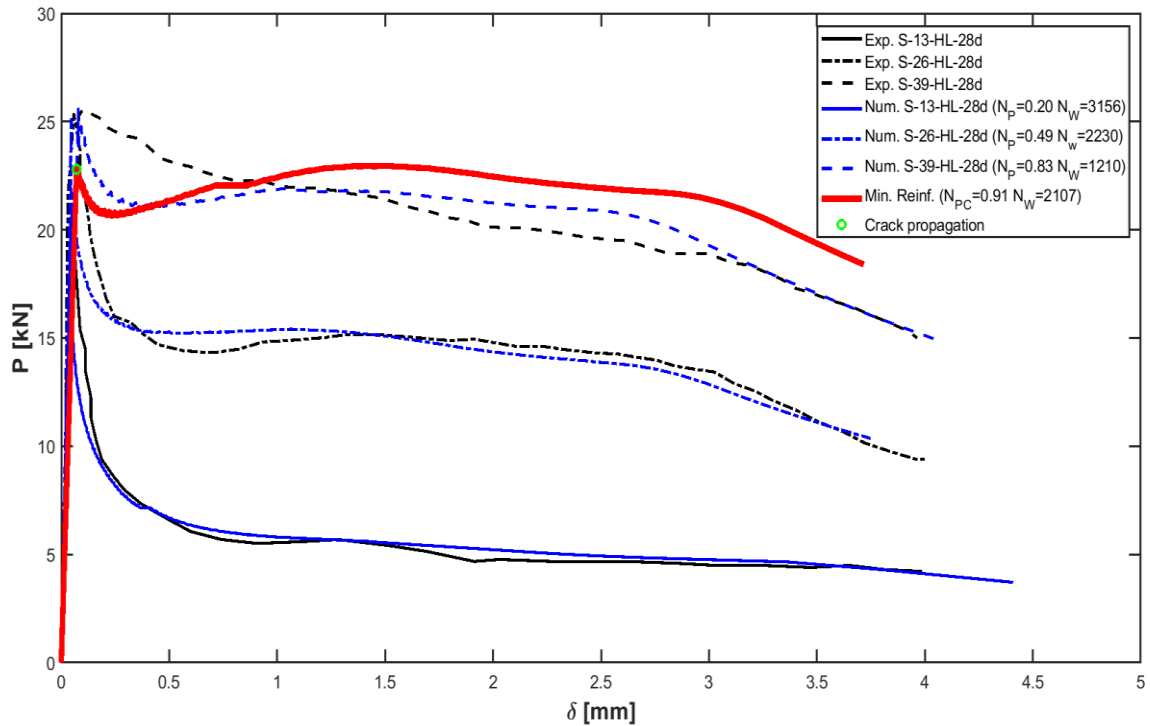
Figure 6.4 Experimental and numerical $P - \delta$ response.

Looking at the Figure 6.4, it is possible to appreciate the capability of the Bridged Crack model to reproduce analytically the flexural response of FRC. Especially in this case, it is surprising how the numerical curves exactly follow the experimental ones, in all the three stage of the response. The N_{PC} value is equal to 0.91. For all the experimental curves is $N_P < N_{PC}$ (in post-cracking stage the bending moment decreases). However, it is possible to appreciate that the lowest N_W value, corresponding to the highest fiber content, describes the curve most affect by the softening final branch. In this case, being the test specimen un-notched, a fictitious initial crack depth, set equal to 0.05 h, is used.

In Figure 6.4 is also represented, in red, the analytical curve of estimated minimum reinforcement condition. . To obtain it, K_{IC}, E, P_P, and w_C are assumed as the average of the parameters in Table 6.4, the slippage constitutive law for hooked-end fibers (section

3.3) is adopted, the number of fibers modelling is the deterministic one (Eq. 2.1), fiber is uniformly distributed into the whole ligament, the other input data are defined as in Table 6.10.

Beam thickness	b	[cm]	15
Beam depth	h	[cm]	15
Notch depth	a_0	[cm]	0.75
Dimensionless notch depth	a_0/h	[-]	0.05
Beam span	S	[cm]	45
Beam length	L	[cm]	51
Young's modulus	E	[MPa]	20700
Fracture toughness	K_{IC}	[kg/cm$^{1.5}$]	52
Concrete compressive strength	f_{cm}	[MPa]	36
Fiber diameter	d_f	[cm]	0.03
Fiber length	l_f	[cm]	5
Fiber tensile strength	f_u	[MPa]	2300
Fiber pull-out strength	τ_u	[MPa]	0.59
Dimensionless fiber average embedded length	w_C/l_f	[-]	0.41
Fiber volume ratio	V_f	[-]	0.62

Table 6.10 Input data for minimum reinforcement condition.

6.2.3 Soetens et al. experimental work

This experimental campaign was conducted by Soetens and Matthis (2014). Through residual flexural parameters obtained by means of three- or four-point bending tests, a performance classification of the SFRC was done and a Mode I crack opening constitutive law for SFRC was derived for structural design purposes. For this purpose, a total of 42 bending tests have been conducted. Test parameters included fiber dosage (20 kg/m^3 and $40\,kg/m^3$), fibre type (long bare steel fiber with normal strength and zinc-coated fiber with high strength) and concrete type (normal and high strength).

The results of FPBT on SFRC specimens with normal strength steel fiber and normal strength matrix are the object of the comparison with analytical response. In the following, the main variables of the experimental campaign, including the results, are summarized.

- **MATERIALS**

  ➢ **Matrix**

  The components and mechanical properties of the concrete matrix are reported in Table 6.11.

Cement CEM I 52,5 N (c)	[kg/m³]	390.0
Water (w)	[kg/m³]	188.0
w/c	[-]	0.48
Superplasticizer glenium 51	[kg/m³]	2.20
Sand (0-4 mm)	[kg/m³]	805
Crushed aggregate (2-7 mm)	[kg/m³]	150
Crushed aggregate (7-14 mm)	[kg/m³]	850
Concrete compressive strength (f_{cm})	[MPa]	57.4

Table 6.11 Concrete composition and mechanical properties.

  ➢ **Fiber**

  Long steel hooked-end with Normal strength fibers were used (LN). Their mechanical and geometrical properties, and their volume ratio for each mixture, are reported in Tables 6.12 and 6.13 respectively.

			LN
Fiber diameter	d_f	[cm]	0.075
Fiber length	l_f	[cm]	6
Fiber aspect ratio	λ	[-]	80
Fiber tensile strength	f_u	[MPa]	1236

Table 6.12 Fiber mechanical and geometrical properties.

			4P-LN-20	4P-LN-40
Fiber volume ratio	V_f	[%]	0.25	0.51

Table 6.13 Fiber volume ratio for each mixture.

- **TEST SETUP**

Four-point bending tests based on NBN (1992) were conducted (Figure 6.5) on un-notched prismatic specimen of 15X15X60 cm. The span length is equal to 45 cm and the distance between the position of the loads is at 1/3th of the span length. The deflection was measured by means of a linear variable displacement transducer (LVDT), attached to a brace which is fixed to the beam by a hinge at one support and is free to slide at the other support. Testing is performed displacement-controlled at a deflection rate of 0.05 mm/min until reaching a midspan deflection of at least 4 mm.
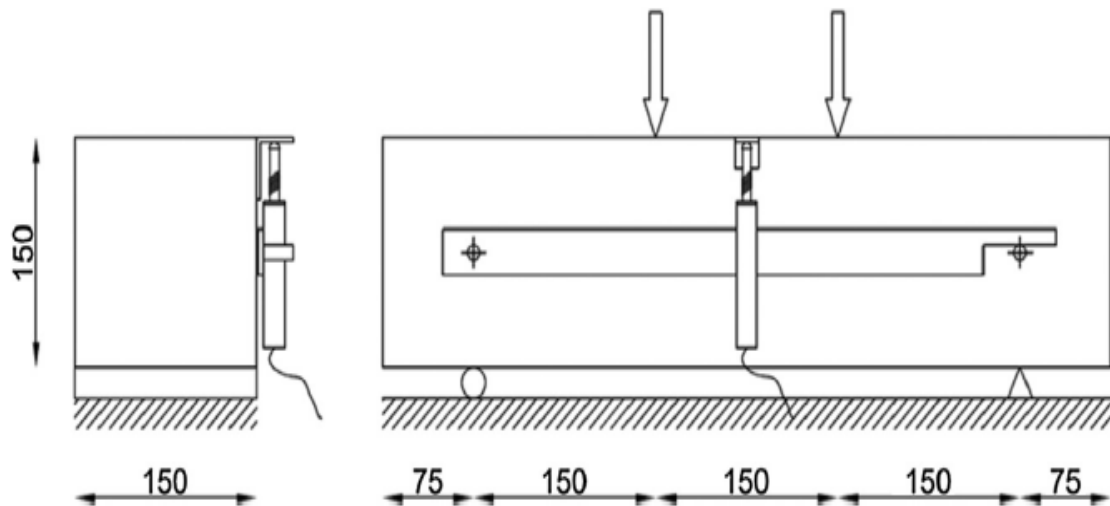
Figure 6.5 Bending Test setup on FRC specimen.

- **RESULTS AND DISCUSSION**

For each specimen, identified by beam ID, the experimental data (black curves) with the related numerical simulations (blue curves) are represented in Figure. 6.6. The best fit is obtained by varying the four parameters (K_{IC}, E, P_P, and w_C), which are summarized in Table 6.14 along with the dimensionless quantities, N_P and N_W.

For this mixture, the estimate of the matrix fracture toughness is particularly different between the two specimen. The un-notched specimen could be the cause of this inhomogeneity in the response.

ID	K_{IC}	E	P_P	w_C/l_f	N_P	N_W
	[kg/cm$^{1.5}$]	[MPa]	[kN]	[-]	[-]	[-]
4P-LN-20	58	30000	0.209	0.26	0.79	2083
4P-LN-40	80	33000	0.193	0.42	1.08	2684

Table 6.14 Parameters obtained with best fitting procedure.
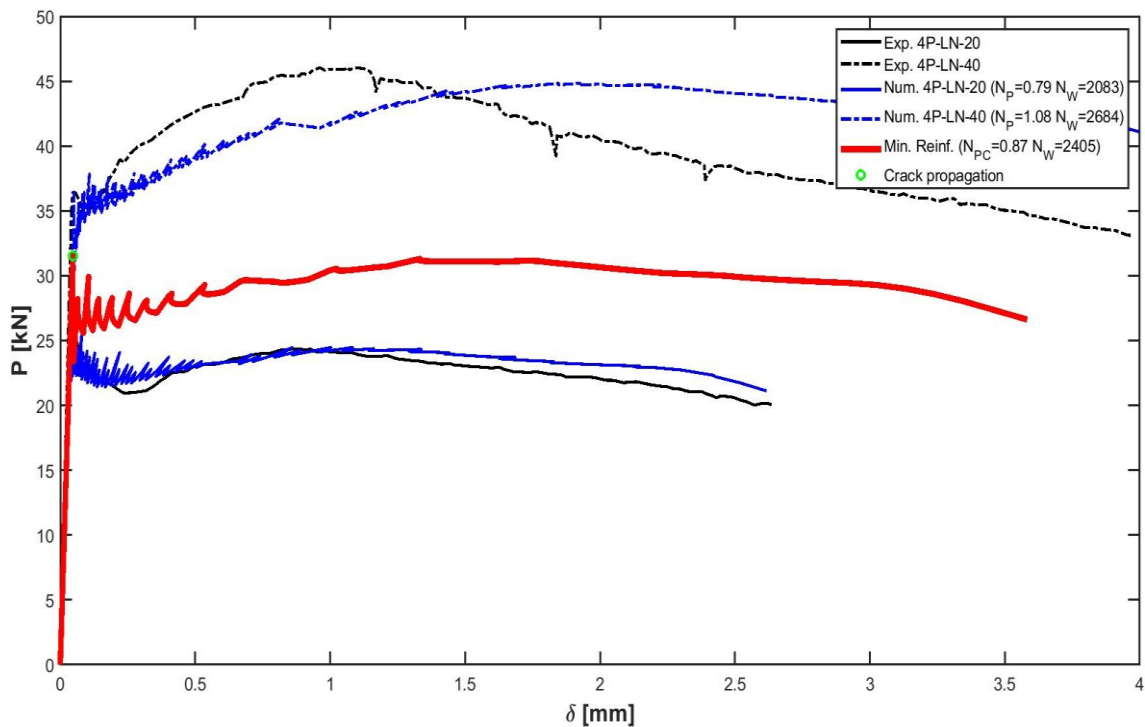
Figure 6.6 Experimental and numerical $P - \delta$ response.

The N_{PC} value is equal to 0.87; the lowest fiber volume ratio is not enough to provide a ductile post-cracking behaviour of the specimen, whereas the highest one allows a strain

hardening (II stage). Regarding the mixture 4P-LN-40, the blue numerical curve and the black experimental one are slightly different. It is mainly the effect of the two assumptions related to the fiber distribution (discussed in section 2.1) and the constitutive slippage law (discussed in section 3.3).

In Figure 6.6 is also represented, in red, the analytical curve of estimated minimum reinforcement condition. To obtain it, K_{IC}, E, P_{P}, and w_C are assumed as the average of the parameters in Table 6.4, the slippage constitutive law for hooked-end fibers (section 3.3) is adopted, the number of fibers modelling is the deterministic one (Eq. 2.1), fiber is uniformly distributed into the whole ligament, the other input data are defined as in Table 6.15.

Beam thickness	b	[cm]	15
Beam depth	h	[cm]	15
Notch depth	a_0	[cm]	0.75
Dimensionless notch depth	a_0/h	[-]	0.05
Beam span	S	[cm]	45
Beam length	L	[cm]	60
Young's modulus	E	[MPa]	31500
Fracture toughness	K_{IC}	[kg/cm$^{1.5}$]	69
Concrete compressive strength	f_{cm}	[MPa]	57.4
Fiber diameter	d_{f}	[cm]	0.075
Fiber length	l_{f}	[cm]	6
Fiber tensile strength	f_{u}	[MPa]	1236
Fiber pull-out strength	τ_u	[MPa]	2.84
Dimensionless fiber average embedded length	w_C/l_{f}	[-]	0.34
Fiber volume ratio	V_{f}	[-]	0.34

Table 6.15 Input data for minimum reinforcement condition.

6.2.4   Alberti et al. experimental work

The experimental campaign conducted by Alberti et al. (2014), aims to study the synergies between the steel fibers and the new structural synthetic fibers added to Self-Compacting Concrete (SCC). Following this purpose, manufacture of a SCC with polyolefin and steel fibers was attempted. This entailed two hybrid fiber-reinforced concretes being manufactured, which were characterized and their properties compared with those of the SCC reinforced only with one type of fiber.

Three Point Bending Test on SFRC specimen were carried out to understand the effect of only steel fiber reinforcing, with two different volume ratio (0.33% and 0.49%). The results of these FPBT are the object of the comparison with analytical response. In the following, the main variables of the experimental campaign, including the results, are summarized.

- **MATERIALS**

  ➢ **Matrix**

    The matrix was a Self-Compacting Concrete, its components and mechanical properties are reported in Table 6.16.

Cement CEM I 53,5 R (c)	[kg/m³]	375.0
Water (w)	[kg/m³]	187.5
w/c	[-]	0.50
Limestone powder	[kg/m³]	200.0
Sand (0-8 mm)	[kg/m³]	918
Grit (2-16 mm)	[kg/m³]	245
Gravel (4-32 mm)	[kg/m³]	367
Young's modulus (E)	[MPa]	35800
Concrete compressive strength (f_{cm})	[MPa]	47

Table 6.16 Concrete composition and mechanical properties

  ➢ **Fiber**

    Hooked end Steel fibers were considered (S). Their mechanical and geometrical properties, and their volume ratio for each mixture, are reported in Tables 6.17 and 6.18 respectively.

			S
Fiber diameter	d_f	[cm]	0.055
Fiber length	l_f	[cm]	3.5
Fiber aspect ratio	λ	[-]	64
Fiber tensile strength	f_u	[MPa]	1100

Table 6.17 Fiber mechanical and geometrical properties.

			S33	S49
Fiber volume ratio	V_f	[%]	0.33	0.49

Table 6.18 Fiber volume ratio for each mixture.

- **TEST SETUP**

In accordance with RILEM, TC-187-SOC, three-point bending tests were carried out on prismatic specimens, with dimensions 10X10X43 cm, of each mixture. There is an initial crack depth of 3.33 cm. The geometry was set based on the depth (D) of the sample shown in Figure 6.7. Thus, span was chosen as three times the depth and the notch height as one third of the depth in the center of the span. The test was initially controlled by a clip-on gage crack mouth opening displacement (CMOD) device placed on the notch. Deflection was also measured by two linear variable differential transformer (LVDT) devices on each side of the specimen.
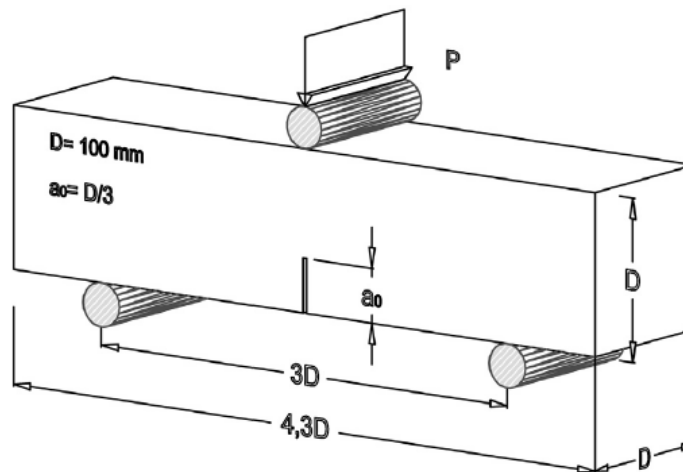
Figure 6.7 Bending Test setup on FRC specimen.

- **RESULTS**

For each specimen, identified by beam ID, the experimental data (black curves) with the related numerical simulations (blue curves) are represented in Figure. 6.8. The best fit is obtained by varying the four parameters (K_{IC} , E , P_{P} , and w_C), which are summarized in Table 6.19 along with the dimensionless quantities, N_{P} and N_{W} .

For this mixture, the estimate of the four parameters provides results homogeneous among the two specimens.

ID	K_{IC}	E	P_{P}	w_C/l_f	N_{P}	N_{W}
	[kg/cm$^{1.5}$]	[MPa]	[kN]	[-]	[-]	[-]
S33	90	25000	0.051	0.30	0.26	922
S49	97	30000	0.060	0.32	0.40	1095

Table 6.19 Parameters obtained with best fitting procedure.
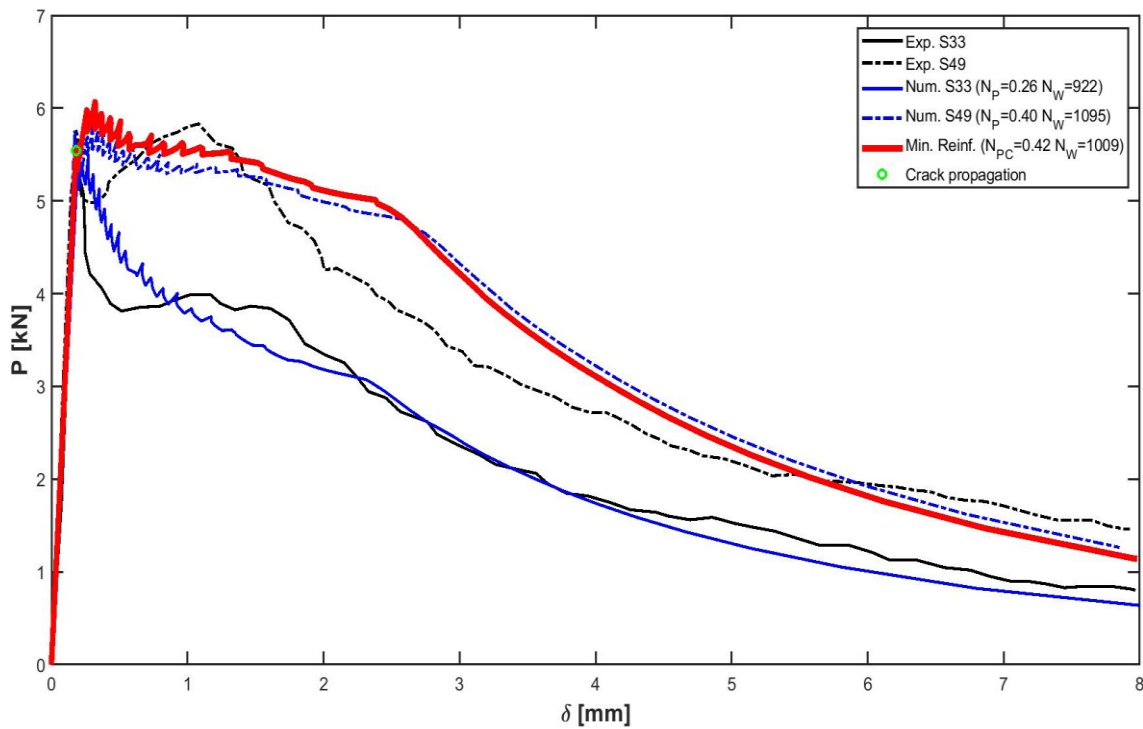
Figure 6.8 Experimental and numerical $P - \delta$ **response.**

The Figure 6.8 shows that the mixture used is not able to provide a stable post-cracking behaviour. However, these tests are carried out within a research program about HFRC, so this steel fiber type are then mixed with other fiber type to enhance the mixture

performance. It is worth notice, especially in this case, that the N_W low values, ranging from 922 to 1095, predict correctly the un-stable response of the specimens.

In Figure 6.8 is also represented, in red, the analytical curve of estimated minimum reinforcement condition. . To obtain it, K_{IC}, E, P_P, and w_C are assumed as the average of the parameters in Table 6.4, the slippage constitutive law for hooked-end fibers (section 3.3) is adopted, the number of fibers modelling is the deterministic one (Eq. 2.1), fiber is uniformly distributed into the whole ligament, the other input data are defined as in Table 6.20.

Beam thickness	b	[cm]	10
Beam depth	h	[cm]	10
Notch depth	a_0	[cm]	3.33
Dimensionless notch depth	a_0/h	[-]	0.333
Beam span	S	[cm]	30
Beam length	L	[cm]	43
Young's modulus	E	[MPa]	27500
Fracture toughness	K_{IC}	[kg/cm$^{1.5}$]	93.5
Concrete compressive strength	f_{cm}	[MPa]	47
Fiber diameter	d_f	[cm]	0.055
Fiber length	l_f	[cm]	3.5
Fiber tensile strength	f_u	[MPa]	1100
Fiber pull-out strength	τ_u	[MPa]	1.83
Dimensionless fiber average embedded length	w_C/l_f	[-]	0.31
Fiber volume ratio	V_f	[-]	0.53

Table 6.20 Input data for minimum reinforcement condition.

.

6.2.5   Aydin experimental work

The present experimental research was conducted by Aydin (2013). The effects of steel fiber strength on the mechanical properties of steel fiber reinforced concretes, such as compressive strength, modulus of elasticity, splitting tensile strength, flexural strength, and fracture energy have been investigated. Steel fibers with two different tensile strength of 1100 and 2000 MPa, and two different volume fractions of 20 and 60 kg/m^3 were used in the production of normal and high strength concretes.

The results of three point bending tests on High and Normal Strength Concrete (HSC and NSC) reinforced with High and Normal Strength Fibers (HSF and NSF) are the object of the comparison with analytical response. In the following, the main variables of the experimental campaign, including the results, are summarized.

- **MATERIALS**

  ➢ **Matrix**

    The concrete matrix components and mechanical properties are reported in Table 6.16, both for NSC and HSC.

		NSC	HSC
Portland Cement CEM I 42.5 R (c)	[kg/m³]	300.0	470.0
Water (w)	[kg/m³]	180.0	180.0
w/c	[-]	0.60	0.38
Silica fume	[kg/m³]	-	55
Superplasticizer	[kg/m³]	-	3.8
Natural sand (0-5 mm)	[kg/m³]	480	396
Crushed limestone (0-3 mm)	[kg/m³]	545	450
Crushed limestone (5-15 mm)	[kg/m³]	850	850
Concrete compressive strength (f_{cm})	[MPa]	35.5	81.2
Young's Modulus (E)	[MPa]	26200	41600

Table 6.21 Concrete composition and mechanical properties.

> **Fiber**

Two different cold drawn hooked-end steel fibers with low and high carbon contents were used. Their mechanical and geometrical properties, and their volume ratio for each mixture, are reported in Tables 6.22 and 6.23 respectively.

			NSF	HSF
Fiber diameter	d_f	[cm]	0.055	0.055
Fiber length	l_f	[cm]	3	3
Fiber aspect ratio	λ	[-]	55	55
Fiber tensile strength	f_u	[MPa]	1100	2000

Table 6.22 Fiber mechanical and geometrical properties.

			NSC-NSF-20	NSC-NSF-60	NSC-HSF-20	NSC-HSF-60	HSC-NSF-20	HSC-NSF-60
Fiber volume ratio	V_f	[%]	0.26	0.77	0.26	0.77	0.26	0.77

Table 6.23 Fiber volume ratio for each mixture.

- **TEST SETUP**

Flexural tests were performed on notched prismatic specimens (10X10X60 cm) using a closed loop deflection-controlled testing machine according to RILEM 50-FMC. All of the beam specimens have the same notch depth, equal to one-third of the beam height (Figure 6.9). SFRCs were tested at a loading rate of 0.2mm/min. The specimens were loaded at their mid-span and the clear distance between the simple supports was 50 cm.
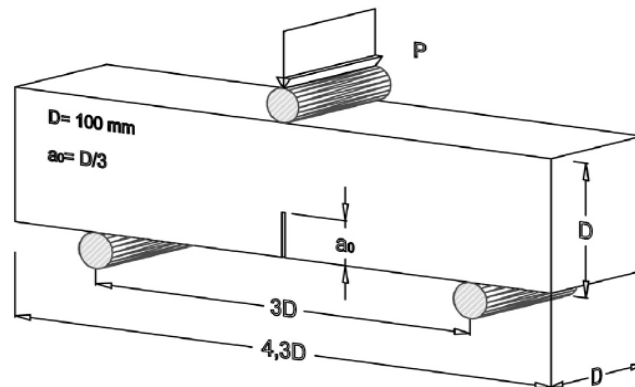
Figure 6.9 Bending Test setup on FRC specimen.

- **RESULTS AND DISCUSSION**

For each specimen, identified by beam ID, the experimental data (black curves) with the related numerical simulations (blue curves) are represented in Figures 6.10, 6.11, and 6.12 (for each mixture). The best fit is obtained by varying the four parameters (K_{IC}, E, P_{P}, and w_C), which are summarized in Tables 6.24, 6.26, and 6.28 along with the dimensionless quantities, N_{P} and N_{W}.

The NSC properties are correctly recognized, homogeneous between the two specimen considered. As it is expected, the fiber properties, which depend on the actual distribution show some differences.

ID	K_{IC}	E	P_{P}	w_C/l_{f}	N_{P}	N_{W}
	[kg/cm$^{1.5}$]	[MPa]	[kN]	[-]	[-]	[-]
NSC-NSF-20	65	30000	0.043	0.50	0.23	2189
NSC-NSF-60	66	30000	0.032	0.50	0.49	3450

Table 6.24 Parameters obtained with best fitting procedure.
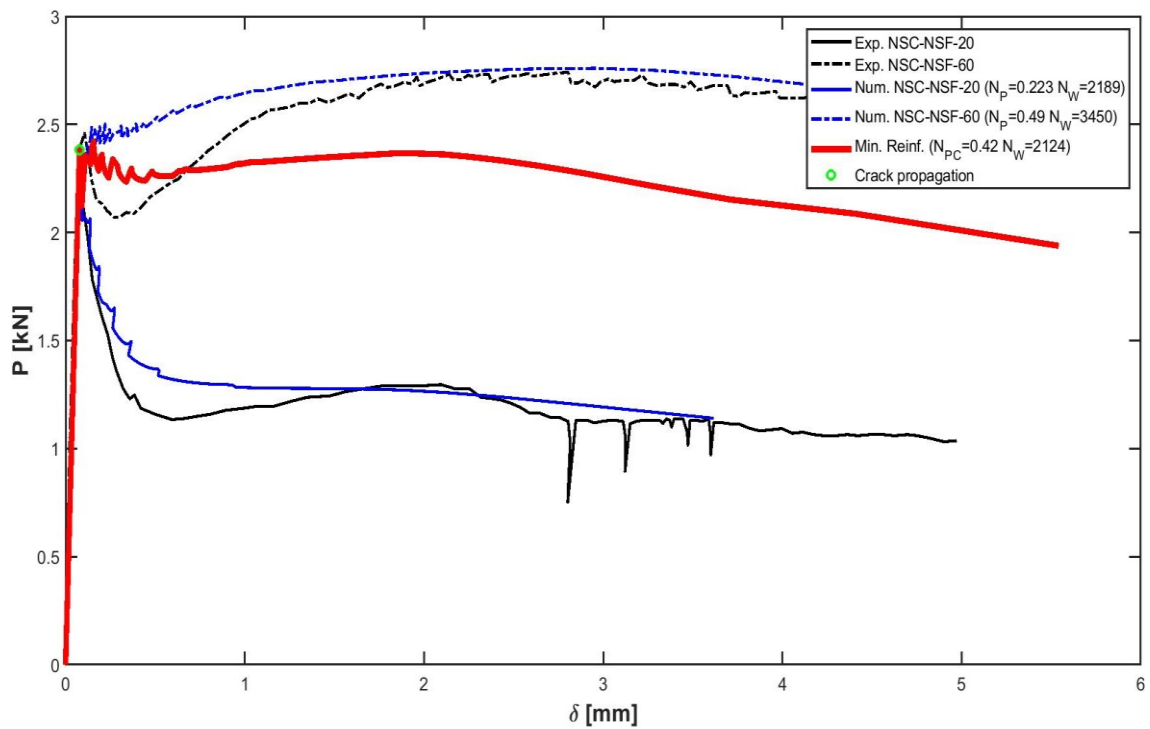
Figure 6.10 Experimental and numerical $P - \delta$ response.

The analytical curves follow the numerical ones in the three regimes of the post-cracking response. The mixture NSC-NSF (with appropriate fiber content) is able to

provide a stable post-cracking response. It is confirmed by the high N_W value corresponding to the specimen with $N_P > N_{PC}$ ($N_W = 3450$).

In Figure 6.10 is also represented, in red, the analytical curve of estimated minimum reinforcement condition. . To obtain it, K_{IC}, E, P_P, and w_C are assumed as the average of the parameters in Table 6.4, the slippage constitutive law for hooked-end fibers (section 3.3) is adopted, the number of fibers modelling is the deterministic one (Eq. 2.1), fiber is uniformly distributed into the whole ligament, the other input data are defined as in Table 6.25.

Beam thickness	b	[cm]	10
Beam depth	h	[cm]	10
Notch depth	a_0	[cm]	3.33
Dimensionless notch depth	a_0/h	[-]	0.33
Beam span	S	[cm]	50
Beam length	L	[cm]	60
Young's modulus	E	[MPa]	30000
Fracture toughness	K_{IC}	[kg/cm$^{1.5}$]	67
Concrete compressive strength	f_{cm}	[MPa]	35.5
Fiber diameter	d_f	[cm]	0.055
Fiber length	l_f	[cm]	3
Fiber tensile strength	f_u	[MPa]	1100
Fiber pull-out strength	τ_u	[MPa]	2.98
Dimensionless fiber average embedded length	w_C/l_f	[-]	0.50
Fiber volume ratio	V_f	[-]	0.56

Table 6.25 Input data for minimum reinforcement condition.

The same procedure is conducted for the mixture NSC-HSF. The matrix is the same of the previous one, indeed its mechanical parameters estimated are the same, except the fracture toughness estimated for the specimen more reinforced. The fiber distribution is homogeneous among the two beam, as recognizable by the same estimated embedded length. This type of fiber provides an higher pull-out force.

ID	K_{IC}	E	P_P	w_C/l_f	N_P	N_W
	[kg/cm$^{1.5}$]	[MPa]	[kN]	[-]	[-]	[-]
NSC-HSF-20	66	30000	0.049	0.50	0.26	2156
NSC-HSF-60	75	30000	0.039	0.50	0.54	1897

Table 6.26 Parameters obtained with best fitting procedure.
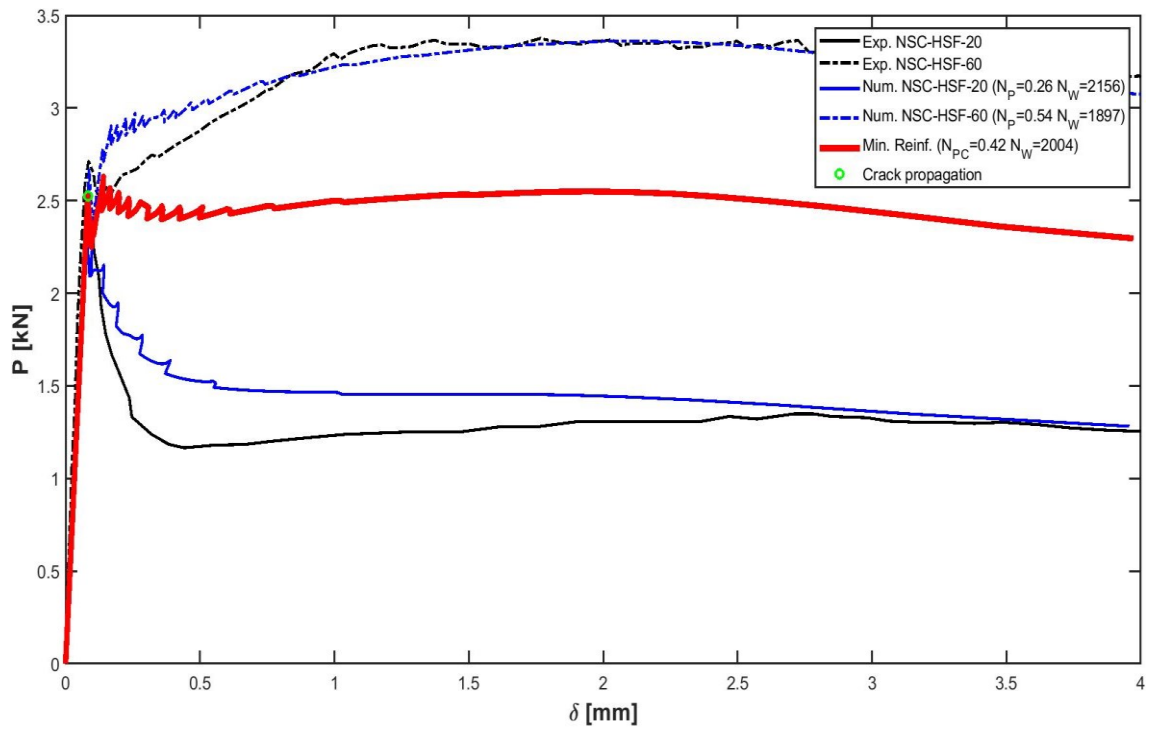
Figure 6.11 Experimental and numerical $P - \delta$ response.

Also in this case the mixture shows an high stability in post-cracking phase, when $N_P \geq N_{PC}$; particularly, for the mixture with the minimum reinforced, $N_W = 2004$. The analytical curve follow the experimental data in the three stage of the response.

In Figure 6.11 is also represented, in red, the analytical curve of estimated minimum reinforcement condition. To obtain it, the slippage constitutive law for hooked-end fibers (section 3.3) is adopted, the number of fibers modelling is the deterministic one (Eq. 2.1),

fiber is uniformly distributed into the whole ligament, the other input data are defined as in Table 6.27.

Beam thickness	b	[cm]	10
Beam depth	h	[cm]	10
Notch depth	a_0	[cm]	3.33
Dimensionless notch depth	a_0/h	[-]	0.33
Beam span	S	[cm]	50
Beam length	L	[cm]	60
Young's modulus	E	[MPa]	30000
Fracture toughness	K_{IC}	[kg/cm$^{1.5}$]	71
Concrete compressive strength	f_{cm}	[MPa]	35.5
Fiber diameter	d_f	[cm]	0.055
Fiber length	l_f	[cm]	3
Fiber tensile strength	f_u	[MPa]	2000
Fiber pull-out strength	τ_u	[MPa]	1.71
Dimensionless fiber average embedded length	w_c/l_f	[-]	0.50
Fiber volume ratio	V_f	[-]	0.51

Table 6.27 Input data for minimum reinforcement condition.

Finally, the same procedure is conducted for the mixture HSC-NSF.

An High Performance Concrete is employed, the matrix properties are thus enhanced respect to the previous mixture, as correctly estimated by best-fit procedure: both the fracture toughness and the Young's modulus are increased.

ID	K_{IC}	E	P_P	w_C/l_f	N_P	N_W
	[kg/cm$^{1.5}$]	[MPa]	[kN]	[-]	[-]	[-]
HSC-NSF-20	103	42000	0.045	0.20	0.15	774
HSC-NSF-60	107	42000	0.074	0.15	0.70	559

Table 6.28 Parameters obtained with best fitting procedure.
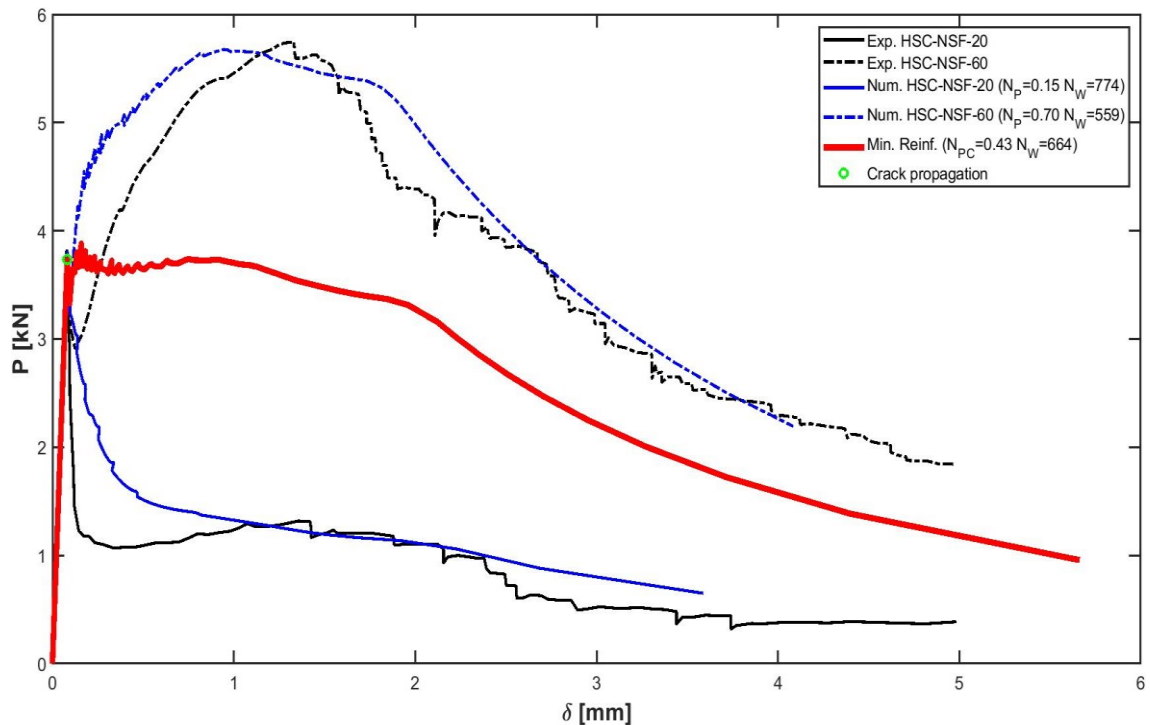
Figure 6.12 Experimental and numerical $P - \delta$ response.

In this case it can possible to compare the results of TPBT conducted, with the same test setup, on three different mixture. Looking at the Figure 6.10, 6.11, and 6.12, it is clear that a good synergy of the two main component of FRC is fundamental. Both the mixtures NSC-NSF and NSC-HSF show a stable post-cracking behaviour. If the matrix performances are enhanced (HSC) to increase the loading capacity, the post-peak behaviour begins un-stable, with N_W values extremely low (for $N_P = N_{PC}$, $N_W = 664$). In this case, even if the constitutive law modelling is still related to the slippage phenomenon, the higher

anchorage between the fiber and the high-strength matrix conducts more probably to the fiber rupture.

In Figure 6.12 is also represented, in red, the analytical curve of estimated minimum reinforcement condition. To obtain it, the slippage constitutive law for hooked-end fibers (section 3.3) is adopted, the number of fibers modelling is the deterministic one (Eq. 2.1), fiber is uniformly distributed into the whole ligament, the other input data are defined as in Table 6.29.

Beam thickness	b	[cm]	10
Beam depth	h	[cm]	10
Notch depth	a_0	[cm]	3.33
Dimensionless notch depth	a_0/h	[-]	0.33
Beam span	S	[cm]	50
Beam length	L	[cm]	60
Young's modulus	E	[MPa]	30000
Fracture toughness	K_{IC}	[kg/cm$^{1.5}$]	105
Concrete compressive strength	f_{cm}	[MPa]	81.2
Fiber diameter	d_f	[cm]	0.055
Fiber length	l_f	[cm]	3
Fiber tensile strength	f_u	[MPa]	1100
Fiber pull-out strength	τ_u	[MPa]	2.53
Dimensionless fiber average embedded length	w_C/l_f	[-]	0.18
Fiber volume ratio	V_f	[-]	0.58

Table 6.29 Input data for minimum reinforcement condition.

6.2.6 Holshemacher et al. experimental work

The experimental research program conducted by Holshemacher et al. (2010), was focused on the influence of steel fibers types and amounts on flexural response of steel bar reinforced high-strength concrete beams. In the frame of the research different bar reinforcements ($2\phi 6$ mm and $2\phi 12$ mm) and three types of fibers configurations (two hooked-end with different ultimate tensile strength, F1 and F2, and one corrugated, F3) were used. Three different fiber contents (20 kg/m^3, 40 kg/m^3 and 60 kg/m^3) were applied.

Four Point Bending Test on FRC specimen were also carried out to understand the effect of only fiber reinforcing phase. The results of FPBT on FRC specimen with fiber types F1 and F2 are the object of the comparison with analytical response. In the following, the main variables of the experimental campaign, including the results, are summarized.

- **MATERIALS**

  - **Matrix**

    The matrix was an High Strength Concrete, its components and mechanical properties are reported in Table 6.30.

Portland cement (*c*)	[kg/m³]	400.0
Water (*w*)	[kg/m³]	132.0
w/c	[-]	0.33
Fly ash	[kg/m³]	100.0
Superplasticizer	[kg/m³]	2.5
Retarder	[kg/m³]	0.2
Sand (0-2 mm)	[kg/m³]	696.7
Gravel (2-8 mm)	[kg/m³]	443.3
Gravel (8-16 mm)	[kg/m³]	638.4
Young's modulus (*E*)	[MPa]	43100
Concrete compressive strength (f_{cm})	[MPa]	94

Table 6.30 Concrete composition and mechanical properties

➢ **Fiber**

Two fiber types were considered (F1 and F2), both with hooked-end. Their mechanical and geometrical properties, and their volume ratio for each mixture, are reported in Tables 6.31 and 6.32 respectively.

			F1	F2
Fiber diameter	d_f	[cm]	0.1	0.1
Fiber length	l_f	[cm]	5	5
Fiber aspect ratio	λ	[-]	50	50
Fiber tensile strength	f_u	[MPa]	1100	1900

Table 6.31 Fiber mechanical and geometrical properties.

			F1-20	F1-40	F1-60	F2-20	F2-40	F2-60
Fiber volume ratio	V_f	[%]	0.25	0.51	0.76	0.25	0.51	0.76

Table 6.32 Fiber volume ratio for each mixture.

• **TEST SETUP**

Four Point Bending Test were conducted on un-notched prismatic specimen with dimensions 15X15X70 cm, the span was equal to 60 cm (Figure 6.13). Casting of the specimens, their curing and the experimental setup were chosen according to the German regulations, which are similar to those of RILEM TC 162-TDF. The beams were loaded orthogonal to the casting direction. The load was controlled using a displacement method with a rate of 0.2 mm/min. The deflection was recorded by two LVDTs (one on each side of the beam).
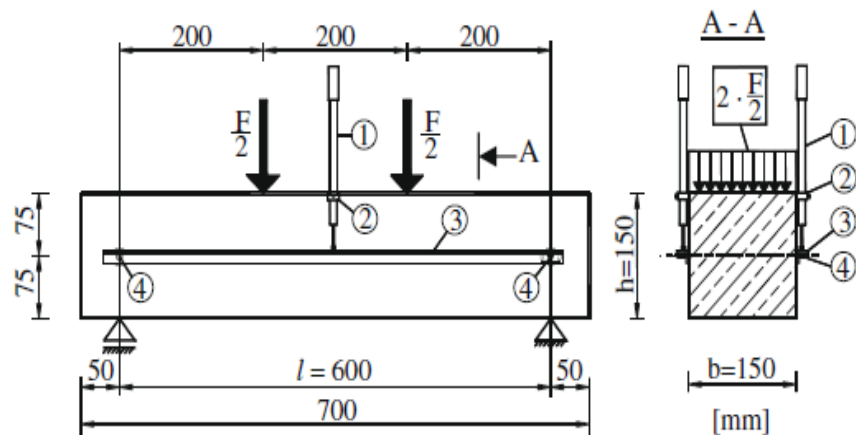

Figure 6.13 Bending Test setup on FRC specimen.

87

• **RESULTS AND DISCUSSION**

For each specimen, identified by beam ID, the experimental data (black curves) with the related numerical simulations (blue curves) are represented in Figures 6.14 and 6.15 (for each mixture). The best fit is obtained by varying the four parameters (K_{IC}, E, P_P, and w_c), which are summarized in Tables 6.33 and 6.35 along with the dimensionless quantities, N_P and N_W.

The High Strength Concrete employed in this experimental campaign show, as expected, high values of fracture toughness and Young's modulus, even if the estimates are slightly different between the three specimens. The fiber pull-out force evaluated is, instead, the same.

ID	K_{IC}	E	P_P	w_C/l_f	N_P	N_W
	[kg/cm$^{1.5}$]	[MPa]	[kN]	[-]	[-]	[-]
F1-20	119	43088	0.343	0.25	0.36	1169
F1-40	128	43088	0.343	0.16	0.68	695
F1-60	135	50000	0.343	0.12	0.95	574

Table 6.33 . Parameters obtained with best fitting procedure.
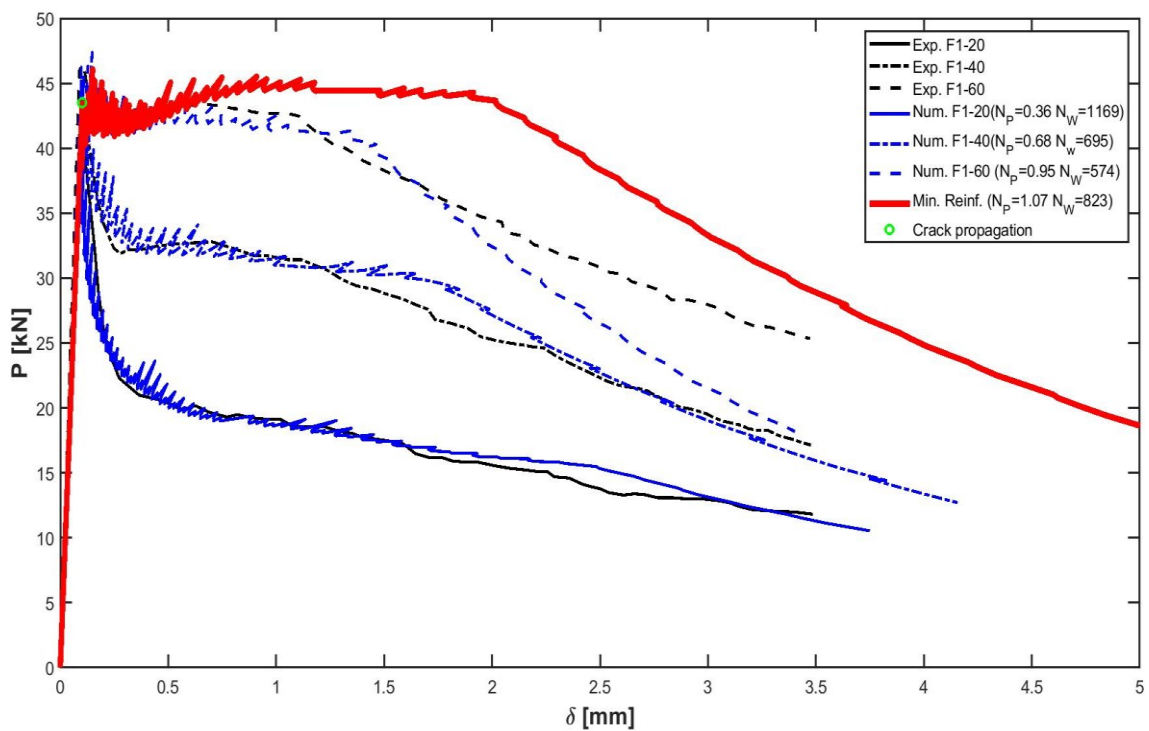

Figure 6.14 Experimental and numerical $P-\delta$ response.

The analytical curve follow the experimental ones along the three stages. This mixture do not provide a stable post-peak behaviour (for $N_P = N_{PC}$, $N_W = 823$).

In Figure 6.14 is also represented, in red, the analytical curve of estimated minimum reinforcement condition. . To obtain it, K_{IC}, E, P_P, and w_C are assumed as the average of the parameters in Table 6.4, the slippage constitutive law for hooked-end fibers (section 3.3) is adopted, the number of fibers modelling is the deterministic one (Eq. 2.1), fiber distribution is uniform into the whole ligament, the other input data are defined as in Table 6.34.

Beam thickness	b	[cm]	15
Beam depth	h	[cm]	15
Notch depth	a_0	[cm]	0.75
Dimensionless notch depth	a_0/h	[-]	0.05
Beam span	S	[cm]	60
Beam length	L	[cm]	70
Young's modulus	E	[MPa]	45000
Fracture toughness	K_{IC}	[kg/cm$^{1.5}$]	126
Concrete compressive strength	f_{cm}	[MPa]	94
Fiber diameter	d_f	[cm]	0.1
Fiber length	l_f	[cm]	5
Fiber tensile strength	f_u	[MPa]	1100
Fiber pull-out strength	τ_u	[MPa]	4.36
Dimensionless fiber average embedded length	w_C/l_f	[-]	0.18
Fiber volume ratio	V_f	[-]	0.8

Table 6.34 Input data for minimum reinforcement condition.

The same procedure is conducted for the mixture F2.

The fiber properties are enhanced, it is recognizable especially in the embedded length estimate, even if variable for inhomogeneous distribution.

ID	K_{IC}	E	P_P	w_C/l_f	N_P	N_W
	[kg/cm$^{1.5}$]	[Mpa]	[kN]	[-]	[-]	[-]
F2-20	123	50000	0.419	0.50	0.42	2624
F2-40	125	50000	0.289	0.30	0.59	1550
F2-60	128	43088	0.305	0.24	0.89	1043

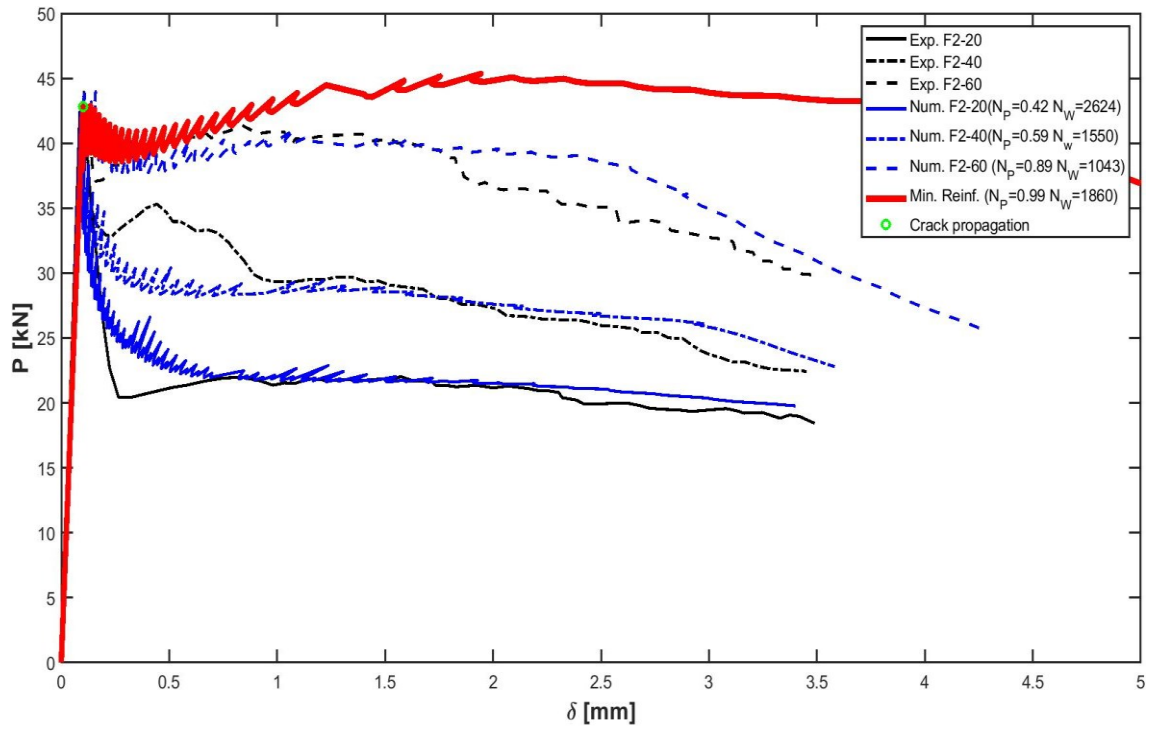**Table 6.35 Parameters obtained with best fitting procedure.**

Figure 6.15 Experimental and numerical $P - \delta$ **response.**

This campaign also confirms the effectiveness of the Bridged Crack model in the mixture design process. In this case two different types of fibers are used. Starting from a graphic analyse, and looking to the corresponding values of dimensionless parameters, it can possible to choose the best mixture. The fiber with an higher strength provides a more stable response (for $N_P = N_{PC}$, $N_W = 1860$).

In Figure 6.15 is also represented, in red, the analytical curve of estimated minimum reinforcement condition. The slippage constitutive law for hooked-end fibers (section 3.3) is adopted, the number of fibers modelling is the deterministic one (Eq. 2.1), fiber distribution is uniform into the whole ligament, the other input data are defined as in Table 6.36.

Beam thickness	b	[cm]	15
Beam depth	h	[cm]	15
Notch depth	a_0	[cm]	0.75
Dimensionless notch depth	a_0/h	[-]	0.05
Beam span	S	[cm]	60
Beam length	L	[cm]	70
Young's modulus	E	[MPa]	45000
Fracture toughness	K_{IC}	[kg/cm$^{1.5}$]	126
Concrete compressive strength	f_{cm}	[MPa]	94
Fiber diameter	d_f	[cm]	0.1
Fiber length	l_f	[cm]	5
Fiber tensile strength	f_u	[MPa]	1900
Fiber pull-out strength	τ_u	[MPa]	4.30
Dimensionless fiber average embedded length	w_C/l_f	[-]	0.4
Fiber volume ratio	V_f	[-]	0.74

Table 6.36 Input data for minimum reinforcement condition.

6.2.7   Bencardino et al. experimental work

In the experimental research program conducted by Bencardino et al. (2010), the effect of fiber type and content on the mechanical and fracture properties of FRC were assessed. For this purpose, sets of steel fiber reinforced concrete (SFRC) and polypropylene fiber reinforced concrete (PFRC) specimens were cast, both with two different fiber volume ratio (1% and 2%). Three Point Bending Test on notched specimens according to the established standard RILEM TC 162-TDF were carried out.

The results of TPBT on SFRC specimens with hooked-end steel fiber are the object of the comparison with analytical response. In the following, the main variables of the experimental campaign, including the results, are summarized.

- **MATERIALS**

  ➢ **Matrix**

  The matrix concrete components and mechanical properties are reported in Table 6.37.

Portland cement-ASTM type I (*c*)	[kg/m³]	500.0
Water (*w*)	[kg/m³]	175.0
w/c	[-]	0.35
Silica fume	[kg/m³]	25.0
Superplasticizer	[kg/m³]	7.5
Spherical quartz sand (0-2 mm)	[kg/m³]	400
Spherical quartz sand (3-6 mm)	[kg/m³]	294
Crushed coarse aggregate (0-5 mm)	[kg/m³]	522
Crushed coarse aggregate (6-10 mm)	[kg/m³]	222
Crushed coarse aggregate (11-15 mm)	[kg/m³]	240
Concrete compressive strength (f_{cm})	[MPa]	74.4

Table 6.37 Concrete composition and mechanical properties.

  ➢ **Fiber**

  Dramix Steel hooked-end fibers were used (DS). Their mechanical and geometrical properties, and their volume ratio for each mixture, are reported in Tables 6.38 and 6.39 respectively.

			DS
Fiber diameter	d_f	[cm]	0.063
Fiber length	l_f	[cm]	5
Fiber aspect ratio	λ	[-]	80
Fiber tensile strength	f_u	[MPa]	1050

Table 6.38 Fiber mechanical and geometrical properties.

			DS1%	DS2%
Fiber volume ratio	V_f	[%]	1	2

Table 6.39 Fiber volume ratio for each mixture.

- **TEST SETUP**

The TPBT were performed at 28 days, according to RILEM TC 162-TDF, using 15X15X60 cm prismatic specimens (Figure 6.16a). In the mid-span of the specimen, a single notch with a depth of 25 mm was sawn with a diamond blade to localize the crack. The tests were carried out by imposing a displacement rate of 0.05 mm/min. An INSTRON 1195 electromechanical testing machine functioning in closed loop with crosshead stroke and applied force fitted up with a 100 kN type C1 HBM load cell was used. Two HBM WA20 LVDTs were used to measure the vertical displacement under the load point on the two specimen faces. The transducers were mounted on a rigid yoke accurately set up on the specimen in order to minimize the effect of rotation during the test. Two further LVDTs WI10 were placed at the tip of the notch on the two faces of the specimen to measure the crack tip opening displacement (CTOD). The data acquisition and signal control were carried out by using a HBM Spider 8 control unit. The experimental set up is shown in Figure 6.16b.
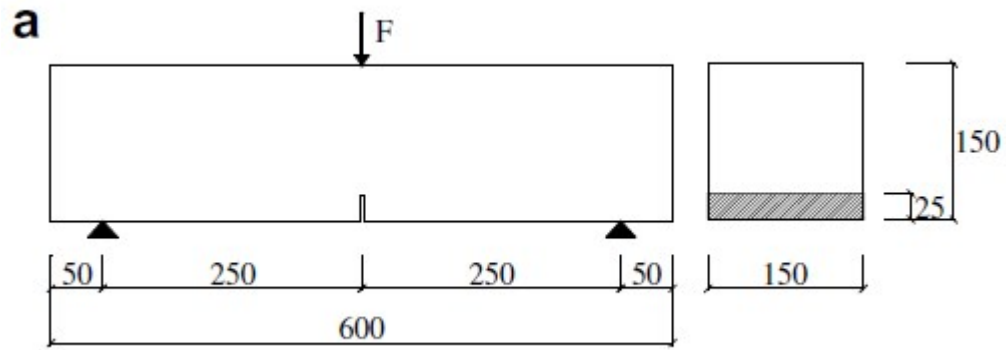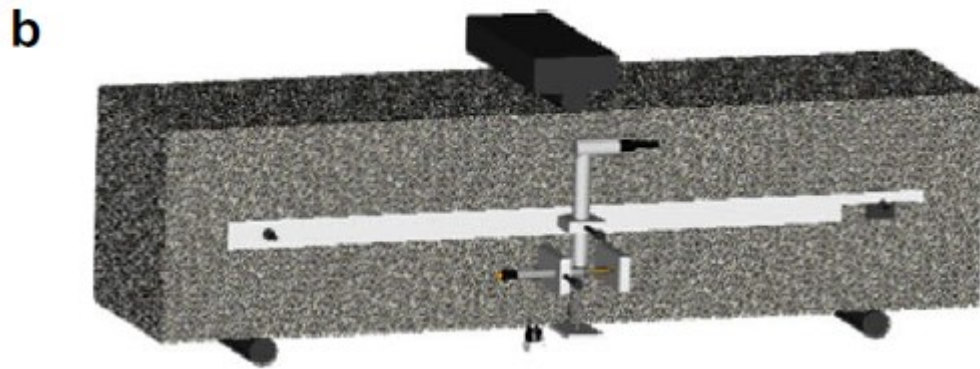
Figure 6.16 Bending Test setup on FRC specimen.

- **RESULTS AND DISCUSSION**

For each specimen, identified by beam ID, the experimental data (black curves) with the related numerical simulations (blue curves) are represented in Figure 6.17. The best fit is obtained by varying the four parameters (K_{IC}, E, P_P, and w_C), which are summarized in Table 6.40 along with the dimensionless quantities, N_P and N_W.

The matrix shows high performance, it is expected looking at the compressive strength, and it is confirmed by the mechanical properties estimated.

ID	K_{IC}	E	P_P	w_C/l_f	N_P	N_W
	[kg/cm$^{1.5}$]	[MPa]	[kN]	[-]	[-]	[-]
DS1%	140	58000	0.142	0.25	1.29	1337
DS2%	160	58000	0.083	0.32	1.31	1498

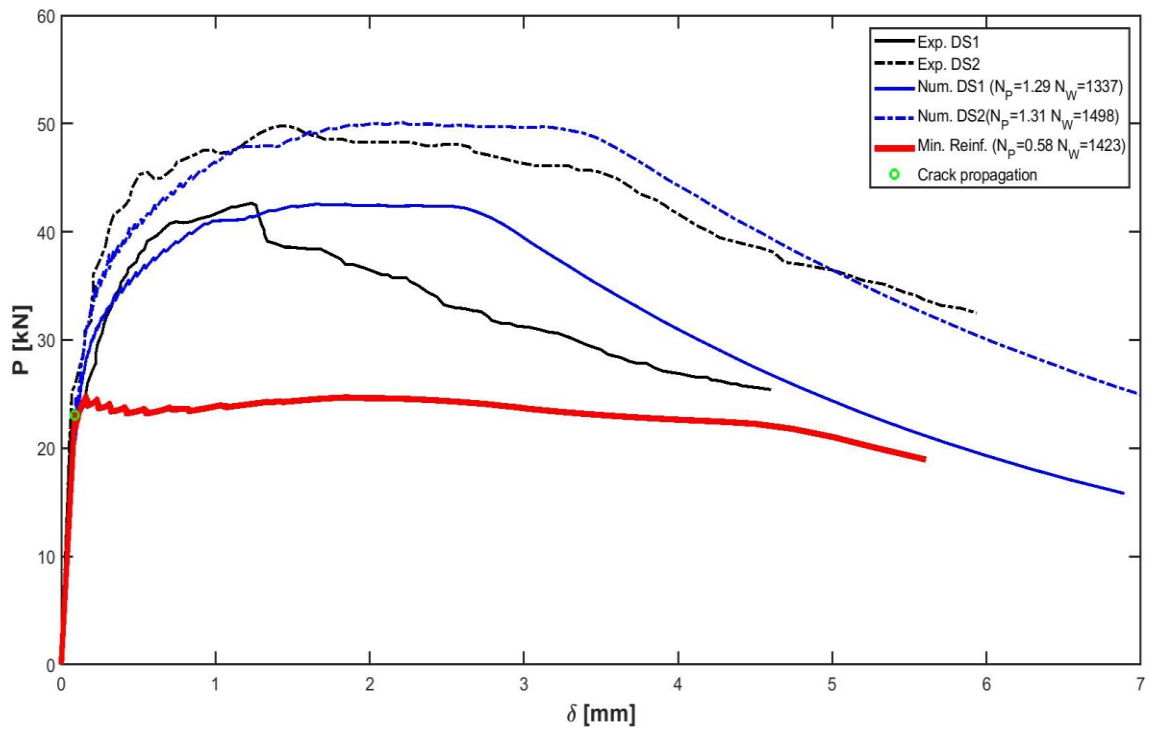**Table 6.40 Parameters obtained with best fitting procedure.**

Figure 6.17 Experimental and numerical $P - \delta$ response.

The flexural response both of the DS1 and DS2 mixtures shows a post-cracking strain hardening range ($N_{\mathrm{P}} > N_{\mathrm{PC}}$). A not uniform fiber distribution could be recognized in DS1 specimen, which provide a behaviour less stable then the DS2 one.

In Figure 6.17 is also represented, in red, the analytical curve of estimated minimum reinforcement condition. . To obtain it, K_{IC}, E, P_{P}, and w_C are assumed as the average of the parameters in Table 6.4, the slippage constitutive law for hooked-end fibers (section 3.3) is adopted, the number of fibers modelling is the deterministic one (Eq. 2.1), fiber distribution is uniform into the whole ligament, the other input data are defined as in Table 6.41.

Beam thickness	b	[cm]	15
Beam depth	h	[cm]	15
Notch depth	a_0	[cm]	2.5
Dimensionless notch depth	a_0/h	[-]	0.17
Beam span	S	[cm]	50
Beam length	L	[cm]	60
Young's modulus	E	[MPa]	58000
Fracture toughness	K_{IC}	[kg/cm$^{1.5}$]	150
Concrete compressive strength	f_{cm}	[MPa]	74.4
Fiber diameter	d_f	[cm]	0.063
Fiber length	l_f	[cm]	5
Fiber tensile strength	f_u	[MPa]	1050
Fiber pull-out strength	τ_u	[MPa]	2.3
Dimensionless fiber average embedded length	w_C/l_f	[-]	0.29
Fiber volume ratio	V_f	[-]	0.61

Table 6.41 Input data for minimum reinforcement condition.

6.2.8 Barros et al. experimental work

This experimental campaign was carried out by Barros et al. (2005). To characterize the SFRC post-cracking behaviour according to RILEM TC 162-TDF recommendations, an experimental and a numerical research were carried out in the work. Three Point Bending Tests are conducted on SFRC; the test parameters are fiber diameter and amount.

The results of TPBT on SFRC with three different dosages of Dramix hooked-end steel fibers (10 kg/m^3, 20 kg/m^3, and 30 kg/m^3) are the object of the comparison with analytical response. In the following, the main variables of the experimental campaign, including the results, are summarized.

- **MATERIALS**

  ➢ **Matrix**

  The concrete matrix components and mechanical properties are reported in Table 6.42.

Cement CEM I 42,5 R (*c*)	[kg/m³]	300.0
Water (*w*)	[kg/m³]	163.8
w/c	[-]	0.55
Superplasticizer (Rheobuild 1000)	[kg/m³]	7.5
Fine sand	[kg/m³]	173.5
Crushed sand	[kg/m³]	871
Coarse aggregate (5-15 mm)	[kg/m³]	315.7
Coarse aggregate (15-25 mm)	[kg/m³]	468.2
Concrete compressive strength (f_{cm})	[MPa]	39.7

Table 6.42 Concrete composition and mechanical properties

  ➢ **Fiber**

  Dramix hooked-end steel fibres were used: RC-80/60-BN. Their mechanical and geometrical properties, and their volume ratio for each mixture, are reported in Tables 6.43 and 6.44 respectively.

			RC-80/60-BN
Fiber diameter	d_f	[cm]	0.075
Fiber length	l_f	[cm]	6
Fiber aspect ratio	λ	[-]	80
Fiber tensile strength	f_u	[MPa]	1100

Table 6.43 Fiber mechanical and geometrical properties.

			F80/60-10	F80/60-20	F80/60-30
Fiber volume ratio	V_f	[%]	0.13	0.26	0.38

Table 6.44 Fiber volume ratio for each mixture.

- **TEST SETUP**

Figure 6.18 represents the specimen recommended by RILEM TC 162-TDF for the characterization of the flexural behaviour of SFRC (dimensions 15X15X60 cm). The measurements which were taken during testing were the load applied, mid-span displacements on both sides of the beam and the crack mouth opening displacement (CMOD).
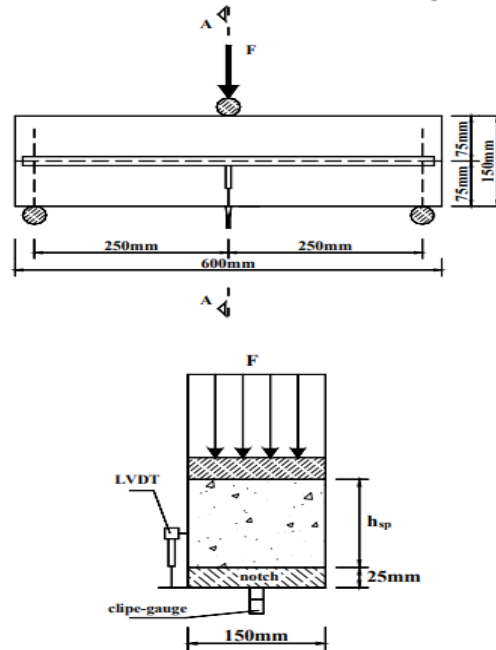

Figure 6.18 Bending Test setup on FRC specimen.

98

- **RESULTS**

For each specimen, identified by beam ID, the experimental data (black curves) with the related numerical simulations (blue curves) are represented in Figure 6.19. The best fit is obtained by varying the four parameters (K_{IC}, E, P_P, and w_C), which are summarized in Table 6.45 along with the dimensionless quantities, N_P and N_W.

In this case, even if the matrix is a normal strength concrete, the properties recognizable through the best-fit procedure, especially the Young's modulus, are really high. Also the fiber characteristics are performants, as looking at the average of the embedded length, wich is equal to $0.4\, l_f$.

ID	K_{IC}	E	P_P	w_C/l_f	N_P	N_W
	[kg/cm$^{1.5}$]	[MPa]	[kN]	[-]	[-]	[-]
F80/60-10	86	60000	0.156	0.40	0.21	4323
F80/60-20	85	50000	0.111	0.30	0.30	2733
F80/60-30	91	60000	0.116	0.50	0.43	5107

Table 6.45 Parameters obtained with best fitting procedure.
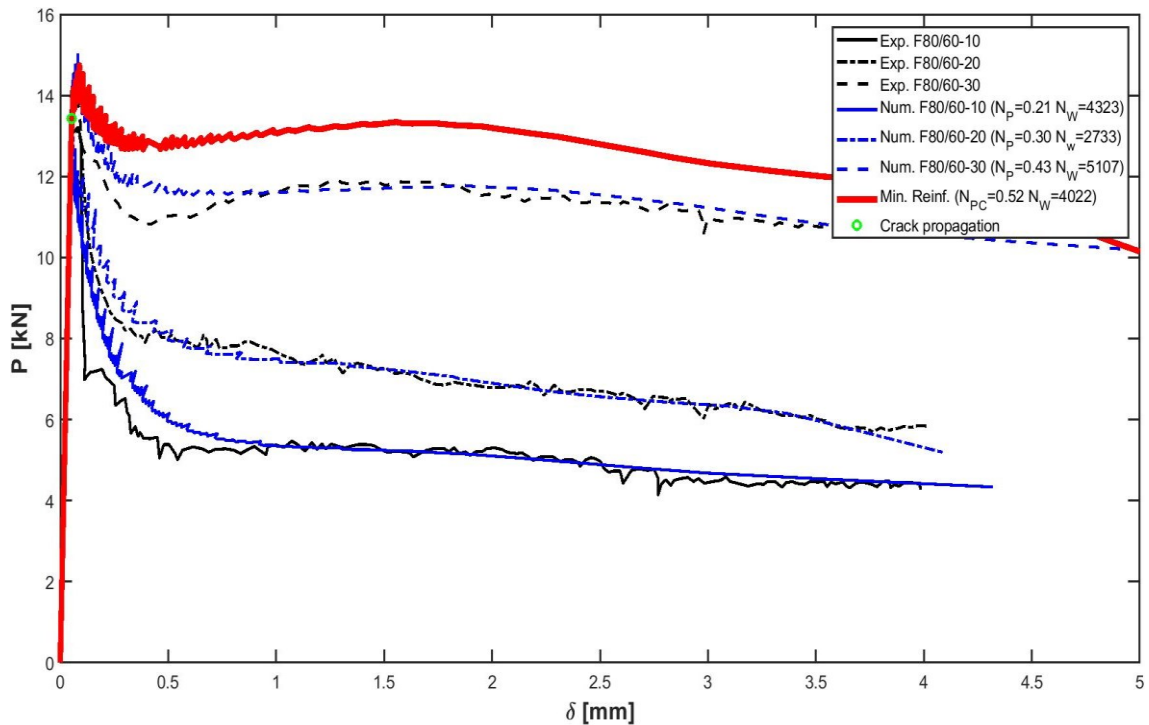

Figure 6.19 Experimental and numerical $P - \delta$ response.

In this work it is worth notice that the $P - \delta$ experimental curves, and consequentially also the numerical one, experiences a post-cracking phase without the softening branch up to a midspan deflection of 4 mm. It could be related to the fiber length (6 cm) that provide an extensive bridging action. In this case, the fiber slippage behaviour tends to be rigid-perfectly plastic (for $N_P = N_{PC}$, $N_W = 4022$).

In Figure 6.19 is also represented, in red, the analytical curve of estimated minimum reinforcement condition. . To obtain it, K_{IC}, E, P_P, and w_C are assumed as the average of the parameters in Table 6.4, the slippage constitutive law for hooked-end fibers (section 3.3) is adopted, the number of fibers modelling is the deterministic one (Eq. 2.1), fiber distribution is uniform into the whole ligament, the other input data are defined as in Table 6.46.

Beam thickness	b	[cm]	15
Beam depth	h	[cm]	15
Notch depth	a_0	[cm]	2.5
Dimensionless notch depth	a_0/h	[-]	0.17
Beam span	S	[cm]	50
Beam length	L	[cm]	60
Young's modulus	E	[MPa]	56667
Fracture toughness	K_{IC}	[kg/cm$^{1.5}$]	87
Concrete compressive strength	f_{cm}	[MPa]	25
Fiber diameter	d_f	[cm]	0.075
Fiber length	l_f	[cm]	6
Fiber tensile strength	f_u	[MPa]	1100
Fiber pull-out strength	τ_u	[MPa]	2.35
Dimensionless fiber average embedded length	w_C/l_f	[-]	0.40
Fiber volume ratio	V_f	[-]	0.40

Table 6.46 Input data for minimum reinforcement condition.

6.2.9   Barr et al. experimental work

A round robin test programme was carried out by Barr et al. (2003) on the beam-bending test recommended by the RILEM TC 162-TDF. Five testing laboratories were involved in the round robin testing programme, with Cardiff University lab as the task co-ordinator. The laboratories are: Belgian Building Research, Institute Technical University of Derunark , Katholieke Universiteit Leuven, Ruhr-University of Bochum. Plain concrete and steel fiber reinfbrced concrete (SFRC) beams were included in the test programme. The material variables for the SFRC beams consisted of two Concrete Strengths (Normal in NSC and High in HSC), three fibre dosages (25 kg/m^3, 50 kg/m^3, and 75 kg/m^3) and three types of fibers. A comprehensive statistical analysis was carried out to determine the applicability and robustness of the test method.

The results of TPBT on NSC reinforced with two different dosages of hooked-end steel fiber (25 kg/m^3 and 75 kg/m^3) are the object of the comparison with analytical response. In the following, the main variables of the experimental campaign, including the results, are summarized.

- **MATERIALS**

  ➢ **Matrix**

    The matrix was a Normal Strength Concrete (C25/30). The mix composition of cement: fine aggregate: coarse aggregate: water was equal to 1: 2: 2.5: 0.56 by weight. Concrete compressive strength (f_{cm}) equal to 35.3 Mpa.

  ➢ **Fiber**

    Hooked end steel fibers were considered (Dramix 65/60 BN). Their mechanical and geometrical properties, and their volume ratio for each mixture, are reported in Tables 6.47 and 6.48 respectively.

			Dramix 65/60 BN
Fiber diameter	d_f	[cm]	0.092
Fiber length	l_f	[cm]	6
Fiber aspect ratio	λ	[-]	65
Fiber tensile strength	f_u	[MPa]	1000

Table 6.47 Fiber mechanical and geometrical properties.

			C25/30(25)	C25/30(75)
Fiber volume ratio	V_f	[%]	0.32	0.95

Table 6.48 Fiber volume ratio for each mixture.

- **TEST SETUP**

The TPBT set-up used is illustrated in Figure 6.20 with some slight modifications from the RILEM recommendations. All tests were conducted under closed looped conditions. The measurements which were taken during testing were the load applied, mid-span displacements on both sides of the beam and the crack mouth opening displacement (CMOD). In the RILEM recommendations, it is stated that the tests should be conducted in a manner such that the average mid-span deflection increases at a constant rate of 0.2 mm/min. A slight modification was made with respect to this requirement. Instead of carrying out the tests under average mid-span deflection control, the tests were carried out under CMOD control. The actual notched specimen dimensions were 15X15X60 cm, the beam span was 50cm (Figure 6.20).
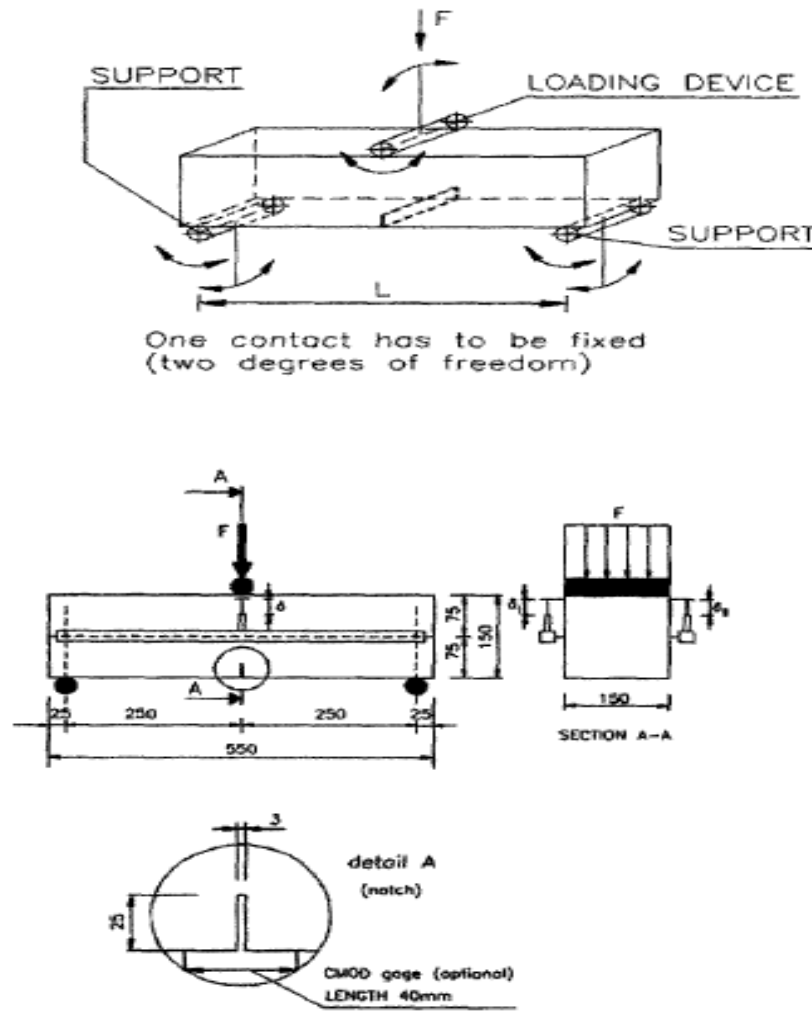
Figure 6.20 Bending Test setup on FRC specimen.

- **RESULTS**

For each specimen, identified by beam ID, the experimental data (black curves) with the related numerical simulations (blue curves) are represented in Figure 6.21. The best fit is obtained by varying the four parameters (K_{IC}, E, P_P, and w_c), which are summarized in Table 6.49 along with the dimensionless quantities, N_P and N_W.

ID	K_{IC}	E	P_P	w_C/l_f	N_P	N_W
	[kg/cm$^{1.5}$]	[MPa]	[kN]	[-]	[-]	[-]
C25/30(25)	88	60000	0.139	0.28	0.30	2957
C25/30(75)	104	70000	0.129	0.27	0.69	2815

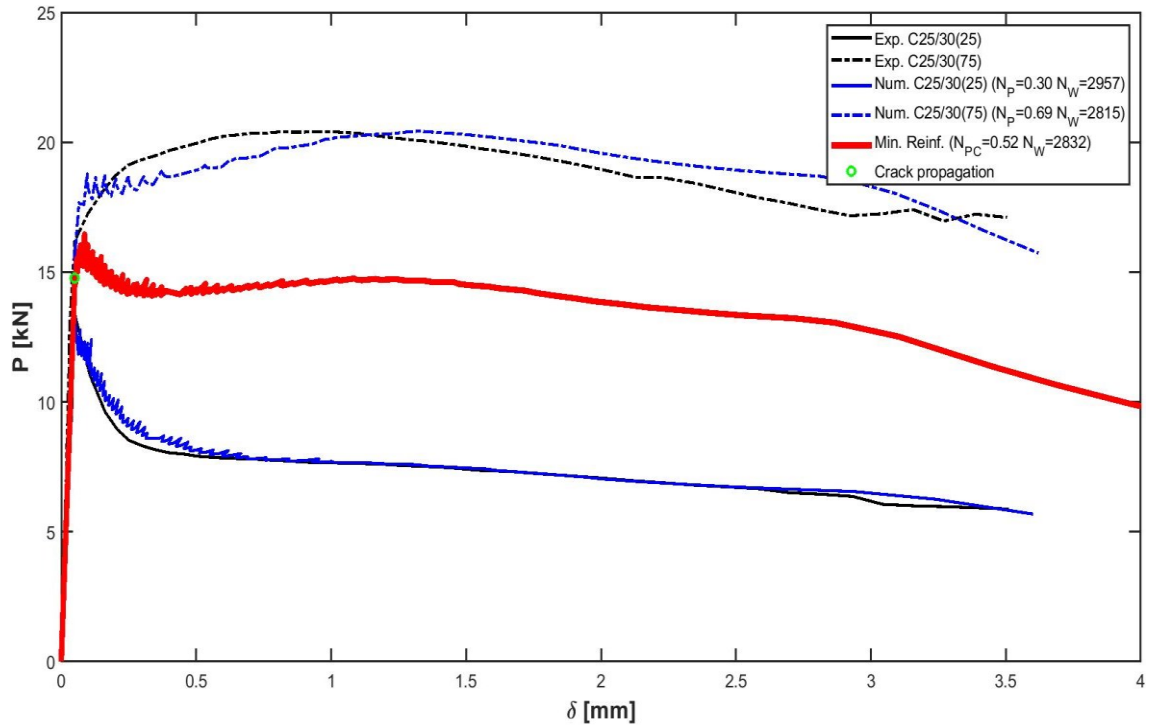**Table 6.49 Parameters obtained with best fitting procedure.**

Figure 6.21 Experimental and numerical $P - \delta$ **response.**

The tests conducted with the two fiber contents provide two typical response: with an insufficient amount of fiber the brittle failure of the specimen incurs, whereas the mixture more reinforced shows a strain-hardening post-cracking behaviour. The minimum reinforcement represent the fiber amount corresponding to the transition. Also in this case the high value of N_{W} (related to the fiber length) guarantee a stable ductile response (for $N_{\mathrm{P}} = N_{\mathrm{PC}}$, $N_{\mathrm{W}} = 2832$).

In Figure 6.21 is also represented, in red, the analytical curve of estimated minimum reinforcement condition. . To obtain it, K_{IC}, E, P_{P}, and w_C are assumed as the average of the parameters in Table 6.4, the slippage constitutive law for hooked-end fibers (section 3.3) is adopted, the number of fibers modelling is the deterministic one (Eq. 2.1), fiber distribution is uniform into the whole ligament, the other input data are defined as in Table 6.50.

Beam thickness	b	[cm]	15
Beam depth	h	[cm]	15
Notch depth	a_0	[cm]	2.5
Dimensionless notch depth	a_0/h	[-]	0.17
Beam span	S	[cm]	50
Beam length	L	[cm]	60
Young's modulus	E	[MPa]	65000
Fracture toughness	K_{IC}	[kg/cm$^{1.5}$]	96
Concrete compressive strength	f_{cm}	[MPa]	35.5
Fiber diameter	d_f	[cm]	0.092
Fiber length	l_f	[cm]	6
Fiber tensile strength	f_u	[MPa]	1000
Fiber pull-out strength	τ_u	[MPa]	2.86
Dimensionless fiber average embedded length	w_C/l_f	[-]	0.27
Fiber volume ratio	V_f	[-]	0.64

Table 6.50 Input data for minimum reinforcement condition.

Chapter 7

SIZE EFFECTS IN FRC BEAMS

7.1   Introduction

The flexural behaviour of different FRC specimens can vary with the specimen size. This phenomenon, known as *size effect*, was studied already for plain and ordinary reinforced concrete in the framework of Fracture Mechanics (Carpinteri, 1984; Bosco et al., 1990). In this work this analyse is extended to the FRC response.

Several other studies regarded the size effects in quasi-brittle materials, such as concrete. Particularly, the effects of the specimen size on tensile strength and fracture energy were widely investigated. These types of scale effects have been understood with a fractal geometry approach, which led to the definition of the Multifractal Scaling Law (MFSL) (Carpinteri et al., 1995). Regarding FRC composites, in the scientific literature there are experimental works, conducted on specimen with different specimen size, which confirm the scale effect on tensile or flexural strength and fracture energy (Fládr et al., 2018; Aghdasi, 2015; Prebhakumari et al, 2013; Ferrara et al., 2001).

This work, talking about size effect, it is referring to the global flexural behavior of the specimen, in terms of $P - \delta$ response. As seen in analytical simulations reported in Chapter 5, the Bridged Crack model is able to provide significant changes of the whole post-cracking behaviour, when the specimen depth increase. These changes can be predict through the dimensionless parameter N_P and N_W, since their opposite dependency on the beam depth. When the latter increases, N_P increases too, and the post-cracking behaviour in the stage II becomes more stable; on the other hand, an increase in the beam size, provides a decrease in N_W, causing less stability in the third branch of the response. In conclusion, an increase of the beam depth involves a double brittle-to-ductile-to-brittle transition, as shown in Chapter 5 (Figure 5.8).

In order to validate the model, three experimental campaigns, which involved specimen with different dimension, are analyzed and reproduced. All the experimental campaigns involve un-notched specimens; however, they are modelled with a small initial

crack, since the the bridged crack model requires an initiation to reproduce the crack propagation process.

Also in this Chapter, as in previous, the procedure provides a best-fit of each experimental curve. The actual matrix properties related to the elastic range are estimated, i.e., Young's modulus, E, and fracture toughness, K_{IC}; moreover, through the best-fit of the post-cracking ranges the pull-out force, P_{P}, and fiber embedded length, w_{C} are evaluated. The Bridged Crack model confirms again its capability to reproduce the three characteristic stage, also in case of size variation.

7.2   Comparison with experimental data

7.2.1 Yoo et al. experimental work

In the experimental study conducted by Yoo et al. (2016), the size effect on the flexural behavior of amorphous metallic fiber reinforced concrete (AM-FRC) was investigated. Following this purpose, several AM-FRC beams having three different sizes were fabricated with two different values of water-to-cementitious material ratio (w/c) and fiber volume fraction. In order to estimate the implication of fiber type on the size effect, steel fiber reinforced concrete (SFRC) having the same two different mixture proportion and 0.75% by volume of hooked-end steel fibers were also fabricated and tested.

The results of FPBT on the SFRC specimen, with three different specimen size, are the focus of this section.

- **MATERIALS**

  - ➢ **Matrix**

    The two different matrix were obtained by varying the w/c ratio. Their components and mechanical properties are reported in Table 7.1.

		W0.60	**W0.45**
Portland cement type I (c)	[kg/m³]	350	467
Water (w)	[kg/m³]	210	210
w/c	[-]	0.60	0.45
Superplasticizer	[%]	0-0.7%	0.3-1%
Fine aggregate	[kg/m³]	746	705
Coarse aggregate	[kg/m³]	1030	973
Concrete compressive strength (f_{cm})	[MPa]	29.2	44.7

Table 7.1 Concrete composition and mechanical properties.

  - ➢ **Fiber**

    Steel hooked-end fibers were used (S). Their mechanical and geometrical properties are reported in Table 7.2. The fiber volume ratio is equal to 0.75%.

			S
Fiber diameter	d_f	[cm]	0.05
Fiber length	l_f	[cm]	3
Fiber aspect ratio	λ	[-]	60
Fiber tensile strength	f_u	[MPa]	1195.5

Table 7.2 Fiber mechanical and geometrical properties.

- **SPECIMEN GEOMETRY AND TEST SETUP**

In order to estimate the size effect on the flexural behavior, three different un-notched specimen sizes were considered (Figure 7.1). However, as discussed, all the specimens are modelled with a small initial notch ($a_0 = 0.05h$).

-small: 5X5X25 cm;

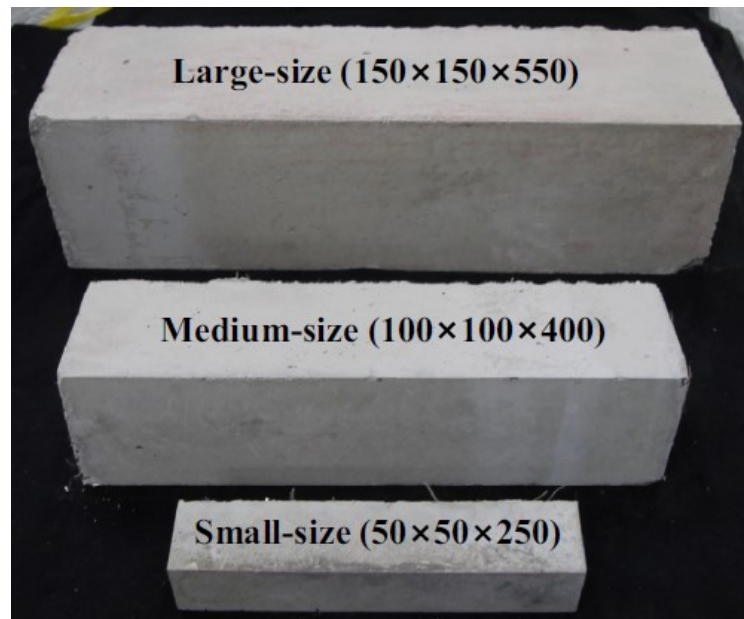-medium: 10X10X40 cm;

 -large: 15X15X55.

Figure 7.1 Different specimen size.

A monotonically increasing load was applied using the UTM with a maximum load capacity of 3000 kN at a rate of 0.2 mm/min, and the load was measured by the load cell affixed to the cross head. In order to obtain true mid-span deflection excluding the beam settlement at the supports, two LVDTs were mounted in the middle of the beam height
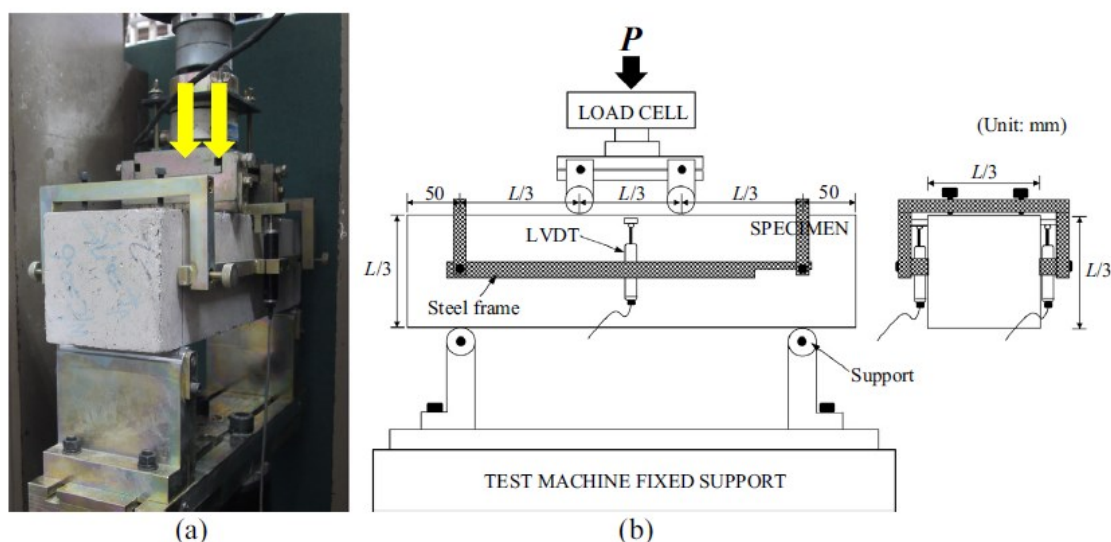
using a steel frame. Details of the test setup are shown in Figure 7.2. The beam span is assumed as triple of beam depth.

Figure 7.2 Bending Test setup on FRC specimen.

- **RESULTS AND DISCUSSION**

For each specimen, identified by beam ID, the experimental data (black curves) with the related numerical simulations (blue curves) are represented in Figure 7.3 and 7.4, for mixture W0.60%-S0.75% and W0.45%-S0.75%, respectively. The best fit is obtained by varying the four parameters (K_{IC}, E, P_P, and w_C), which are summarized in Table 7.3 and Table 7.4 (for each mixture) along with the dimensionless quantities, N_P and N_W.

W0.60%-S0.75%	K_{IC}	E	P_P	w_C/l_f	N_P	N_W
	[kg/cm$^{1.5}$]	[MPa]	[kN]	[-]	[-]	[-]
SMALL	57	22380	0.070	0.25	0.97	1317
MEDIUM	56	22380	0.050	0.30	1.08	1137
LARGE	29	12000	0.059	0.40	1.01	1282

Table 7.3 Parameters obtained with best fitting procedure.

In specimen with small and medium size, the matrix and fibers properties estimated are homogeneous. Indeed, it is recognizable an increase of N_P and a decrease in N_W values from small to medium specimen, which is consistent with the size effect predicted by the model.

However, the matrix properties of the specimen with large size results significantly lower, causing the inability of the dimensionless parameters to describe this scale transition.
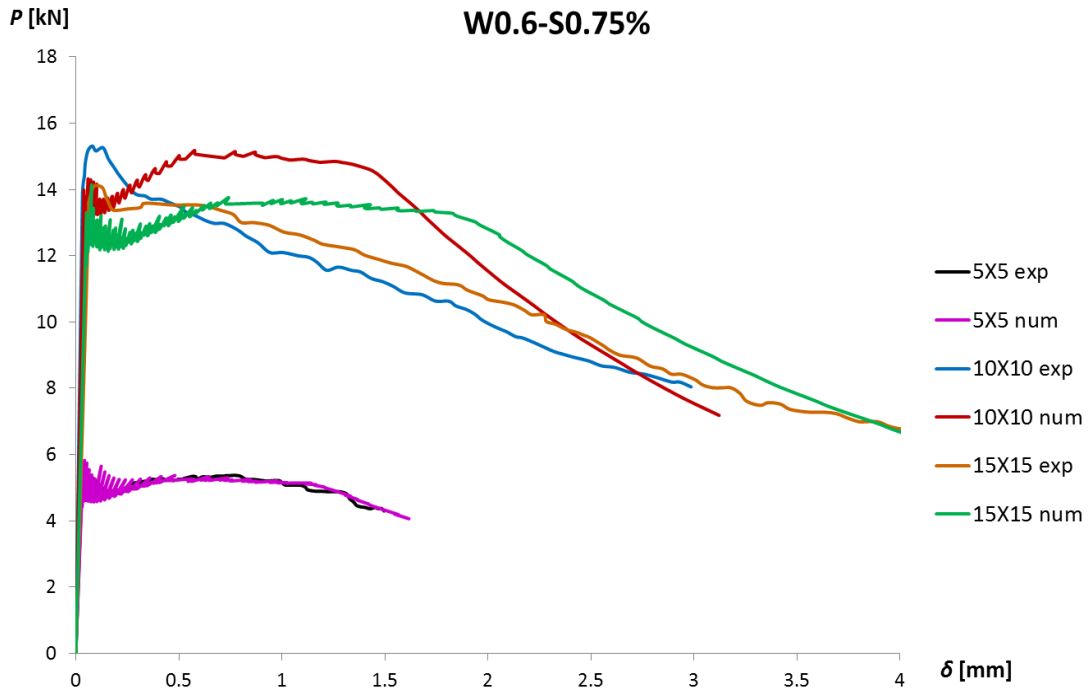

Figure 7.3 Experimental and numerical $P-\delta$ response.

The analytical curves describe globally the three stage of the experimental results, keeping the cracking load at the end of the elastic stage, the maximum load along the stage II, and the residual load at the end of the softening branch.

W0.45%-S0.75%	K_{IC}	E	P_P	w_C/l_f	N_P	N_W
	[kg/cm$^{1.5}$]	[MPa]	[kN]	[-]	[-]	[-]
SMALL	95	55000	0.090	0.15	0.87	1165
MEDIUM	75	36000	0.077	0.19	1.33	865
LARGE	33	20000	0.030	0.19	1.44	892

Table 7.4 Parameters obtained with best fitting procedure.

For the mixture with lower w/c ratio, thus with higher strength, the average fracture toughness and Young's Modulus estimated are higher, as it is expected. However, the matrix properties estimate in large size specimen are again significantly lower. Also in

this case, the scale transition between small and medium specimen is correctly described by the variation in N_{P} and N_{W} values.
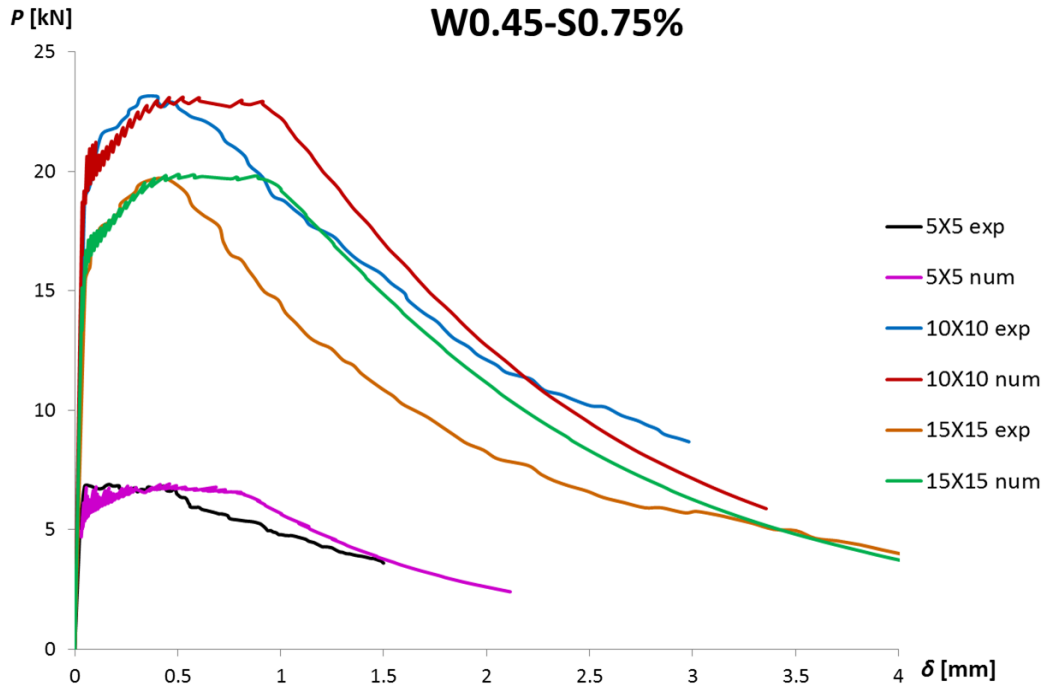

Figure 7.4 Experimental and numerical $P - \delta$ response.

The analytical curves follow the experimental ones in their three characteristic stages, keeping the cracking load at the end of the elastic stage, the maximum load along the stage II, and the residual load at the end of the softening branch.

7.2.2   Paschalis et al. experimental work

The experimental campaign conducted by Paschalis et al. (2015), at University of Brighton, in United Kingdom, was focused on the scale effects on Ultra High Performance Fiber Reinforced Concrete (UHPFRC), characterized by enhanced homogeneity and high density. Following this purpose, Four Point Bending Test were carried out on un-notched specimen with four different depths: 2.5 cm, 5 cm, 7.5 cm, and 10 cm.

- **MATERIALS**

  - **Matrix**

    The UHPFRC matrix components are reported in Table 7.5.

Portland cement 52.5 N (c)	[kg/m^3]	657
Water (w)	[kg/m^3]	185
w/c	[-]	0.28
Superplasticizer	[kg/m^3]	59
GGBS	[kg/m^3]	418
Silica fume	[kg/m^3]	119
Silica sand	[kg/m^3]	1051

Table 7.5 Concrete composition and mechanical properties.

  - **Fiber**

    Steel straight fibers were used (S). Their geometrical properties are reported in Table 7.6. The fiber volume ratio is equal to 3%.

			S
Fiber diameter	d_f	[cm]	0.016
Fiber length	l_f	[cm]	1.3
Fiber aspect ratio	λ	[-]	81

Table 7.6 Fiber geometrical properties.

- **SPECIMEN GEOMETRY AND TEST SETUP**

    In order to estimate the size effect on the flexural behavior, four different un-notched specimen sizes were considered (Figure 7.5). However, as discussed, all the specimens are modelled with a small initial notch ($a_0 = 0.05h$).
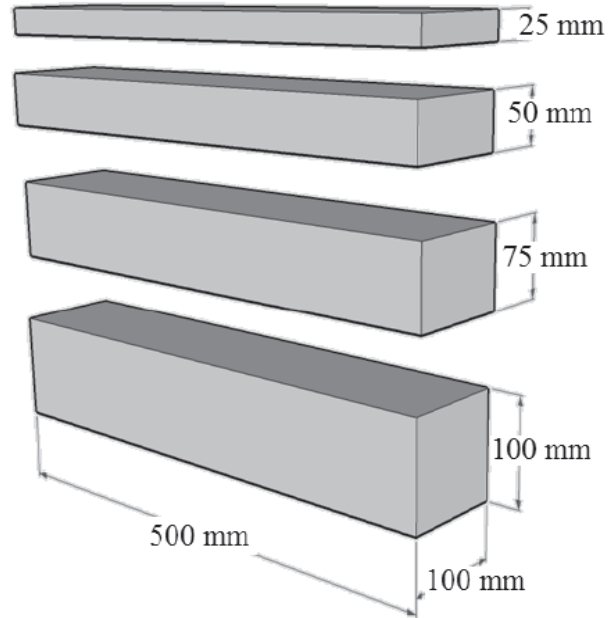

Figure 7.5 Bending Test setup on FRC specimen.

    The tests were conducted under four point loading, with a span length of 30 cm and distance between the two loading points of 10 cm. Two LVDTs were used to record the deflection of the beams in both sides and the tests were conducted using a displacement control of 0.001 mm/s. An external joke was used in order to exclude any additional displacement at the support. The testing setup is shown in Figure 7.6.

Figure 7.6 Bending Test setup on FRC specimen.

114

- **RESULTS AND DISCUSSION**

For each curve, identified by beam ID, the best fitting procedure provides the four parameters (K_{IC}, E, P_P, and w_C) required to define the analytical response curve, and the N_P and N_W values are evaluated (Table 7.7). The Figure 7.7 shows each experimental curve with corresponding analytical simulation.

	K_{IC}	E	P_P	w_C/l_f	N_P	N_W
	[kg/cm$^{1.5}$]	[MPa]	[kN]	[-]	[-]	[-]
10X2.5X50 cm	84	23000	0.010	0.30	4.05	675
10X5X50 cm	132	23000	0.010	0.30	3.65	304
10X7.5X50 cm	125	58000	0.007	0.30	3.39	661
10X10X50 cm	137	30000	0.008	0.35	3.68	315

Table 7.3 Parameters obtained with best fitting procedure.

The estimate of the matrix properties do not allows to appreciate all the scale transitions through the dimensionless parameter, in this case.
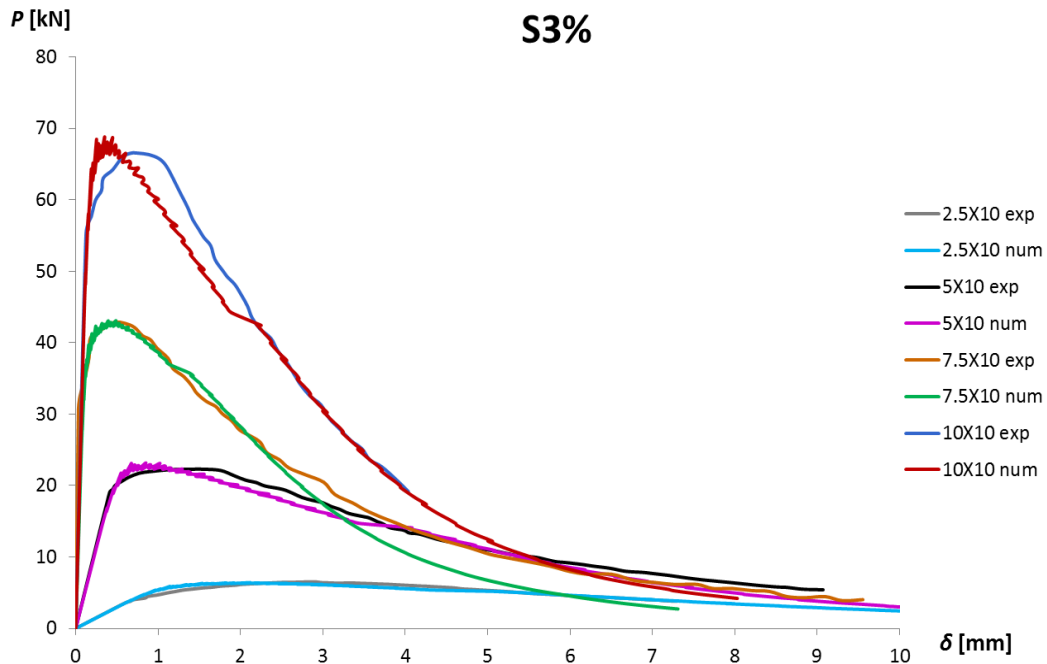

Figure 7.7 Experimental and numerical $P - \delta$ **response.**

In this experimental work the scale effect are recognizable graphically. By increasing the specimen depth, the load capacity increases, but the response becomes less stable, as predicted by the Bridged Crack model. The analytical curves follow the numerical ones in the three characteristic regimes of the response.

7.2.3   Jones et al. experimental work

The research project of Jones et al. (2008) was conducted to investigate the reinforcing mechanisms and fracture processes associated with SFRC under flexural load, in order to develop an alternative stress-profile model to predict flexural behaviour in the form of a load–deflection response using strain, crack-width and fibre pull-out data as the principal modelling parameters. An experimental investigation was undertaken, using a typical wet process steel fibre reinforced sprayed concrete mix design, to obtain the necessary data to implement and verify the model.

Un-notched specimens with three different depths were made with high strength concrete and two different amount of hooked-end steel fibers.

- **MATERIALS**

  - ➢ **Matrix**

The base concrete mix had a water:cementitious:aggregate ratio of 0.45:1.0:2.8, and contained silica fume replacement at 10% by weight of cement. The cement was Class 42.5N Portland Cement (PC), the condensed silica fume was a 50% water based slurry, the aggregate was a 6 mm maximum sized uncrushed river gravel. The concrete developed a 28-day compressive strength of 72 MPa.

  - ➢ **Fiber**

Hooked end steel fibers were added. Their mechanical and geometrical properties, and their volume ratio for each mixture, are reported in Tables 7.4 and 7.5 respectively.

Fiber diameter	d_f	[cm]	0.05
Fiber length	l_f	[cm]	3
Fiber aspect ratio	λ	[-]	60
Fiber tensile strength	f_u	[MPa]	1100

Table 7.4 Fiber mechanical and geometrical properties.

			C(40)	**C(80)**
Fiber volume ratio	V_f	[%]	0.5	1

Table 7.5 Fiber volume ratio for each mixture.

- **SPECIMEN GEOMETRY AND TEST SETUP**

Three different beam depths are considered. The specimens are un-notched. However, as discussed, all the specimens are modelled with a small initial notch ($a_0 = 0.05h$).

-SMALL: 10X5X50 cm

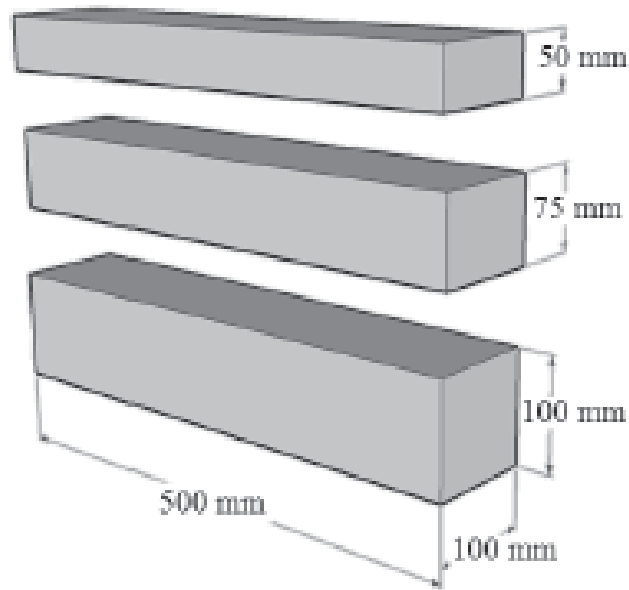-MEDIUM: 10X7.5X50 cm;

-LARGE: 10X10X50 cm.

Figure 7.8 Different specimen size.

A monotonically increasing load was applied using the UTM with a maximum load capacity of 3000 kN at a rate of 0.2 mm/min, and the load was measured by the load cell affixed to the cross head. In order to obtain true mid-span deflection excluding the beam settlement at the supports, two LVDTs were mounted in the middle of the beam height using a steel frame. Details of the test setup are shown in Figure 7.9. The beam span is assumed as triple of beam depth.
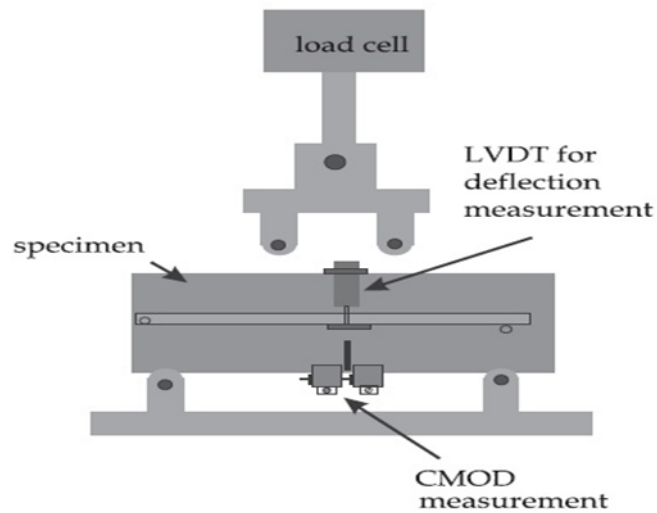
Figure 7.9 Bending Test setup on FRC specimen.

- **RESULTS AND DISCUSSION**

For each curve, identified by beam ID, the best fitting procedure provides the four parameters (K_{IC}, E, P_P, and w_c) required to define the analytical response curve, and the N_P and N_W values are evaluated (Table 7.6 and Table 7.7 for mixture C(40) and C(80), respectively). The Figures 7.10 and 7.11 show each experimental curve with corresponding analytical simulation, for the two different mixture.

C(40)	K_{IC}	E	P_P	w_C/l_f	N_P	N_W
	[kg/cm$^{1.5}$]	[MPa]	[kN]	[-]	[-]	[-]
SMALL	39	25000	0.053	0.38	0.77	3268
MEDIUM	61	28000	0.065	0.30	0.75	1508
LARGE	65	30000	0.070	0.30	0.86	1314

**Table 7.6 Parameters obtained with best fitting procedure.**

The matrix toughness and Young's Modulus are coherently estimated in medium and large specimens; indeed, it is recognizable an increase of N_P and a decrease in N_W values from medium to large specimen, that is coherent with the scale variation. However, in this case the smallest beam show a lower matrix performances.
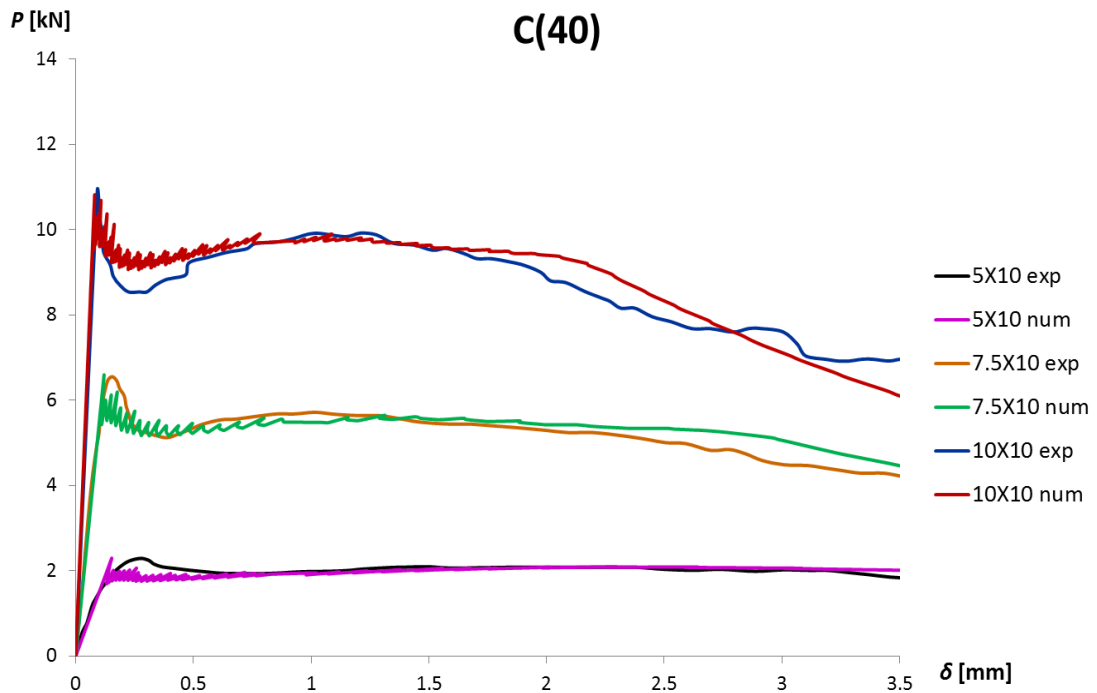
Figure 7.10 Experimental and numerical $P - \delta$ response.

C(80)	K_{IC}	E	P_P	w_C/l_f	N_P	N_W
	[kg/cm$^{1.5}$]	[MPa]	[kN]	[-]	[-]	[-]
SMALL	51	22000	0.058	0.20	1.29	1852
MEDIUM	64	34000	0.057	0.33	1.24	1920
LARGE	71	25000	0.066	0.20	1.51	668

Table 7.7 Parameters obtained with best fitting procedure.

The estimate of the matrix properties do not allows to appreciate all the scale transitions through the dimensionless parameter, in this mixture.
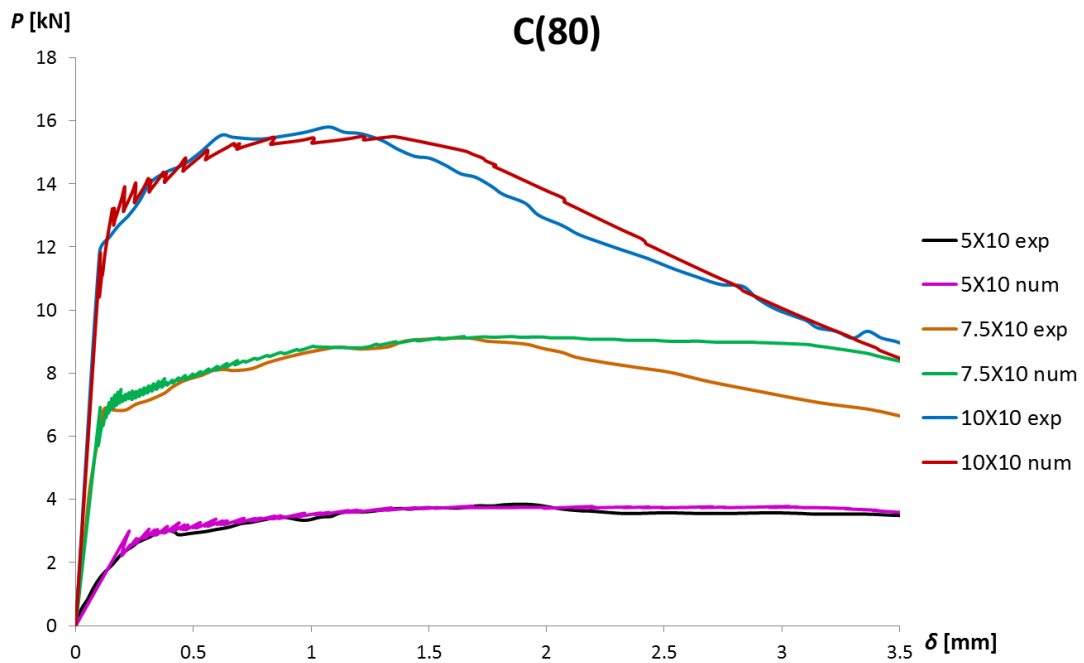
Figure 7.11 Experimental and numerical $P - \delta$ response.

Also in this last case, scale effects can be appreciate graphically. By increasing the beam depth, the flexural response becomes less stable, softening branch becomes indeed more influent in post-peak behaviour. The analytical curves follow the numerical ones in the three regimes of the response.

REFERENCES

Abdallah S., Fan M. and Rees D. W. A. (2018), "Bonding Mechanisms and Strength of Steel Fiber–Reinforced Cementitious Composites: Overview", *Journal of Materials in Civil Engineering*, Vol. 30.

Abdallah S. and Rees D. W. A. (2019), "Analysis of Pull-Out Behaviour of Straight and Hooked End Steel Fibres", *Engineering*, Vol. 11, pp. 332-341.

Accornero F. and Carpinteri A. (2020), "Fiber-Reinforced Brittle-Matrix Composites: Discontinuous Phenomena and Optimization of the Components", in: *Proceedings of XXIV AIMETA Conference 2019*. AIMETA 2019. Lecture Notes in Mechanical Engineering. Springer, Cham.

Accornero F., Rubino A. and Carpinteri A. (2020), "Ductile-to-brittle transition in fiber-reinforced concrete beams: Scale and fiber volume fraction effects", *Material Design & Processing Communication*, pp. 1-11.

Aghdasi P. (2015), "Mechanical Properties of a Highly flowable Ultra-High-Performance Fiber-Reinforced Concrete Mixture Considering Large-Size Effects". In: *Proceedings of the 7th RILEM Workshop on High Performance Fiber Reinforced Cement Composites* (HPFRCC-7), Stuttgard.

Alberti M. G., Enfedaque A., Gálvez J.C., Cánovas M.F., Osorio I.R. (2014), "Polyolefin fiber-reinforced concrete enhanced with steel-hooked fibers in low proportions", *Materials and Design*, Vol. 60, pp. 57-65.

Almusallam T., Ibrahim S.M., Al-Salloum Yousef, Abadel Aref, Abbas Husain (2016), "Analytical and experimental investigations on the fracture behavior of hybrid fiber reinforced concrete", *Cement and Concrete Composites*, Vol. 74, pp. 201-217.

ASTM C1018-97/1997, "Standard Test Method for Flexural Toughness and First-Crack Strength of Fiber-Reinforced Concrete (Using Beam With Third-Point Loading) (Withdrawn 2006)", West Conshohocken, PA, ASTM International.

ASTM C1609/C1609M-19a, "Standard Test Method for Flexural Performance of Fiber-Reinforced Concrete (Using Beam With Third-Point Loading)", West Conshohocken, PA, 2019, ASTM International.

Aydin S. (2013), "Effects of fiber strength on fracture characteristics of normal and high strength concrete", *periodica polytechnica*, Vol. 57, pp. 191-200.

Banthia N. and Gupta R. (2004), "Hybrid fiber reinforced concrete (HyFRC): fiber synergy in high strength matrices", *Materials and Structures*, Vol. 37, pp. 707-716.

Barr B.I.G., Lee M.K. (2003), "Round-robin analysis of the RILEM TC 162-TDF beam-bending test: Part 1- Test method evaluation", *Materials and Structures*, Vol. 36, pp 609-620.

Barenblatt I. G. (1962), "The Mathematical Theory of Equilibrium Cracks in Brittle", *Advanced in Apllied Mechanics*, Vol. 7, pp. 55-129.

Barros J.A.O., Cunha V.M.C.F., Ribeiro A.F., Antunes J.A.B. (2005), "Post-cracking behaviour of steel fibre reinforced concrete", *Materials and Structures*, Vol. 38, pp. 47-56.

Barros J.A.O., Sena Cruz J. (2001), "Fracture Energy of Steel Fiber-Reinforced Concrete", *Mechanics of Composite Materials and Structures*, Vol. 8, pp. 29-45.

Bencardino F., Rizzuti L., Spadea G., Swamy R.N. (2010), "Experimental evaluation of fiber reinforced concrete fracture properties", *Composites: Part B*, Vol. 41, pp. 17-24.

Bosco C., Carpinteri A. and Debernardi P. G. (1990), "Fracture of Reinforced Concrete: Scale Effects and Snap-back Instability", *Engineering Fracture Mechanics*, Vol. 35, No. 4/5, pp. 665-677.

Bosco C. and Carpinteri A. (1991), "Fibre toughening and crack growth stability in fibre reinforced disordered materials", *Fracture process in Concrete, Rock and Ceramics*.

Bosco C. and Carpinteri A. (1995), "Discontinuous constitutive response of brittle matrix fibrous composites", *Journal of the Mechanics and Physics of solids*, Vol. 43, No. 2, pp. 261-274.

Bruggi M., Venini P. (2012), "A numerical investigation on the size effect of fiber-reinforced concrete specimens in crack propagation", *Computational Mechanics*, Vol. 50, pp. 99-117.

Buttignol T. E. T., Sousa O. J. L. A., Bittencourt T. N. (2017), "Ultra High-Performance Fiber-Reinforced Concrete (UHPFRC): a review of material properties and design procedures", *Ibracon De Estruturas E Materiais*, Vol. 10, pp.957-971.

Carpinteri A. (1980) "Size effect in fracture toughness testing: A dimensional analysis approach", *Proceedings of the International Conference on Analytical and Experimental Fracture Mechanics*, Roma, Italy, Eds. G.C. Sih, M. Mirabile, Sijthoff & Noordhoff, Alphen an den Rijn, pp. 785-797.

Carpinteri A. (1982) "Notch sensitivity in fracture testing of aggregative materials", *Engineering Fracture Mechanics*, Vol. 16, pp. 467-481.

Carpinteri A. (1981), "A Fracture Mechanics Model for Reinforced Concrete Collapse", in *Proceedings of the IABSE colloquium on advanced mechanics of reinforced concrete*, Delft.

Carpinteri A. (1984), "Stability of fracturing process in R.C. beams", *Journal of Structural Engineering* (ASCE), Vol. 110, pp. 544-558.

Carpinteri A. (1994) "Scaling laws and renormalization groups for strength and toughness of disordered materials", *International Journal of Solids and Structures*, Vol. 31, pp. 291-302.

Carpinteri A. and Carpinteri An. (1984), "Hysteretic behaviour of R.C. beams", *Journal of Structural Engineering* (ASCE), Vol. 110, pp. 2073-2084.

Carpinteri A. and Chiaia B. (1995), "Multifractal scaling law for the fracture", in *Proceedings FRAMCOS-2*, Freiburg.

Carpinteri A. and Massabò R. (1996), "Bridged versus cohesive crack in the flexural behavior of brittle-matrix composites", *International Journal of Fracture*, Vol. 81, pp. 125-145.

Carpinteri A. and Massabò R. (1996), "Bridged versus cohesive crack in the flexural behavior of brittle-matrix composites", *International Journal of Fracture*, Vol. 81, pp. 125-145.

Carpinteri A. and Massabò R. (1997), "Continuous vs discontinuous bridged crack model of fiber-reinforced materials in flexure", *International Journal of Solids and Structures*, Vol. 34, pp. 2321-2338.

Carpinteri A. and Massabò R. (1997), "Reversal in failure scaling transition of fibrous composites", *Journal of Engineering Mechanics* (ASCE), Vol. 123, pp. 107-114.

Carpinteri A. and Accornero F. (2018), "Multiple snap-back instabilities in progressive microcracking coalescence", *Engineering Fracture Mechanics*, Vol. 187, pp. 272-281.

Carpinteri A. and Accornero F. (2019), "The Bridged Crack Model with multiple fibers: Local instabilities, scale effects, plastic shake-down, and hysteresis", *Theoretical and Applied Fracture Mechanics*, Vol. 104.

Carpinteri A. and Accornero F. (2019), "Ductile-to-Brittle Transition in Fiber-Reinforced Brittle-Matrix Composites: Scale and Fiber Volume Fraction Effects", in: *Proceeding of 10th International Conference on Fracture Mechanics of Concrete and Concrete Structures.* FraMCoS-X, Bayonne.

Carpinteri A. and Accornero F. (2020), "Residual crack opening in fiber-reinforced structural elements subjected to cyclic loading", *Strength, Fracture and Complexity*, Vol. 12, pp. 63-74.

Choi W., Jung K., Jang S. and Yun H. (2019), "The Influence of Steel Fiber Tensile Strengths and Aspect Ratios on the Fracture Properties of High-Strength Concrete", *Materials*, Vol. 12.

CNR DT 204/2006, Istruzioni per la Progettazione, l'Esecuzione ed il Controllo di Strutture di Calcestruzzo Fibrorinforzato.

Cox B. N. and Marshall D.B. (1991), "Stable and unstable solutions for bridged cracks in fracture and fatigue", *Acta Metallurgical Materials*, Vol. 38, pp. 579-589.

Cunha V., C. F. M., Barros J. A. O. and Sena-Cruz J. M. (2010), "Pullout Behavior of Stell Fibers in Self-Compacting Concrete", *Journal of Materials in Civil Engineering*, Vol. 22, pp. 1-9.

Dugdale D. S. (1960), "Yielding of Steel Sheets Containing Slits", *Journal of Mechanics and Physics of Solids*, Vol. 8, pp. 100-104.

Ferrara L., Gettu R. (2001), "Size effect in splitting tests on plain and steel fiber-reinforced concrete: A non-local damage analysis", *Fracture Mechanics of Concrete Structures*, pp. 677-684.

Fládr J., Bily P. (2018), "Specimen size effect on compressive and flexural strength of high-strength fibre-reinforced concrete containing coarse aggregate", *Composites Part B*, Vol. 138, pp. 77-86.

Foote R. M. L., Mai Y. M. and Cottarell B. (1986), "Crack growth resistance curves in strain-softening materials", *Journal of Mechanics, Physics and Solids*, Vol. 34, pp. 593-607.

Hillelborg A., Mooder M. and Petersson P. E. (1976), "Analysis of crack formation and crack growth in concrete by means of fracture mechanics and finite elements", *Cement and Concrete Research*, Vol. 6, pp. 773-782.

Holschemacher K., Mueller T., Ribakov Y. (2010), "Effect of steel res on mechanical properties of high-strength concrete", *Materials and Design*, Vol. 31, pp. 2604-2615.

Jenq Y. S. and Shah S. P. (1985) Two parameter fracture model for concrete", *Journal of Engineering Mechanics*, Vol. 111, pp. 1227-1241.

Jones P. A., Austin S. A., Robins P.J. (2008), "Predicting the flexural load–deflection response of steel fibre reinforced concrete from strain, crack-width, fibre pull-out and distribution data", *Materials and Structures*, Vol. 41, pp. 449-463.

Lim D.H., Oh B.H. (1999), "Experimental and theoretical investigation on the shear of steel fibre reinforced concrete beams", *Engineering Structures*, Vol. 21, pp. 937-944.

Marshall D. B., Cox B. N. and Evans A. G. (1985), "The mechanics of matrix cracking in brittle-matrix fiber composites", Acta Metallurgical Materials, Vol. 33, pp. 2013-2021.

Massabò R. (1993), "Meccanismi di rottura nei materiali fibrorinforzati", PhD. Thesis, Scuola di Dottorato, Politecnico di Torino.

Mobasher B., Bakhshi M., Barsby C. (2014), "Backcalculation of residual tensile strength of regular and high performance fiber reinforced concrete from flexural tests", *Construction and Building Materials*, Vol. 70, pp. 243-253.

Naaman A. E., Namur G. G., Alwan J. M. and Najm H. S. (1991a), "Fiber pullout and bond slip. I: Analytical study", *Journal of Structural Engineering*, Vol. 117, pp. 2769-2790.

Naaman A. E., Namur G. G., Alwan J. M., and Najm, H. S. (1991b)."Fiber pullout and bond slip. II: Experimental validation.", *Journal of Structural Engineering*, Vol. 117, pp. 2791-2800.

Naaman A.E., Reinhardt H.W. (2006). "Proposed classification of HPFRC composites based on their tensile response". *Materials and Structures*, Vol. 39, pp. 547–555

Naaman A.E. (2008), "High Performance Fiber Reinforced Cement Composites". In: Shi C., Mo J.L. (Eds), *High-performance Construction Materials*, pp. 91-153.

NBN B 15-238 (1992), Proeven op vezelversterkt beton – Buigproef op prismatische proefstukken. Brussel: Belgian Institute for Normalisation.

Paschalis S. A., Lampropoulos A. P. (2015), "Size effect on the flexural performance of Ultra High Performance Fiber Reinforced Concrete (UHPFRC)", in Proceedings of the 7th RILEM Workshop on High Performance Fiber Reinforced Cement Composites (HPFRCC-7), Stuttgard, pp. 177-184.

Prebhakumari K. S., Jayakumar P. (2013), "Fracture Parameters of Steel Fibre Reinforced High Strength Concrete by Size Effect Method", *International Journal of Scientific & Engineering Research*, Vol. 4.

Puzzi S. (2004), "Mechanics of grained or fibrous heterogeneous materials", PhD. Thesis, Scuola di Dottorato, Politecnico di Torino.

RILEM 50-FMC, "Determination of fracture energy of mortar and concrete by means of three-point bend tests on notched beams" (1985), *Materials and Structures*, Vol. 18, pp. 285–290.

RILEM TC 162-TDF: Test and design methods for Steel Fibre Reinforced Concrete (2001), "Uni-axial tension test for steel fibre reinforced concrete", *Materials and Structures*, Vol. 34, pp. 3-6.

RILEM TC 162-TDF: Test and design methods for Steel Fibre Reinforced Concrete (2002), "Design of steel fibre reinforced concrete using the σ-w method: principles and applications", *Materials and Structures*, Vol. 35, pp. 262-278.

RILEM TC 162-TDF: Test and design methods for Steel Fibre Reinforced Concrete (2002), "Bending test: Final Recommendation", *Materials and Structures*, Vol. 35, pp. 579-582.

RILEM TC 162-TDF: Test and design methods for steel fibre reinforced concrete (2003), "σ-ε design method: Final Recommendation", *Materials and Structures*, Vol. 36, pp. 560-567.

RILEM, TC-187-SOC: Indirect test for stress-crack opening curve (2007). In: Experimental Determination of the Stress-Crack Opening Curve for Concrete in Tension - Final report of RILEM Technical Committee TC 187-SOC, RILEM Publications SARL.

Robins P., Austin S. and Jones P. (2002), "Pull-out behaviour of hooked steel fibres", *Materials and Structures*, Vol. 35, pp. 434-442.

Soetens T., Matthys S. (2014), "Different methods to model the post-cracking behaviour of hooked-end steel fibre reinforced concrete", Construction and Building Materials, Vol. 73, pp. 458-471.

Soulioti D. V., Barkoula N. M., Paipetis A. and Matikas T.E. (2009), "Effects of Fibre Geometry and Volume Fraction on the Flexural Behaviour of Steel-Fibre Reinforced Concrete", *Strain*, Vol. 47, pp e535-e541.

Tada H., Paris P. and Irwin G. (1985), "The Stress Analysis of Cracks", St. Louis, Missouri, Paris Productions Incorporated (and Del Research Corporation).

Yoo D., Banthia N., Yang J., Yoon Y. (2016), "Size effect in normal- and high-strength amorphous metallic and steel fiber reinforced concrete beams", *Construction and Building Materials*, Vol. 121, pp. 676-685.